Politecnico di Milano

SCHOOL OF INDUSTRIAL AND INFORMATION ENGINEERING
Master of Science Degree in Aeronautical Engineering

POLITECNICO
MILANO 1863

Comprehensive Flight Testing and Data Analysis for a New Ultralight Aircraft

Candidate:
Saverio Oldani
841266

Supervisor:
Prof. Lorenzo Trainelli

Assistant Supervisors:
Prof. Alberto Rolando
Ing. Simone Quaglietta

Academic year
2016-2017

«Terras licet» inquit «et undas
obstruat, at caelum certe patet; ibimus illac!
omnia possideat, non possidet aëra Minos».
Dixit et ignotas animum dimittit in artes
naturamque novat.

Ovidio, *Metamorfosi*, VIII, 185–189

Ringraziamenti

Il primo ringraziamento è al Professor Lorenzo Trainelli, per la continua disponibilità e pazienza, per i saggi consigli e indicazioni su come svolgere al meglio questo gratificante lavoro. Grazie al Professor Alberto Rolando, per l'indiscutibile professionalità e competenza sul campo di volo nella gestione della sua *creatura*, che è stata una dei protagonisti dei giorni passati a Mezzana.

Impossibile non esprimere gratitudine a Simone Quaglietta, eccellente e infaticabile pilota, nonchè fonte di preziosi suggerimenti nel corso delle ore passate sul mezzo e dei giorni impiegati ad analizzare infiniti dati.

Grazie a Nando Groppo, per l'amore per il suo lavoro e la passione che è riuscito a trasmettermi nelle giornate sul campo. L'esperienza di questa tesi non avrebbe visto la luce senza di lui.

Il ringraziamento più sincero va alla mia famiglia, a mia mamma e mio papà, a Pietro e Francesca, per il loro sostegno silenzioso e presente durante questi anni di studi.

Infine, una dedica particolare e di cuore agli amici di vacanze, serate e capodanni, per le chiacchiere, le risate fino alle lacrime e per tutti questi anni insieme. E agli amici di *Soave*, compagni unici in questo percorso, per i viaggi, le discussioni da talk-show e per aver fatto in modo che un lustro passasse in un soffio.

Abstract

Flight testing activities play a key role in the development phase of a new air vehicle. Through flight testing, the predictions made in the design phase can be verified on the actual aircraft in its real operational conditions. Also, flight testing contributes, as mandatory means of compliance, to the demonstration of the aircraft fitness according to airworthiness regulations.

The present work concerns a comprehensive flight test campaign performed on a new aircraft model, the TRAIL G70 ultralight, two-seater airplane. This activity was carried out on the second G70 prototype, which was developed to correct and improve some characteristics revealed during a previous campaign on the first prototype. The present campaign, encompassing both performance and control & stability characteristics, was designed in order to investigate the G70 compliance with the German LTF-UL norms. In addition to compliance verification, a number of further analyses was carried out, in order to identify some fundamental characteristics of the aircraft and derive an analytical model for performance prediction.

Critical analysis of the results showed that a few improvements are still needed to completely fulfil the LTF-UL requirements. Therefore, this work establishes an important knowledge base to be used in the final design optimization.

Sommario

L'attività di flight testing gioca un ruolo essenziale nella fase di sviluppo di un nuovo velivolo. Attraverso di essa, le previsioni effettuate nelle fasi precedenti possono essere verificate sull'aeromobile nelle sue reali condizioni operative. Inoltre, l'attività di flight testing contribuisce alla dimostrazione della rispondenza del velivolo alle normative di idoneità al volo.

Il presente lavoro descrive la campagna globale di flight testing effettuata su un nuovo modello di velivolo, il TRAIL G70, ultraleggero biposto. L'attività si è svolta sul secondo prototipo del G70, sviluppato per correggere e migliorare alcuni aspetti emersi da una precedente campagna sul primo velivolo. La campagna oggetto del presente lavoro ha avuto come obiettivo la dimostrazione della rispondenza del velivolo alle norme della tedesca LTF-UL, includendo analisi di prestazione, controllo e stabilità. Inoltre, sono state condotte ulteriori analisi per identificare delle caratteristiche fondamentali del velivolo e per ricavare un modello analitico di predizione delle prestazioni.

L'analisi critica dei risultati ha mostrato che è necessario ancora un numero ridotto di migliorie per soddisfare appieno i requisiti della LTF-UL. Di conseguenza, questo lavoro costituisce una importante base da utilizzare nell'ottimizzazione finale del velivolo.

Contents

List of Figures

List of Tables

List of Symbols

$(\cdot)_{,x}$	Generic derivative of a quantity with respect to the variable x	
$(\cdot)_{,eq}$	Generic quantity referred to the equilibrium condition	
$(\cdot)_{,lin}$	Generic quantity referred to the linear drag polar CD versus C_L^2	
$(\cdot)_{,par}$	Generic quantity referred to the parabolic drag polar	
$(\cdot)_S$	Generic standard quantity	
$(\cdot)_T$	Generic quantity in the test condition	
$(\cdot)_t$	Generic quantity referred to the tail	
$(\cdot)_{wb}$	Generic quantity referred to the wing-body combination	
a	Derivative of C_L with respect to α	[-]
a_X	Acceleration in the X direction	[m/s^2]
a_Y	Acceleration in the Y direction	[m/s^2]
a_Z	Acceleration in the Z direction	[m/s^2]
b	Propeller polar third order coefficient	[-]
c	Wing chord	[m]
c_e	Engine's characteristic parameter	[-]
e	Oswald's factor	[-]
f	Frequency	[Hz]
f_C	Cut-off frequency	[Hz]
f_S	Sampling frequency	[Hz]
h	Altitude	[m]
l	Aircraft length	[m]
m	Propeller polar first order coefficient	[-]
n	Load factor	[-]
p	Pitch rate	[rad/s]
q	Roll rate	[rad/s]

r	Yaw rate	[rad/s]
x_A	Dimensional position of the aerodynamic center	[m]
C	Shaft torque	[Nm]
C_0	Shaft torque at SSL	[Nm]
C_D	Drag coefficient	[-]
$C_{D,min}$	Minimum drag coefficient	[-]
C_{D0}	Parasite drag coefficient	[-]
C_f	Skin friction coefficient	[-]
C_L	Complete aircraft lift coefficient	[-]
C_l	Airfoil lift coefficient	[-]
$C_{L_{C_{D,min}}}$	Lift coefficient at the point of minimum C_D	[-]
C_M	Complete aircraft moment coefficient	[Nm]
$C_{M,N}$	Complete aircraft moment coefficient around the neutral point	[Nm]
C_P	Power coefficient	[-]
C_T	Thrust coefficient	[-]
D	Drag	[N]
D_I	induced drag	[N]
D_P	Parasite drag	[N]
D_p	Propeller diameter	[m]
F	Stick force	[N]
H	Coefficient of the first order term in the parabolic drag polar	[-]
J	Advance ratio	[-]
K	Induced drag factor	[-]
L	Lift	[N]
N	Engine revolutions in the time unit	[1/s]
P	Power	[W]
P_a	Available power	[W]
P_b	Brake horsepower	[W]
P_r	Requested power	[W]
P_{xs}	Excess power	[W]
R_Y	Radius of gyration in the Y axis	[m]
S	Wing surface	[m^2]
$S_{50_{LD}}$	Standard distance from 15 m obstacle to full stop during LND	[m]
$S_{50_{TO}}$	Standard distance from brake release to 15 m obstacle during TO	[m]
$S_{a0_{LD}}$	Raw distance in the air during LND	[m]
$S_{a0_{TO}}$	Raw distance in the air during TO	[m]

$S_{aS_{LD}}$	Weight and density reduced distance in the air during LND	[m]
$S_{aS_{TO}}$	Weight and density reduced distance in the air during TO	[m]
$S_{aT_{LD}}$	Wind-reduced distance in the air during LND	[m]
$S_{aT_{TO}}$	Wind-reduced distance in the air during TO	[m]
$S_{g0_{LD}}$	Raw distance on the ground during LND	[m]
$S_{g0_{TO}}$	Raw distance on the ground during TO	[m]
$S_{gS_{LD}}$	Weight and density reduced distance on the ground during LND	[m]
$S_{gS_{TO}}$	Weight and density reduced distance on the ground during TO	[m]
$S_{gT_{LD}}$	Wind-reduced distance on the ground during LND	[m]
$S_{gT_{TO}}$	Wind-reduced distance on the ground during TO	[m]
S_{wet}	Wet surface	[m^2]
T	Thrust	[N]
$\overline{T}$	Period of dynamic modes	[s]
T_{xs}	Excess thrust	[N]
V_{BG}	Speed for best efficiency (maximum range) during glide	[m/s]
V_d	Vertical speed of descent	[m/s]
$V_{d,BG}$	Vertical speed of descent in maximum efficiency condition	[m/s]
V_{FC}	Speed of fastest climb	[m/s]
V_{FE}	Maximum speed with flaps deflected	[m/s]
$V_{GS_{LO}}$	Ground speed at the lift-off time	[m/s]
$V_{GS_{TD}}$	Ground speed at the touch-down time	[m/s]
V_{LO}	Lift-off speed	[m/s]
V_{LO_W}	Weight reduced lift-off speed	[m/s]
V_M	Maximum speed	[m/s]
V_m	Minimum speed	[m/s]
V_{MD}	Speed for best endurance in glide	[m/s]
V_{NE}	Never exceed speed	[m/s]
V_{NO}	Maximum speed with turbulence	[m/s]
V_R	Rotation speed	[m/s]
V_{S0}	Stall speed in LND configuration	[m/s]
V_{S1}	Stall speed in one specific configuration	[m/s]
V_{SC}	Speed of steepest climb	[m/s]
V_{TD}	Touch-down speed	[m/s]
V_{TD_W}	Weight reduced touch-down speed	[m/s]

V_v	Vertical speed of climb	[m/s]
$V_{W_{LD}}$	Wind speed at landing	[m/s]
$V_{W_{TO}}$	Wind speed at take-off	[m/s]
W	Weight	[N]
X_G	Center of gravity position	[% MAC]
X_N	Neutral point position	[% MAC]
α	Angle of attack	[deg]
β	Angle of sideslip	[deg]
γ	Climb angle	[deg]
γ_d	Descent angle	[deg]
$\gamma_{d,BG}$	Descent angle in the condition of maximum efficiency	[deg]
γ_{SC}	Best angle of climb	[deg]
Δt_{DBLT}	Doublet semi-period	[s]
Δt_{IMP}	Impulse semi-period	[s]
Δt_{RUDD}	Rudder pulse semi-period	[s]
δ_a	Aileron deflection angle	[deg]
δ_e	Elevator deflection angle	[deg]
δ_r	Rudder deflection angle	[deg]
ϵ	Downwash angle	[deg]
ζ	Damping	[-]
η	Tail efficiency	[-]
η_p	Propeller efficiency	[-]
θ	Pitch angle	[deg]
Θ	Temperature	[K]
λ	Aspect ratio	[-]
ξ_A	Dimensionless position of the aerodynamic center on the longitudinal axis	[-]
ξ_N	Dimensionless position of the neutral point on the longitudinal axis	[-]
ρ_0	SSL air density	[kg/m^3]
σ	Ratio between density and ground standard density	[-]
Φ	Power drop-off factor	[-]
ϕ	Roll angle	[deg]
ψ	Yaw angle	[deg]
ω_{PH}	Phugoid frequency	[rad/s]
ω_{SP}	Short period frequency	[rad/s]
$\hat{\omega}_{SP}$	Numerically estimated short period frequency	[rad/s]

List of Acronyms

A/C	Aircraft
CAS	Calibrated Airspeed
CG	Center of Gravity
CHT	Cylinder Head Temperature
CR	Cruise
DAer	Department of Aerospace Science and Technology
EAS	Equivalent Airspeed
EFIS	Electronic Flight Instrument System
FFT	Fast Fourier Transform
FTE	Flight Test Engineer
FTG	Flight Test Guide
FTI	Flight Test Instrumentation
GLONASS	GLObal NAvigation Satellite System
GPS	Global Positioning System
GS	Ground Speed
IAS	Indicated Airspeed
LND	Landing
MAC	Mean Aerodynamic Chord
MCP	Maximum Continuous Power
MEMS	Micro Electro Mechanical System
OAT	Outside Air Temperature
PSD	Power Spectral Density
QZSS	Quasi-Zenit Satellite System
ROC	Rate of Climb
RPM	Revolutions per Minute
RSS	Root of Sum of Squares
SHSS	Steady Heading Side-Slip
SSL	Standard Sea Level
TAS	True Airspeed
TO	Take-off

TP	Test Pilot
UL	Ultralight

Chapter 1

Introduction

1.1 Work rationale

Almost ten years passed since 2008, when *Politecnico di Milano* started a collaboration with *Ing. Nando Groppo SRL*, a highly valued UL (ultralight) aircraft manufacturer located in the small town of Mezzana Bigli, close to the city of Pavia, Italy. Nando Groppo has been designing and manufacturing UL aircraft since 1973 and in 1993 he founded the company of the same name. The last airplane produced is the G70, whose first version has been manufactured in 2015. After the campaign aimed at investigating the certification potential of this aircraft, held between October 2015 and March 2016 ([11]), Mr. Groppo started focusing on the second, improved, prototype of the G70: the result came into the world at the beginning of 2017 with the name of TRAIL G70. It shares most of its characteristics with the older version, but, at the same time, it features some significant modifications, detailed in 2.1.2.

The manufacturer wanted to perform a flight test campaign in order to check the behaviour of the aircraft with regard to performance, manoeuvrability and stability and to be sure that all the modifications of the new aircraft did not affect its compliance to regulations. The campaign followed the prescriptions of the German LTF-UL ([5]) in order to verify the G70 airworthiness and to inspire corrections, should any deficiencies arise. Moreover, some data have been used to develop further analyses in flight performance, as the drag polar estimate or the analysis of climbing and gliding capabilities, and in static stability, basically through an accurate evaluation of the neutral point position.

1.2 Campaign execution

The campaign took place between May and July 2017 and was performed in cooperation with the course of *Flight Testing*, held by Prof. L. Trainelli at *Politecnico di Milano*. The first tests, namely the calibration of the anemometer and some general tests to verify the manoeuvrability and the stall behaviour of the aircraft have been planned, performed and post-processed by the author as FTE (Flight Test Engineer). The other tests, which referred to LTF-UL, were planned and post-processed by the author and executed with the students of the course as FTEs after the general behaviour of the aircraft had already been confirmed. The TP (Test Pilot), for all the campaign duration, was Simone Quaglietta.

Test points have been executed applying the standard techniques described in the CS23 FTG ([1]), according to LTF-UL prescriptions. Data have been recorded by hand, mainly the atmospheric ones, and by means of the Mnemosine FTI (Flight Test Instrumentation), a complete instrumentation suite able to sense and record a great number of parameters which have been critically analysed during the work. The software employed for the post-processing phase, including the plot of all the graphs, has been developed in MATLAB.

1.3 Structure of the thesis

The thesis starts with an introduction of the test aircraft and of the area in which the tests were executed. The following chapter details the instrumentation employed during the campaign, in terms of sensor features, sample frequency and main limitations; the chapter includes a description of the filtering process on the data, with an example of its functioning.

The main corpus of the work includes the detailed description and results presentation of all the tests performed for certification purposes. The first tests are the performance ones, with stall, take-off, landing and climb performance. Controllability and manoeuvrability tests follows: they focus on lateral and directional control, control forces during manoeuvres and trim tests. Stability tests conclude the main part of the work, with static and dynamic stability, both longitudinal and lateral-directional; the latter focuses on the aircraft modes which may affect the safety and the comfort of the flight.

Some additional investigations have been performed with the available data, namely neutral point estimation and drag polar approximation. The former has been experimentally performed with a series of trim flight con-

ditions, and then compared to the results of a vortex-lattice model and an analytical two-surface model. The latter employed the glide tests, together with the trim ones, already used for neutral point estimation.

The thesis ends with an estimation of the performance of the aircraft extended to the full flight envelope, in terms of weight and altitude, using the so-called Bootstrap approach to flight performance ([16], [17]). This method receives as input some parameters calculated through flight tests in a single condition of weight and altitude; its main drawback is the high sensitivity to input parameters variation, which is detailed in the last chapter.

Chapter 2

Test aircraft and location

This chapter describes the features of Nando Groppo TRAIL G70, the test aircraft which flew during this campaign, and all the differences with respect to the older version. Secondly, the test area where the aircraft has been flown will be detailed, with all the limitations that a light aircraft has to observe.

2.1 Test aircraft

TRAIL G70 is the second prototype of the last aircraft manufactured by *Ing. Nando Groppo SRL*. TRAIL G70 is an ultralight aircraft, high-wing, single engine, meant for recreational, not aerobatic, flight. The cabin is a steel-made framework with aluminium alloy coverage, supplied with two side-by side seats. The aircraft has a tricycle landing gear, with the front wheel steerable by the rudder pedals ([6]).

The engine is a Rotax 912ULS, four stroke, four cylinders, able to provide a maximum take-off power of 74kW (100 Hp) at 5800 rpm ([7]). The propeller is a Duc Helices Flash Droite, three blades, fixed pitch, with a diameter of 1.76 m. The aircraft mounts two tanks inside the wings, with a capacity of 50 l each.

Tab. 2.1 and summarizes the main geometric characteristics and limitations of the airplane, respectively.

2.1.1 Cockpit

The aircraft mounts double commands, which allows to pilot either from the right and the left seat. The seats are side-by-side and they can be adjusted according to the pilot's size in the longitudinal direction. They are equipped of four-points seat belts. Behind the seats there is the luggage compartment,

Table 2.1: TRAIL G70 main geometric characteristics

Wingspan	[m]	8.90	Wing surface	[m^2]	10.56
Length	[m]	6.22	Wing load	[kg/m^2]	44.7
Width	[m]	2.74	Cabin width	[m]	1.22
Heigth	[m]	2.32	Landing gear width	[m]	1.80

Table 2.2: TRAIL G70 main limitations

Weight limitations [kg]	
MTOW	472.5
Maximum project weight	600
Maximum weight of fuel	72
Maximum weight of luggage	40
Speed limitations [km/h]	
V_{FE}	110
V_{NE}	210
V_{NO}	160
Other limitations	
Ceiling [ft]	15000
Max/Min load factor [g]	+4/-2

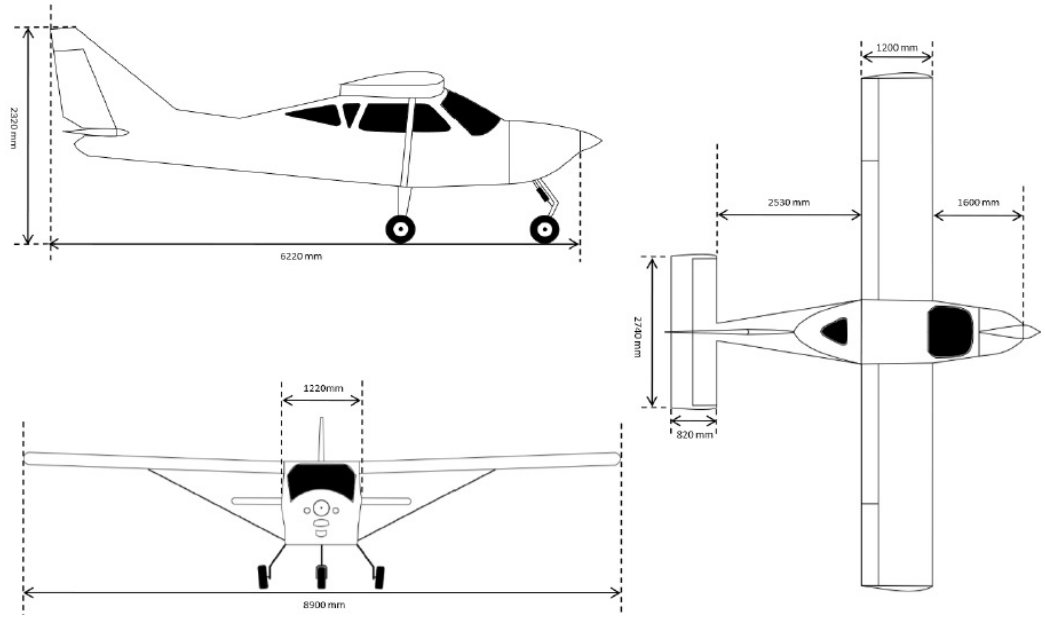

Figure 2.1: TRAIL G70 three view representation.

Figure 2.2: TRAIL G70 on the apron.

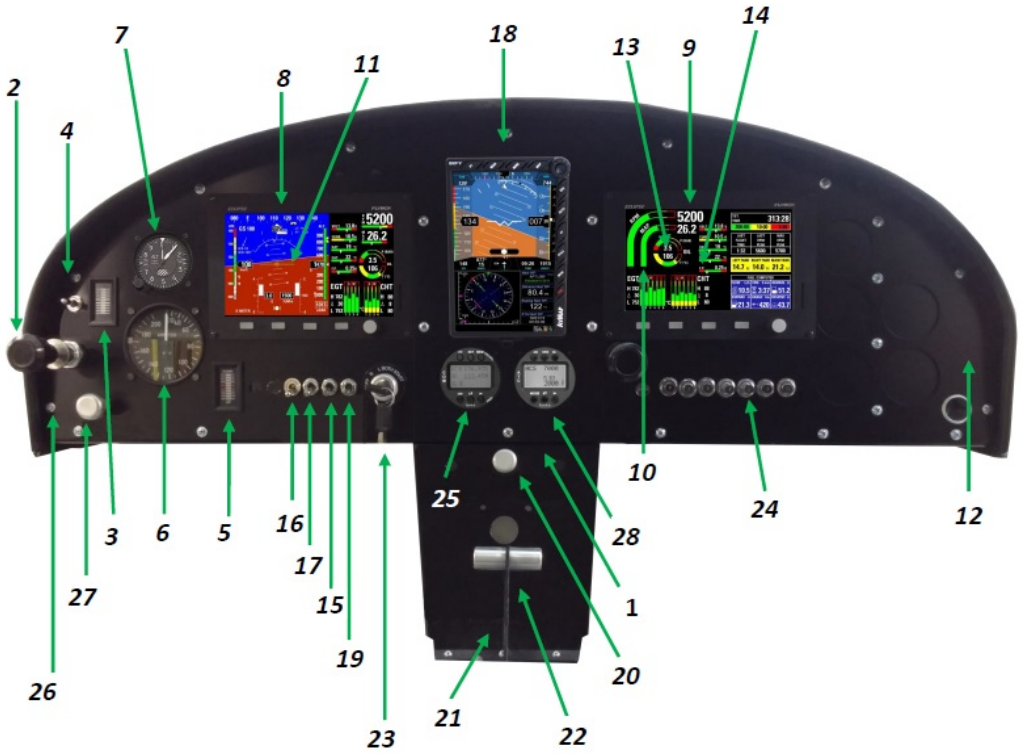

Figure 2.3: TRAIL G70 dashboard.

which can be loaded with a maximum of 40 kg weight.

The cockpit is organized as shown in Fig. 2.3, with a brief description of the instrumentation in Tab. 2.3.

2.1.2 Comparison with the older version

The TRAIL G70 of the 2017 flight test campaign is the evolution of the first G70, which was designed between 2014 and 2015. The new G70 features some important modifications:

- Horizontal tail plane:
  - The tail plane has been raised of 80 mm, moved back of 90 mm and now is passing through the fuselage, as shown in Fig. 2.4;
  - The trim tab has been lengthened, it is symmetric with respect to the longitudinal axis of the airplane and it has been inserted into the elevator, as shown in Fig. 2.4;

Table 2.3: Cockpit instrumentation

1	Airbox command	15	Light switch
2	Throttle	16	Radio switch
3	Flap position indicator	17	Auxiliary pump switch
4	Flap lever	18	EFIS
5	Trim position indicator	19	Master switch
6	Anemometer	20	Cabin heating switch
7	Altimeter (not provided)	21	Brake valve
8	Turn coordinator	22	Brake lever
9	Engine RPM indicator	23	Engine switch
10	Fuel pressure indicator	24	Fuses
11	EFIS	25	Radio
12	Headphones plug (co-pilot)	26	Headphones plug (pilot)
13	Oil pressure and temperature indicator	27	Choke
14	CHT indicator	28	Transponder (not provided)

  - The horizontal tail plane has been counterweighted with additional masses. Now the elevator is horizontal when the aircraft is on the ground.

- Fuselage:
  - The width of the cabin has been increased: from 1035 mm to 1220 mm of the new version;
  - Aerodynamic enhancement of the junction between cabin and tail trunk;
  - The nose has been lengthened and its angle with respect to the windscreen has been increased in order to raise the aerodynamic efficiency of the aircraft, as shown in Fig. 2.5;
  - The leaf spring of the landing gear has been inserted inside the fuselage, with the aim of enhancing the aerodynamic efficiency, as shown in Fig. 2.6
  - The cabin doors are of the gull-wing type, while the older version had common doors, hinged at the front-facing edge.

Besides, the connection between stick and ailerons, which was a bar in the previous version, has been replaced by cables and pulleys.

No changes have been applied to:

- Airfoil, wing geometry and ratio between flap and aileron span;

(a) (b)

Figure 2.4: The new (2.4a) and the old (2.4b) elevator and trim tab.

(a) (b)

Figure 2.5: The new (2.5a) and the old (2.5b) nose.

- Airfoil and surface of the horizontal tail plane;
- Rudder.

2.2 Changes of configuration during the test

During the test campaign, due to the prototype nature of the aircraft, the manufacturer improved some changes to the aircraft configuration in order to explore different constructive solutions. The different configurations are the following, in chronological order:

1. Wings with vortex generators along the whole length. Static port in conventional position on the right and left side. Whool wires on the fuselage;

(a) (b)

Figure 2.6: The new (2.6a) and the old (2.6b) landing gear.

2. Removal of vortex generators, except in the semi-span from the wing strut to the tip. Static port moved inside the cabin. Removal of whool wires;

3. Removal of more vortex generators, in order to leave them in front of the aileron only. Dihedral reduced to 0.5° and propeller pitch increased of 0.5°.

The above described configurations are always referred in this work as *aircraft configurations*, not to be confused with cruise, take-off or landing configuration, which are indicated simply as *configurations*. When not specified otherwise, all the tests have been performed with the third and last aircraft configuration.

2.3 Test area

All the tests have been conducted in the sky above *Aviosuperficie Club Astra*, located in Mezzana Bigli, close to Pavia, Italy. The airstrip is a 900 m, grass, short-mown one, with orientation 02-20. The area of the test has been limited between the ENI refinery, in front of the airstrip for 020-headed take-off and Po river, which runs 2 km south of the airfield. All the flights have been performed in summer: the hot weather typical of the test area led to frequent thermal streams. The solution was to fly over the Po river, whose area should be less inclined to produce thermal lifts thanks to the presence of cooler water.

2.4 Test limitations

The first limit the tests are subject to is the altitude: the maximum altitude in the test area must not exceed 2500 ft/asl. Secondly, all the test flights are subject to the weather conditions. Visual flight rules prescribe a minimum of 5 km of visibility and 1.5 km of separation from the clouds. Luckily, all the flights were performed during summer and the meteorological conditions were always suitable for visual flight without the necessity to delay the schedule.

Chapter 3

Test instrumentation

This chapter enumerates all the features and the sensors implemented in the Flight Test Instrumentation of the campaign. The suite implements a set of sensors in order to provide the time history of all the parameters needed to perform a fully satisfactory analysis of the flights and other essential components to make the FTI fully serviceable. For the best FTI use, some ground sensors have to be placed, too: a telemetry station followed real time the aircraft and a meteorological station assured the knowledge of all the ambient parameters for the post processing analysis.

Eventually, most of the data need a filtering in order to be readable without losing any important information for the post processing analysis; the filtering is briefly detailed in the last part of the chapter.

3.1 Mnemosine Mk-V

The flight test instrumentation is the *Mnemosine Mk-V*, fifth generation of the FTI developed at *Politecnico di Milano*, at the Department of Aerospace Engineering, by professor Alberto Rolando. The architecture of the FTI is based on a central unit, connected with all the sensors, able to record 35 parameters on a removable SD card. The sensor suite includes:

- Inertial measurement unit (XSENS);
- GPS unit (GPS);
- Flight control position sensors (ADC);
- Air data sensors (ADS);
- Stick force sensor.

Figure 3.1: Mnemosine main unit, housed in the luggage compartment behind the seats.

Additionally, the FTI is completed with a dashboard to switch on and off the registration and a kneepad, to offer an immediate view of some parameters chosen by the user and to mark the time when the test points start and end. Tab. 3.1 summarizes the sample frequencies of each FTI unit.

Table 3.1: Sample frequency for each family of sensors.

Sensor family	Freq. [Hz]
XSENS	50
GPS	2
ADC	10
ADS	10
Stick force	10

For a complete overview of the FTI instrumentation, the reader might refer to [9] and [22]. The improvement made for the current flight test campaign concerns the air data boom, which is a brand new instrument acquired in May 2017 by the *Politecnico di Milano DAer*; its details are enumerated in 3.1.4.

3.1.1 Inertial measurements unit

The inertial measurement unit is demanded to a iMAR iμVRU, which features a 3 MEMS gyro axes, 3 MEMS accelerometer axes, barometer, 3D magnetometer, GPS and odometer interface. The integrated Kalman filter based data fusion provides secured attitude even at lost of some of the aiding data. The outputs provided are:

- Acceleration along the three axis;
- Angular velocity along the three axis;
- Euler angles;

Full technical documentation is available on the website, at [32].

3.1.2 GPS unit

The GPS module is used both as positioning sensor and time source. The GPS featured for Mnemosine Mk-V is the LEA-6N, a standalone positioning module which combines an extensive array of features with flexible connectivity options. LEA-6N supports GPS, GLONASS and QZSS modules.

3.1.3 Flight control position sensors

Position indication of rudder, elevator, ailerons, flaps comes from a set of LX-PA-3.8 wire potentiometer. The moving part is attached to the connection between bar and surface, while the body is fixed to the cabin floor. The cable movement pulls a spring attached to a potentiometer. The cable spring maintains a constant pull back tension on the cable. These sensors are particularly easy to integrate and guarantee a good level of safety, since the wire might be broken if they create an obstacle for the deflection of the control surfaces. An example of potentiometer is reported in Fig. 3.2.

3.1.4 Air data module

All the air data sensors are housed on a 100400 Mini Airdata boom, whose sketch and components are represented in Fig. 3.3. In particular, the boom hosts a static probe and a total pressure one, an angle of attack sensor and an angle of sideslip one. The entire air data module is composed by a Olimex STM32-H107, two pressure transducers (static and dynamic air pressure), one resistance to detect the temperature and an analogue signal conditioning

Figure 3.2: One of the potentiometers installed on the G70 TRAIL.

module for wind angle measures. The module is the only one stored outside the main FTI unit, in order to avoid long linkages between the probes and the transducers.

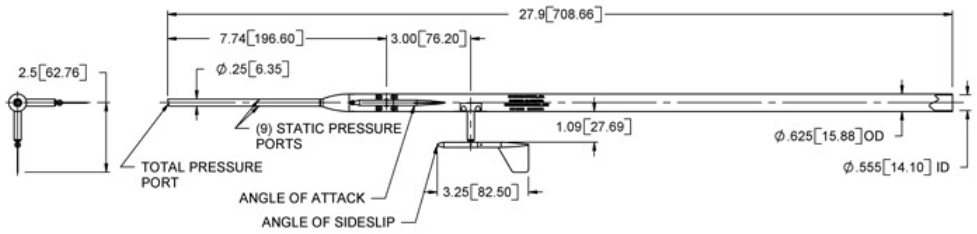

Figure 3.3: The sketch of the air data boom installed under the right wing.

3.1.5 Stick force sensor

Stick force is acquired through the Futek MU300, a small 3D load cell, coupled with a HX711 load cell amplifier to get measurable data. The load cell senses the stick force in both directions, while the load cell amplifier allows complete processing of the signal. The sensor is mounted right on the stick bar, as shown in Fig. 3.5.

Figure 3.4: The air data boom.

Figure 3.5: The instrumented stick bar, with the stick force sensor.

3.1.6 On-board interface: kneepad and dashboard

The kneepad in use with the Mnemosine FTI has three commands and a screen: a switch, a button and a knob (Fig. 3.6). The first opens and closes the TOP, in order to visualize on the mission time line the beginning and the end of each test point. The second marks a specific event on the time line.

The last one switches from one page to the other of the small screen on the kneepad, which shows real-time parameters to the FTE.

Figure 3.6: Mnemosine Mk-V kneepad.

The control board is installed in a position accessible to the FTE to properly turn on and off the whole FTI. On the dashboard there are five switches:

- MASTER, to turn on and off the system;
- TELEMETRY, to control the power to the telemetry transceiver;
- AUX, to supply the FTI from the external battery;
- A/C, to supply the FTI from the aircraft electrical system;
- RECORD, to start and stop data recording.

3.2 Telemetry station

The purpose of a telemetry system is to reliably and transparently convey measurement information from a remotely located data generating source to the user. During the test campaign most of the tests were flown under the supervision of a telemetry station, which communicated with the aircraft by means of a WiFi steerable telemetry antenna on the ground (Fig. 3.7a). The aircraft was equipped with two WiFi antennas under the fuselage and had to be always in line of sight with the ground antenna in order to ensure a continuous data transmission.

If the telemetry station is continuously overseen, the observer has an immediate confirmation if some FTI channel is not recorded properly or, worse, the FTI is not working at all. During the campaign it happened that some FTI cable was disconnected during the flight or the FTI was not recording because of a malfunctioning: without the telemetry station, entire flights would have performed without any registration or with some dark channels, with no attempt of the crew to solve the problem on-board.

3.3 Meteorological station

The meteo station (Fig. 3.7b) is an equipment developed by Eng. Federico Rossi and was employed during the flight test campaign to record the data requested for the reduction formulas of take-off and landing performance. The equipment of the station is made of:

- a Davis anemometer for wind speed and direction;
- a solar radiation shield beneath which a temperature sensor, an humidity sensor and an ultra compact absolute piezoresistive pressure sensor are placed;
- a GPS unit.

Data coming from the meteo station are recorded on a micro SD card located inside the station itself and are synchronized with the main FTI recording thanks to the GPS time. The position of the meteo station should be in proximity of the runway without being an obstacle to the operations of the airplanes and far enough from building, approximately 100 m. For further information refer to [18].

(a) (b)

Figure 3.7: Ground antennas: telemetry (3.7a) and meteo (3.7b).

3.4 Data filtering

Data from FTI have been filtered with a simple Butterworth filter in the Matlab environment by mean of the function `filtfilt`, which processes the data forwards and backwards and compensates the delay introduced by the filtering. Butterworth filter is implemented in Matlab with the function:

`[b,a]=butter(order,`ω_n`)`

where:

- b and a are respectively the numerator and denominator coefficients of the filter transfer function, as output;
- *order* is the filter order;
- ω_n is the normalized cut-off frequency, namely $\omega_n = \dfrac{f_C}{f_S/2}$.

Sample frequencies f_S are the ones reported in Tab. 3.1, while cut-off frequency f_C has been set as 1 Hz for all the data: 1 second dynamics are enough to analyse all the data without losing flight information and to cut off all the noise coming from structural vibration of the aircraft. With higher cut-off frequencies the time history is dirty of noise oscillations, while with lower frequencies there is the risk to lose information.

Filter order has been chosen with trial and error method: first and second order filters does not reach all the data peaks, making the filtered time history not sufficiently accurate; from 3rd order onwards the accuracy of the filter is enough for all the data, therefore a 4th order filter has been chosen in order not to increase fruitlessly the computational cost of the post processing routine.

An example of filtering is hereby reported, regarding the XSENS channel, divided into accelerometer, angular velocity and Euler angles measures; it is taken from the stall test in LND configuration of flight 01.1106. The code receives as input:

- $f_S = 50$;
- $f_C = 1$;
- `order=4`;

hence:

$$\texttt{[b,a]=butter(order,}\frac{f_C}{f_S/2}\texttt{)}$$
$$\texttt{filtered\_data=filtfilt(b,a,raw\_data)}$$

The filter obtained is characterized by the magnitude function represented in Fig. 3.8. The filter has been applied using a zero-delay filtering technique (`filtfilt` MATLAB function), therefore the phase plot can be omitted.

Figg. 3.9, 3.10, 3.11 show the comparison between the original and the filtered signal for each of the channel of the XSENS data set. It is remarkable the good quality of the Euler angles measure, whose filtered signal coincides with the original one for every sample.

In addition, the FFT of the signal can be obtained in the MATLAB environment. The graphs of Fig. 3.12 plot the power spectral density of the acceleration on the y-axis and the frequency in Hertz on the x-axis; the same graphs are obtainable for the other measures, but for sake of brevity only the acceleration one is hereby reported. It is clear how the major portion of energy to the global signal spectrum is given by frequencies around 0.5 Hz, which are the ones of our interest. The Y signal is way dirtier on the frequency spectrum with respect to the other two channels: probably the structural vibrations were transmitted to the inside fuselage surface where the accelerometer was attached in the transversal direction more than in the horizontal and vertical.

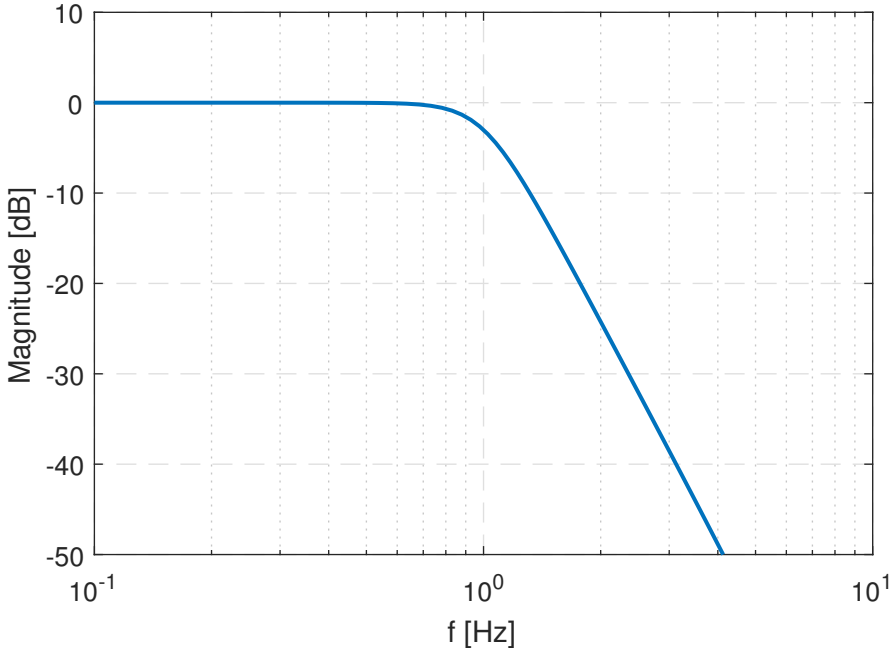

Figure 3.8: Butterworth filter for accelerometer data filtering.

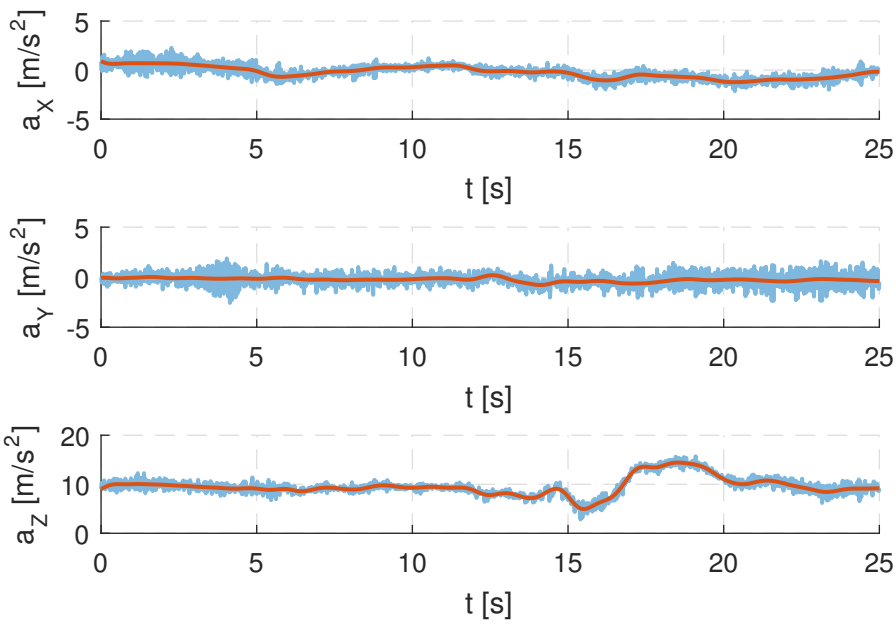

Figure 3.9: Difference between original and filtered signal for acceleration channels.

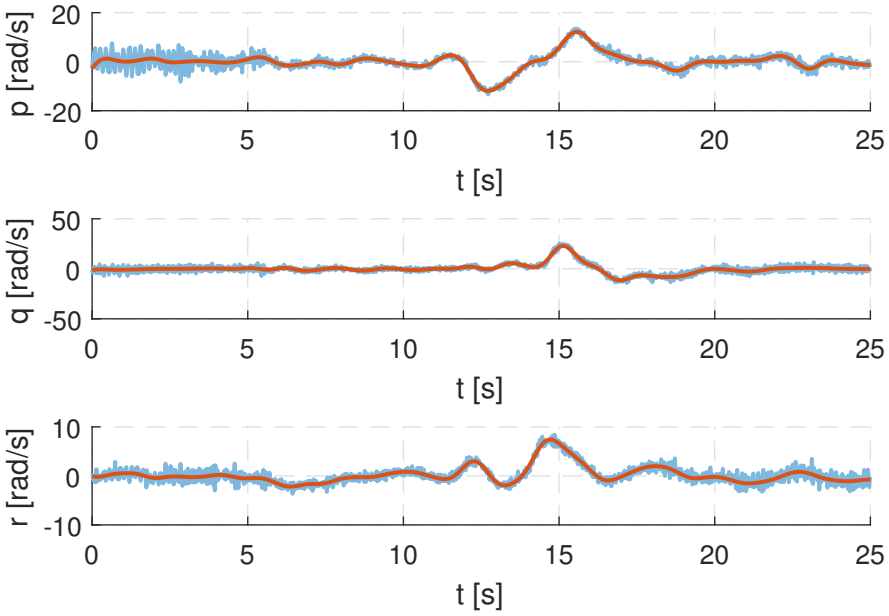

Figure 3.10: Difference between original and filtered signal for angular velocity channels.

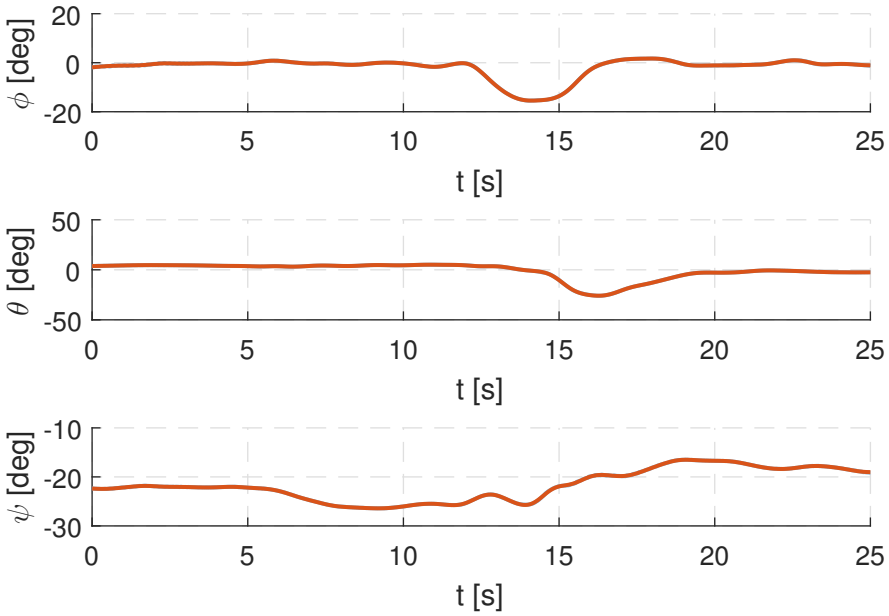

Figure 3.11: Difference between original and filtered signal for Euler angles channels.

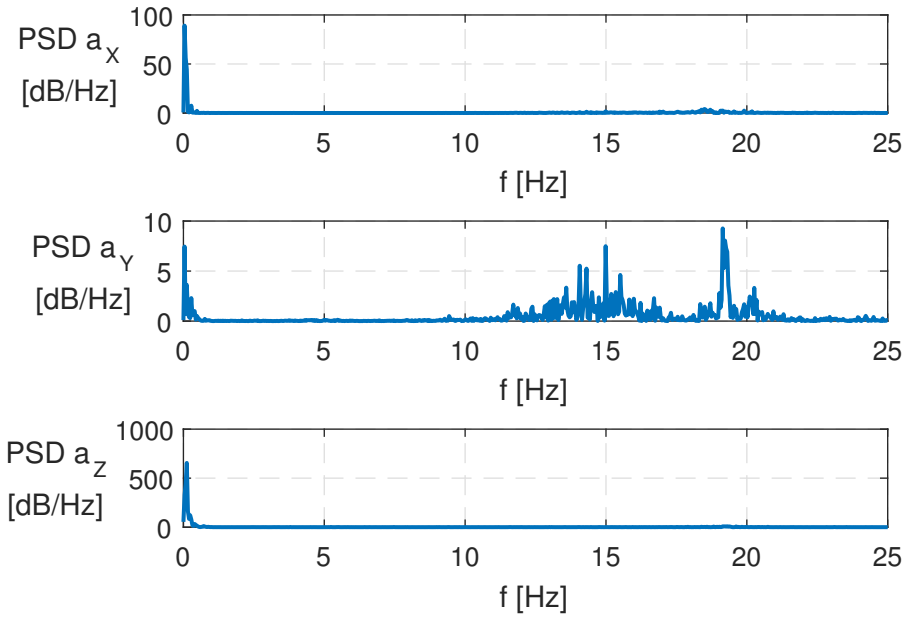

Figure 3.12: FFT of the acceleration channels of the XSENS sensor suite.

Chapter 4

Campaign introduction and preliminary analysis

Before starting the real campaign, some work has been performed in order to assure the correct development of the campaign itself. The first phase was devoted to the normative behind the UL flight, in particular to the requirements listed by the reference law LTF-UL. The first flights have been executed by the author in order to explore the general behaviour of the aircraft, while the test phase referred to LTF-UL has been executed in collaboration with the *Flight testing* course students.

For a meaningful post processing analysis, CAS has to be accurately determined, starting from either the indicated airspeed on the on-board anemometer or the pitot boom indication; therefore, air data calibration has been performed. Moreover, a Tornado model of the aircraft has been developed in order to check neutral point position and to obtain a first approximation of the short period frequency before the test.

4.1 Regulatory background

The results of the flight test campaign have been compared with the prescriptions of the German LTF-UL regulation. In order to understand why *Ing. Nando Groppo SRL* certifies its aircraft according to the German law, a brief digression about the UL airplanes regulation is needed.

The Italian regulation about UL flight is contained in the *Legge del 25 marzo 1985, n. 106* [4] and in the *Decreto del Presidente della Repubblica, 9 luglio 2010, n. 133* (DPR 133) [3]. The last one divides the UL airplanes in *basic* and *advanced* and defines all the test points that must be accomplished to certify the aircraft according to the Italian law. The DULV, *German*

Ultralight Association, is responsible of the UL certification with the LTF-UL as well as AeCI, *Aero Club Italia*, is responsible to release the certification in Italy. The difference between the Italian and the German regulation is that the latter is way more detailed and structured than the former; in addition, once the compliance to LTF-UL has been demonstrated, it is consequent the compliance to DPR 133. This is the main reason why *Ing. Nando Groppo SRL* made the choice to certify its aircraft according to the LTF-UL. In addition, *Groppo* airplanes are appreciated abroad and in particular in Germany, so the choice has reasons linked to strategic marketing, too.

4.2 Test campaign planning and synopsis

The first flights, executed in May, 14th and 22nd, and in June, 2nd, were planned with the aim to test the general behaviour of the aircraft and, moreover, to make lighter the test points executed by the students:

- **Air data calibration**: first test to perform in order to know CAS with respect to indicated airspeed;
- **Climb and glide test**: exploratory test to assess V_{BG}, V_{SC} and V_{FC} and to validate the climbing ability of the aircraft with full throttle;
- **Wind-up turn**: the aim is to verify the positive gradient between elevator deflection and load factor and to make sure that the aircraft remains far away its structural limits;
- **Roll manoeuvrability**: the test aims at checking the correct functioning of the new aileron linkages, which have changed with respect to the former G70 (2.1.2);
- **Stall behaviour test**: recovery ability of the aircraft has to be qualitatively verified in order to guarantee a safe stall speed test in the following flights.

The other flights were planned in order to explore the widest spectrum of LTF-UL tests; in detail, tests during June, 10th, 11th and 17th have been scheduled with the following test points:

- **Take-off and landing distance**;
- **Stall speed determination**, in CR, TO and LND configuration;
- **Climb and glide test** in CR and TO configuration;

- **Static stability**, both in longitudinal and lateral directional plane, in CR, TO and LND configuration;
- **Dynamic stability**, with phugoid and Dutch roll excitation, in CR and LND configuration.

Due to time constraints, static lateral-directional stability has been verified only in CR and TO configuration. During the campaign the following test points were added:

- **Trim test**, in order to guarantee the trimmability of the aircraft and to experimentally obtain the stick-fixed neutral point position. This last test must be executed at least with three different CG positions;
- **Short period excitation**, in order to have a wider analysis of the dynamic stability of the aircraft and to experimentally calculate the correspondent frequency for further works.

An additional flight has been executed in July, 15th, to test climbing ability at altitudes substantially different from the ones performed in the planned tests, always respecting the local limitations for UL flight.

Tab. 4.1 reports all the flight tests executed during the campaign. For the sake of brevity, all the flights are categorized with numbers like NN.DDMM, where DD is the day number, MM the month number, NN the progressive number of the flight in the day. In short, the 2017 campaign can be summarized with the following data:

- 9 days devoted to flight test activity;
- 27 test flights with an average duration of 41 minutes each;
- 19 hours of flight;
- 123 MB of post processed flight data.

Table 4.1: Test campaign synoptic table.

Flight ID	**Aircraft conf.**	**Date**	**TO time (UTC)**	**Duration (min)**	**Test Items**	**FTE**	**TP**
01.1405	1	2017-05-14	12:51	49	• Anemometer calibration CR and LND	Oldani	Quaglietta
02.1405	1	2017-05-14	14:30	53	• Sawtooth climb • Sawtooth glide	Oldani	Quaglietta
01.2005	1	2017-05-20	12:15	45	• Anemometer calibration CR	Oldani	Quaglietta
02.2005	1	2017-05-20	14:22	38	• Trim test • Maximum speed test for static probe check • Wind-up turn • Roll manoeuvrability test	Oldani	Quaglietta
01.0206	2	2017-06-02	12:50	35	• Anemometer calibration CR • Stall behaviour test (CR,TO,LND)	Oldani	Quaglietta
02.0206	2	2017-06-02	14:06	46	• Sawtooth climb • Sawtooth glide • Maximum speed test • Wind-up turn	Oldani	Quaglietta

Flight ID	Aircraft conf.	Date	TO time (UTC)	Duration (min)	Test Items	FTE	TP
01.1006	3	2017-06-10	08:52	48	• Take-off distance • Sawtooth glides • Dutch Roll (CR) • Landing distance	Bordone	Quaglietta
02.1006	3	2017-06-10	09:51	44	• Take-off distance • Sawtooth glides • Dutch Roll (CR) • Short period test • Landing distance	Bay	Quaglietta
03.1006	3	2017-06-10	11:04	50	• Take-off distance • Sawtooth climbs (TO) • Phugoid (LND) • Landing distance	Di Girolamo	Quaglietta
04.1006	3	2017-06-10	13:00	51	• Take-off distance • Sawtooth climbs (TO) • Phugoid (LND) • Landing distance	Musacchio	Quaglietta
05.1006	3	2017-06-10	14:34	42	• Take-off distance • Sawtooth climbs (CR) • Phugoid (CR) • Landing distance	Bavetta	Quaglietta

Flight ID	Aircraft conf.	Date	TO time (UTC)	Duration (min)	Test Items	FTE	TP
06.1006	3	2017-06-10	15:37	44	• Take-off distance • Sawtooth climbs (CR) • Phugoid (CR) • Landing distance	Cannavò	Quaglietta
07.1006	3	2017-06-10	16:41	45	• Take-off distance • Sawtooth glides (TO) • SHSS (CR) • Landing distance	Facchi	Quaglietta
01.1106	3	2017-06-11	08:06	51	• Take-off distance • Speed stability (LND) • Stall test (LND) • Landing distance	Spada	Quaglietta
02.1106	3	2017-06-11	09:10	30	• Take-off distance • Speed stability (LND) • Stall test (LND) • Landing distance	Sesso	Quaglietta
03.1106	3	2017-06-11	10:09	30	• Take-off distance • Speed stability (TO) • Stall test (TO) • Landing distance	Montanini	Quaglietta

Flight ID	Aircraft conf.	Date	TO time (UTC)	Duration (min)	Test Items	FTE	TP
04.1106	3	2017-06-11	10:48	34	• Take-off distance • Speed stability (TO) • Stall test (TO) • Landing distance	Giuri	Quaglietta
05.1106	3	2017-06-11	13:06	46	• Take-off distance • Sawtooth climbs (TO) • SHSS (TO) • Landing distance	Bigoni	Quaglietta
06.1106	3	2017-06-11	14:15	45	• Take-off distance • Sawtooth climbs (TO) • SHSS (TO) • Landing distance	Ibrahim	Quaglietta
07.1106	3	2017-06-11	15:47	40	• Take-off distance • Sawtooth climbs (CR) • Dutch Roll (LND) • Landing distance	Poiana	Quaglietta
08.1106	3	2017-06-11	16:35	28	• Take-off distance • Sawtooth climbs (CR) • Dutch Roll (LND) • Landing distance	Montorfano	Quaglietta

Flight ID	Aircraft conf.	Date	TO time (UTC)	Duration (min)	Test Items	FTE	TP
01.1706	3	2017-06-17	08:22	44	• Take-off distance • Sawtooth glides (TO) • SHSS (CR) • Landing distance	Vassallo	Quaglietta
02.1706	3	2017-06-17	09:21	35	• Take-off distance • Stall test (CR) • Speed stability (CR) • Landing distance	D'Ascenzo	Quaglietta
03.1706	3	2017-06-17	10:11	45	• Take-off distance • Stall test (CR) • Speed stability (CR) • Trim test • Landing distance	Arditi	Quaglietta
04.1706	3	2017-06-17	13:39	18	• Trim test	D'Ascenzo	Quaglietta
05.1706	3	2017-06-17	14:30	29	• Trim test • Short period test	Oldani	Quaglietta
01.1507	3	2017-07-15	09:05	56	• Sawtooth climbs (CR) • Sawtooth glides (CR)	Oldani	Quaglietta

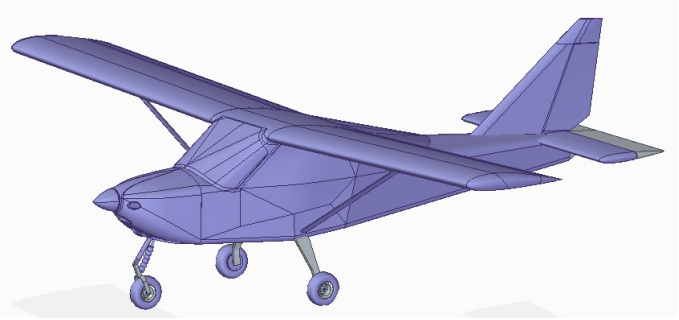

Figure 4.1: TRAIL G70 CAD model.

4.3 Tornado model of the aircraft

Tornado is a Vortex-Lattice software implemented in Matlab for linear aerodynamic wing design applications. Lifting surfaces are modelled as thin plates and, with the fuselage approximated as two plates crossed in the middle, it is possible to obtain a quite accurate model of the aircraft in order to calculate the aerodynamic derivatives for a wide range of aircraft geometries. All the measures for the Tornado model have been taken from the CAD model of the air vehicle, which is reported in Fig. 4.1. The aircraft has been modelled in Tornado with the same reference attitude used for the weighing process, in order to get a position of the neutral point consistent with the CG location along the longitudinal axis obtained in the weighing. All the lifting surfaces have been panelled according to a possible trade-off between the computational cost and the accuracy of the results.

Fig. 4.2 reports the resulting panellization, while Fig. 4.3 shows the top view of the aircraft modelled in Tornado. The model has been employed for a validation of the neutral point position (9.1) and for a preliminary estimation the aerodynamic derivatives of the aircraft in the section dedicated to short period frequency evaluation (8.1).

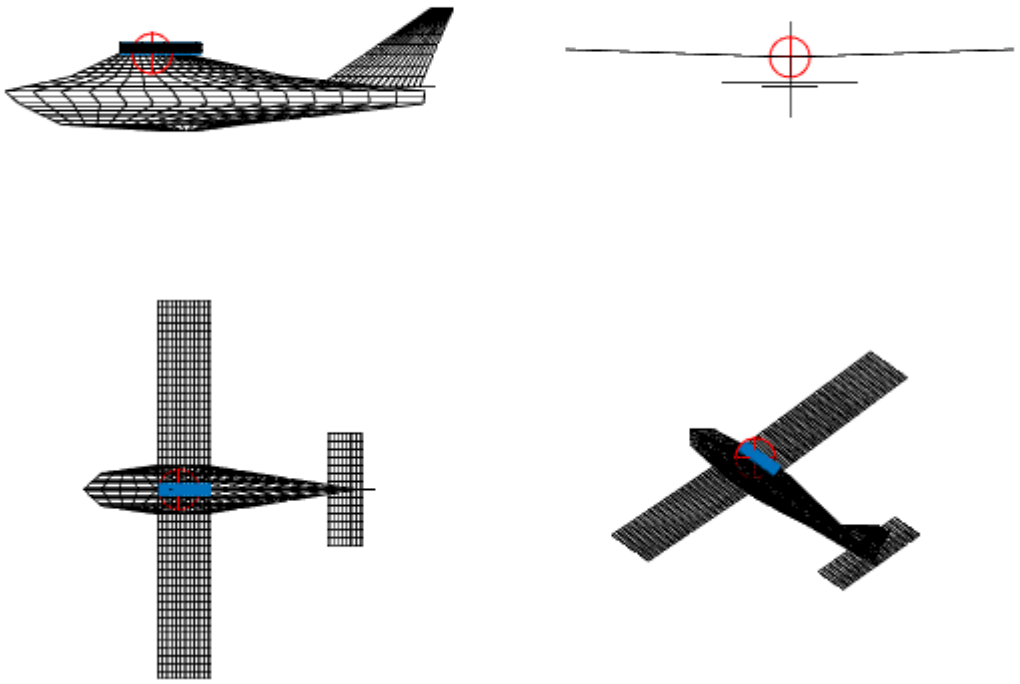

Figure 4.2: TRAIL G70 Tornado model four views.

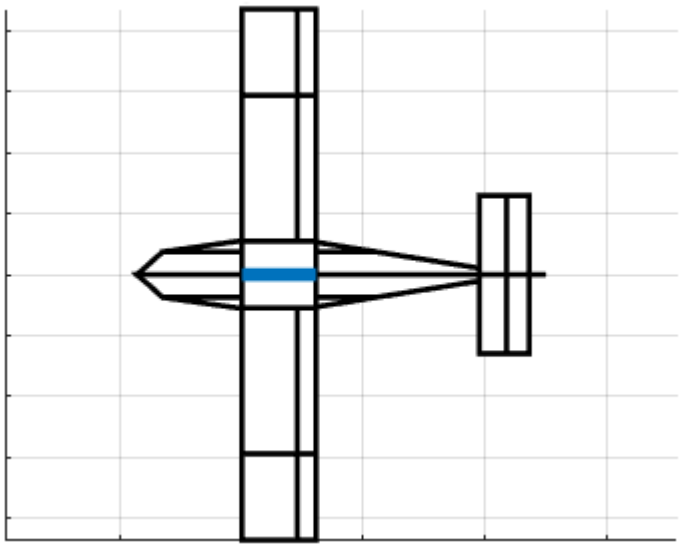

Figure 4.3: TRAIL G70 Tornado model top view.

4.4 Air data calibration

4.4.1 Introduction

Calibration of the devices devoted to airspeed indication, namely on-board anemometer and pitot boom, is of paramount importance to have a precise and reliable indication of CAS. Anemometer calibration has the purpose to measure and mitigate, if necessary, the error acting on the static probe. Pressure distribution along the fuselage (*position error*) provides an error to the static port, located symmetrically on both sides of the G70 ahead the lateral doors; in this area the air flow is influenced by the propeller.

During the past test campaign, it was proved that the indication of airspeed suffered a static probe error which made the on-board anemometer out of compliance according to the limits dictated by LTF-UL. The FTI pitot boom has already been calibrated before the installation and it is located in a region which is ideally far from the disturbed air flow. Practically, even the static probe of the pitot boom might suffer of position error, which will be identified in this section and, most likely, will be relatively small. Both anemometer and pitot boom produce a IAS, which is by definition the speed indicated by mean of an instrument without the position error indication. IAS in this work is used in all the cases referred to the anemometer indication of airspeed, since the one indicated by the pitot boom has already been corrected according to the calibration of this section.

4.4.2 Test objectives

LTF-UL 1323 has precise requisites on the error between the speed indicated on the anemometer and the calibrated one, namely the maximum pitot static error of the aircraft must not exceed $\pm$ *6 km/h or* $\pm 5\%$*, whichever is greater, throughout the following speed range:*

- $1.2V_{S_1}$ *to* V_{NE} *with flaps retracted;*
- $1.2V_{S_1}$ *to* V_{FE} *with flaps extended.*

The FTI pitot boom does not have any limitation of error according to the normative, but it is desirable that pitot IAS is reliable for almost all the flight tests.

4.4.3 Test execution

Procedure for anemometer calibration is the GPS-PEC (Position Error Calibration). The error is reconstructed with a comparison of IAS, which is read

on the anemometer on board, and TAS, which is identified with the GPS. Since the GPS can only measure GS, a way to know wind speed and direction is requested. The procedure leading to the knowledge of wind speed and direction consists in flying three legs, at the same IAS, with a track significantly different among them. A geometrical problem raises, that is a system with three equations, made by the three wind triangles, and three unknowns, namely TAS, wind speed and direction. A graphical representation of the wind triangles is shown in Fig. 4.4.

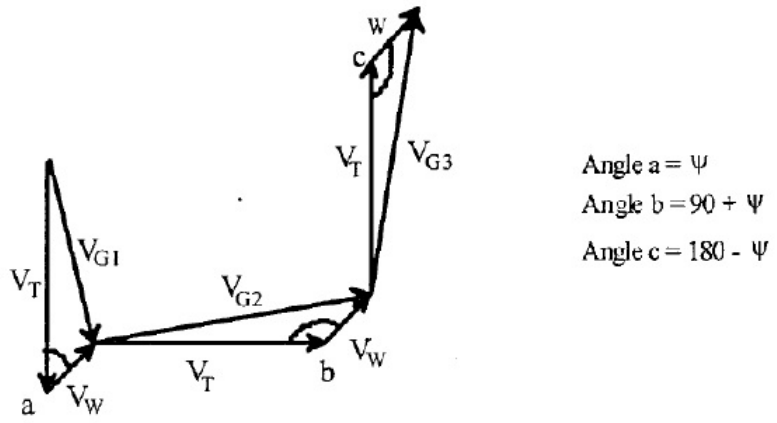

Figure 4.4: Wind triangle problem for GPS-PEC air data calibration.

Assuming constant wind speed and direction during the legs and constant IAS, the system can be solved. For a more reliable result, four legs have been flown, leading to a system with four equations and three unknowns, which is solved with the least square method.
From the comparison between TAS and IAS, with the knowledge of pressure altitude and OAT, it is possible to calculate the pressure error and the relation between IAS and CAS, keeping in mind that, for the range of speed and altitudes of interests in this work, the assumption EAS=CAS is always more than reliable. The anemometer calibration test has been executed in the first flight 01.1405. Due to the not satisfying result, has been repeated in flight 01.2005 and again in flight 01.0206.

FTI pitot boom speed calibration should follow the same procedure of the anemometer one, but at the time the latter was executed, no pitot boom was installed on the aircraft. Thus, the pitot calibration has been executed ex-post by mean of the trimmed flights 03.1706, 04.1706, 05.1706: the anemometer IAS, constant during the test, allows to calculate the CAS thanks to the anemometer calibration; therefore, the comparison between CAS and pitot boom IAS provides the desired result.

4.4.4 Test results

Anemometer calibration

Flights 01.1405 and 01.2005 showed a dramatic high error in the airspeed indication, whose details are enumerated in Appendix A. The decision of the manufacturer, before flight 01.0206, has been to remove the static probe from the fuselage side and to put it in the cabin and perform the rest of the campaign with this configuration, with the purpose to try to solve the problem in future. This solution allowed to reduce the static pressure error during the flight test campaign.

Results are shown in Fig. 4.5. The IAS is a good approximation of the CAS between 100 and 120 km/h, while is lower in the low-speed range, which is good, because it keeps the aircraft far from the stall condition. There is no sense to talk about certification limits for this test, because the static probe inside the cabin is not accepted by the certifier; however, as an example, the compliance graph is reported in Fig. 4.6: the red lines represent the error limits of LTF-UL, as explained in 4.4.2, with the linear regression between the test points (IAS error versus IAS). The error exceeds the LTF-UL limits in the medium-high range of speed, above 150 km/h.

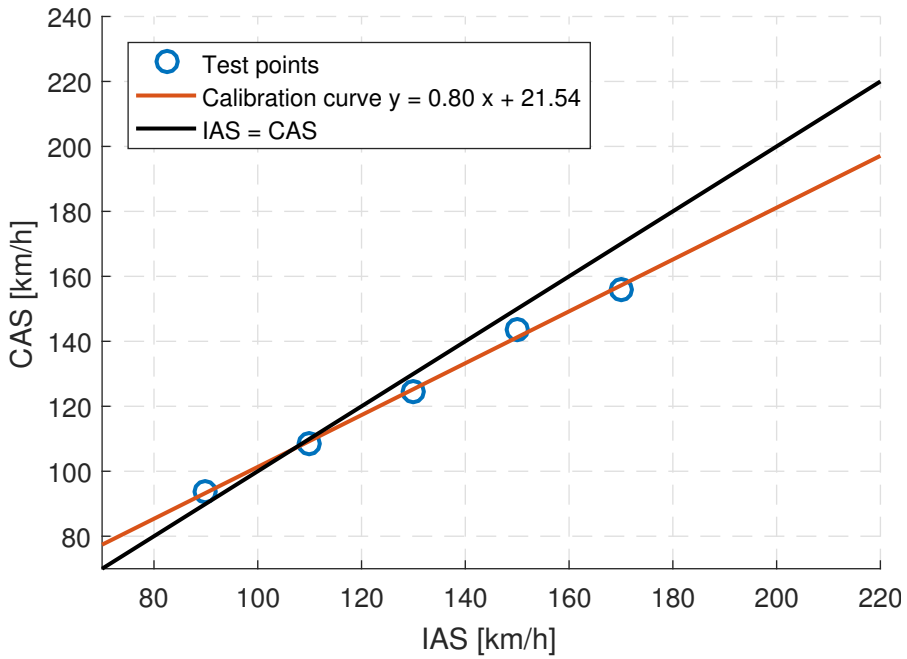

Figure 4.5: Calibration line for G70 aircraft, as resulted in flight 01.0206.

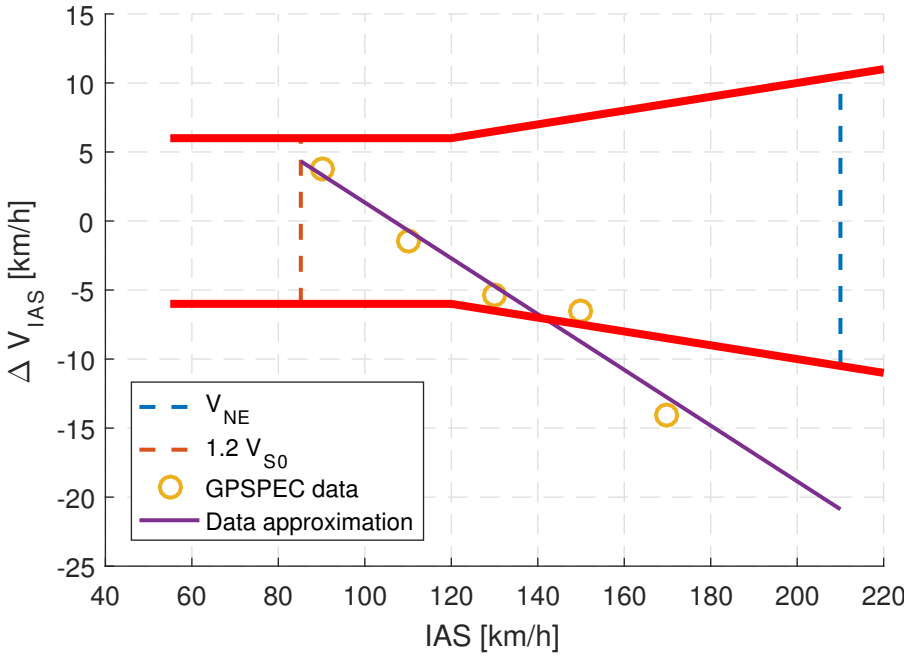

Figure 4.6: IAS error on G70 and limits of LTF-UL, as resulted in flight 01.0206.

FTI pitot boom calibration

The result of the FTI pitot boom calibration is shown in Fig. 4.7. The error due to the FTI boom position, in the range of speed of interest during the flight, is +4/-2 km/h, as demonstrated in Fig. 4.8. The error points have been fitted with a second order approximation, since a linear fitting would have generated a higher mean quadratic error with the experimental points; third or more order approximations do not produce better results in terms of mean quadratic error.

4.4.5 Conclusions

Even in the new version of the aircraft, the anemometer has an important error due to the pressure distribution along the fuselage. However, the static probe inside the cockpit is a not valid solution for certification purposes: the manufacturer has to correct the static probe error before the certification request. For reasons of time, all the tests of this work have been performed with the static probe in the cockpit. Generally, the first solution adopted to solve an abnormal static pressure indication is to apply, around the port, a flap, or "tooth", which creates a stagnation point around the probe; this

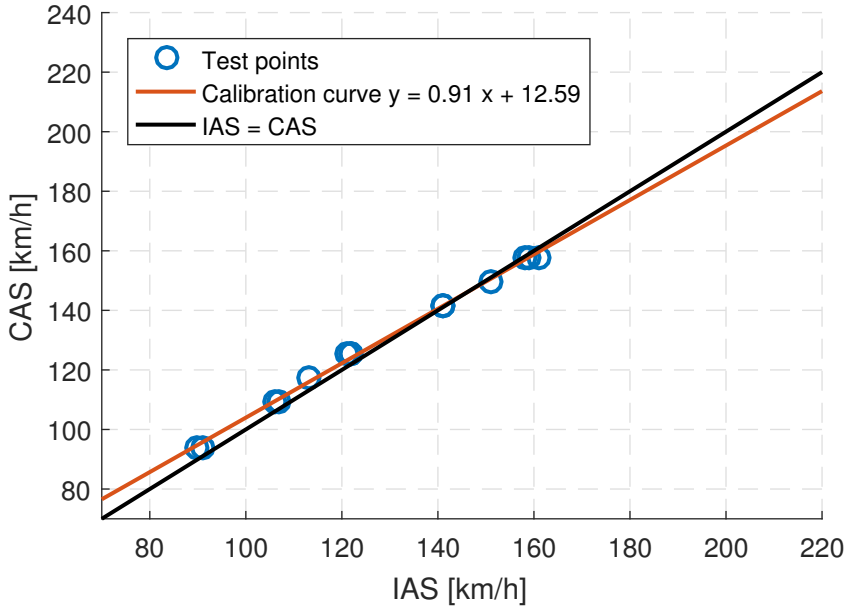

Figure 4.7: Calibration line for the FTI pitot boom during the G70 flight test campaign.

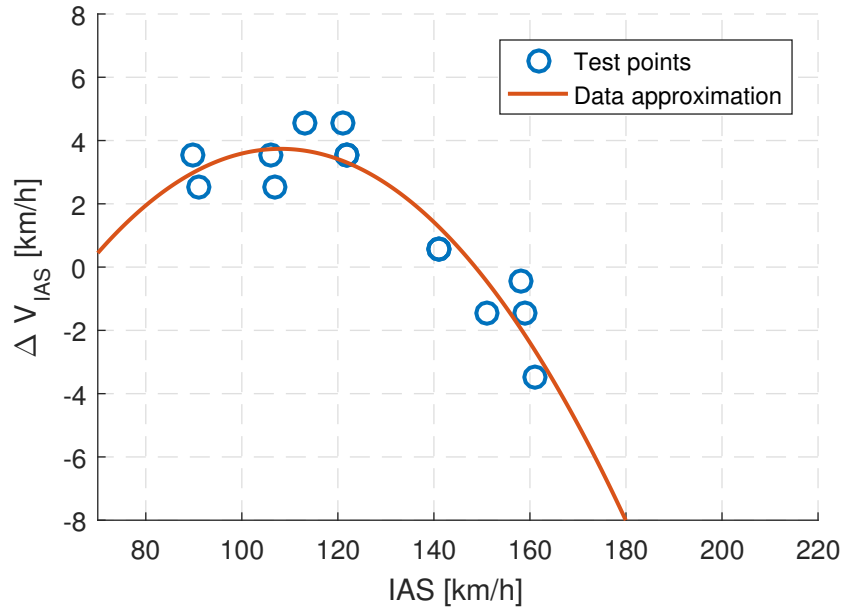

Figure 4.8: CAS error on the FTI pitot boom versus flight speed.

solution will be implemented once this flight test campaign would be over.

For further air data calibrations, the use of the native EFIS screen is discouraged, since the GPS track is constantly equal to the heading. The

AvMap display, installed in the middle of the instrument panel, is regarded as more trustworthy.

The FTI pitot boom error is, as expected, low. In order to reduce the propeller influence on the static port of the pitot boom, a possible solution is to move it toward the wing tip, which makes an additional problem arise: as a matter of fact, pitot boom support installation takes advantage of the connection of the wing beam on the intrados and its shift will definitely require to drill the wing in at least two points. Hence, for ease of installing, the pitot boom cannot be shifted and its static pressure error must be determined.

Chapter 5

Performance test

The performance evaluation test aims at defining numerically and qualitatively the behaviour of the aircraft in terms of stall speed, climb, take-off and landing. The analysis shown how the stall speed is higher than the one of the previous G70 version, but the aircraft behaviour and reaction at the stall is fully satisfactory. Climb performance is more than acceptable: the aerodynamic improvement of the new G70 and the new propeller make the airplane very fast and responsive during the climb phase. Take-off and landing performance confirms the good results previously obtained.

5.1 Tools for data reduction

Engine has an important influence on the overall airplane performance. Consequently, there is the need to know the power available during the test points, by means of the brake horsepower P_b and the propeller efficiency η_p.

Brake horsepower

Brake horsepower is found with the engine chart provided by the manufacturer ([7]), which reports the graphs to find out the real day power given the RPM value, test altitude and actual temperature.

Propeller efficiency

In the UL aircraft world, it is very difficult to find accurate data sheets about propellers and, therefore, efficiency evaluation might be very difficult. French manufacturer E-Props provides on its website a software to calculate the efficiency of their carbon-made propellers, requiring as input:

- propeller diameter,

- number of blades,
- engine speed (RPM),
- reducer ratio,
- engine real power,
- flight speed,
- air density.

Since the software is provided by a propeller manufacturer, there is not any indication about the method which is implemented to calculate the efficiency; furthermore, the website specifies an accuracy of ±5% on the final result. Although the actual limitations of the method, the propeller mounted on the G70 is carbon-made, three blades, diameter as much as the propeller of the software, which makes its result not dissimilar from the one expected.

5.2 Stall speed determination

5.2.1 Introduction

This section is going to determine the stall speed of the aircraft in CR, TO and LND configurations. Many features of the new G70 will definitely influence the stall speed, as the enlarged fuselage and the better aerodynamic shape, whose contribution to the stall speed is ambiguous and a definite prediction on how the new aircraft will behave at the stall is impossible. However, there is one characteristic of the new G70 which will definitely have a great impact on stall speed, that is the reduced number of vortex generators. Whereas in the old version all the wing span was occupied by a row of vortex generators, the new prototype mounts them only in front of the aileron. It is admissible to forecast a higher stall speed on the TRAIL G70 with respect to the old aircraft version.

5.2.2 Test objectives

LTF-UL defines the stalling speeds V_{S0} and V_{S1} in paragraph 49 and explain how to recognize stall in paragraph 201. In particular *V_{S0} is the stall speed, if obtainable, or the minimum steady speed, in km/h (CAS), at which the airplane is controllable with the engine power at idle (throttle closed) or shut down.* During the test the aircraft must be in landing configuration and

the weight equivalent to the maximum weight. V_{S1} is the same, but with the aeroplane in the condition existing in the test in which V_{S1} is being used. According to the first LTF-UL paragraph, V_{S0} must not exceed 65 km/h. LTF-UL 201 completes what specified in the previous paragraph with the identification of the stall, *shown by an uncontrollable downward or sideward pitching movement of the aeroplane* or recognized when the longitudinal control reaches its maximum deflection. Standard deceleration at which stall speed has to be determined is 2 km/h/s.

5.2.3 Test execution

In order to obtain the stall speed at the standard deceleration, an appropriate number of test points has to be executed, with different decelerations, according to the experience and perception of the test pilot. Wind effect must be minimized, so a wind triangle before each stall test should be performed and the stall test repeated upwind and downwind. The detailed procedure is the following:

1. Trim the aircraft approximately at $1.4V_{S1}$, where V_{S1} is the estimated stall speed at the configuration which is tested;
2. Set the engine in idle and pull the stick until a stall is produced, recognised by a sudden pitch or roll brake or by the elevator maximum deflection;
3. Regain the normal attitude and trim for the following test point;
4. Repeat the procedure with different decelerations.

Three different decelerations has been performed upwind and other three downwind, repeated in two flights for each configuration, namely:

- Flights 02.1706 and 03.1706 for CR configuration;
- Flights 03.1106 and 04.1106 for TO configuration;
- Flights 01.1106 and 02.1106 for LND configuration.

During the post-processing phase, the first issue is to identify the stall nature, whether aerodynamic or for maximum elevator deflection. This is accomplished by checking the existence of a pitch or roll break during the test before the elevator reaches its mechanical limit. If the elevator does not reach the limit and there is no evidence of a break, the test point is not valid and

should not be considered in the post-processing. Once all the stalls have been classified, stall speed for each test point should be found, as prescribed in CS-23 FTG ([1]):

- For aerodynamic stalls, V_{S1} is the speed at which pitch or roll brake occurs and the deceleration is the one from V_{S1} to $1.1V_{S1}$;
- For elevator stop stalls, V_{S1} is the minimum speed reached with the stick held in aft position and deceleration is the one from V_{S1} to $1.1V_{S1}$;

Stall speed is the calibrated speed reduced with respect to the standard weight of 472.5 kg:

$$V_{S_W} = V_S \sqrt{\frac{W_S}{W_T}} \tag{5.1}$$

Stall speed at the standard deceleration is found with a linear regression among all the deceleration-reduced stall speed points by finding the speed correspondent to 2 km/h/s.

5.2.4 Test results

All the LND configuration stalls have been reached with aerodynamic break, while all the TO stalls have experienced an elevator stop without any break. CR configuration stalls have had a different nature with respect to the other configurations: they reached the minimum speed before any aerodynamic brake or elevator stop, started a dive and then either the elevator stopped or a slight brake was manifested.

Fig. 5.1 shows aircraft behaviour during a stall in LND configuration. It is possible to verify how the elevator reaches its mechanical limit after the clear roll break on the right; during the break the pilot held the bar in the aft position for one second before starting the recovery procedure, pitching the nose down, how it is confirmed by the pitch angle, rudder and aileron deflection time history.

The aircraft reaction to a stall in TO configuration is very different, as it is explicated in Fig. 5.2: neither roll nor pitch brake appears, while the elevator reaches the stop and it is held in that position for two seconds, before the pilot starts the recovery phase by reversing the elevator to pitch the nose down.

Fig. 5.3 shows a typical stall in CR configuration, which is not the common one expected, according to CS23: the pilot starts pulling the stick and reduces the speed, which reaches a minimum value before any stall manifestation happens. A slight roll brake is present, promptly corrected with a

small aileron effort; stall behaviour in CR configuration is such plain that no important lateral-directional control is needed. After the aircraft reaches the minimum speed of the test, it starts a dive, which makes the speed increase before the elevator reaches its mechanical limit or some roll brake happens. Since CS23 FTG ([1]) does not contemplate such a case, during the post-processing phase stall speed has been considered as the minimum speed of the test. This is in accordance with the procedure prescribed for elevator limited stalls, whose stall speed is indeed the minimum reached during the test.

Fig. 5.4 shows the linear regression between all the test points to find out the stall speed at the standard deceleration of 2 km/h/s. For the CR configuration stall, since the two flights were performed with significantly different weights, which had most likely influenced the dynamics of the stall deceleration, only test of 02.1706 has been considered, the one with the most advanced center of gravity.

The overall results for weight-standardized calibrated and indicated stall speed are summarized in Tab. 5.1.

Table 5.1: Stall CAS in LND, TO and CR configuration.

Conf.	CAS_{stall} [km/h]
LND	77.3
TO	78.4
CR	85.4

5.2.5 Conclusions

As expected, stall speed is way higher than the one of the first G70, which stalled at 71.0, 68.4, 64.8 km/h in CR, TO and LND configuration, respectively. The only modification which can be undoubtedly related to the stalling speed increase is the almost total absence of vortex generators. The compliance with LTF-UL, which is applied to aircraft with stalling speed of maximum 65 km/h, is not respected. CS-VLA ([2]) has a higher stalling speed limit of 83 km/h, probably due to the greater maximum allowed weight of 750 kg (LTF-UL has 472.5 kg of limit), but, if the manufacturer aims at certifying the aircraft according to the German regulation, he should consider a way to decrease the stalling speed. Two possible alternatives are either installing vortex generators along the full wing span, or closing the gap between wing and flap when the latter is deflected, in order to maintain the air stream attached to the wing as much as possible.

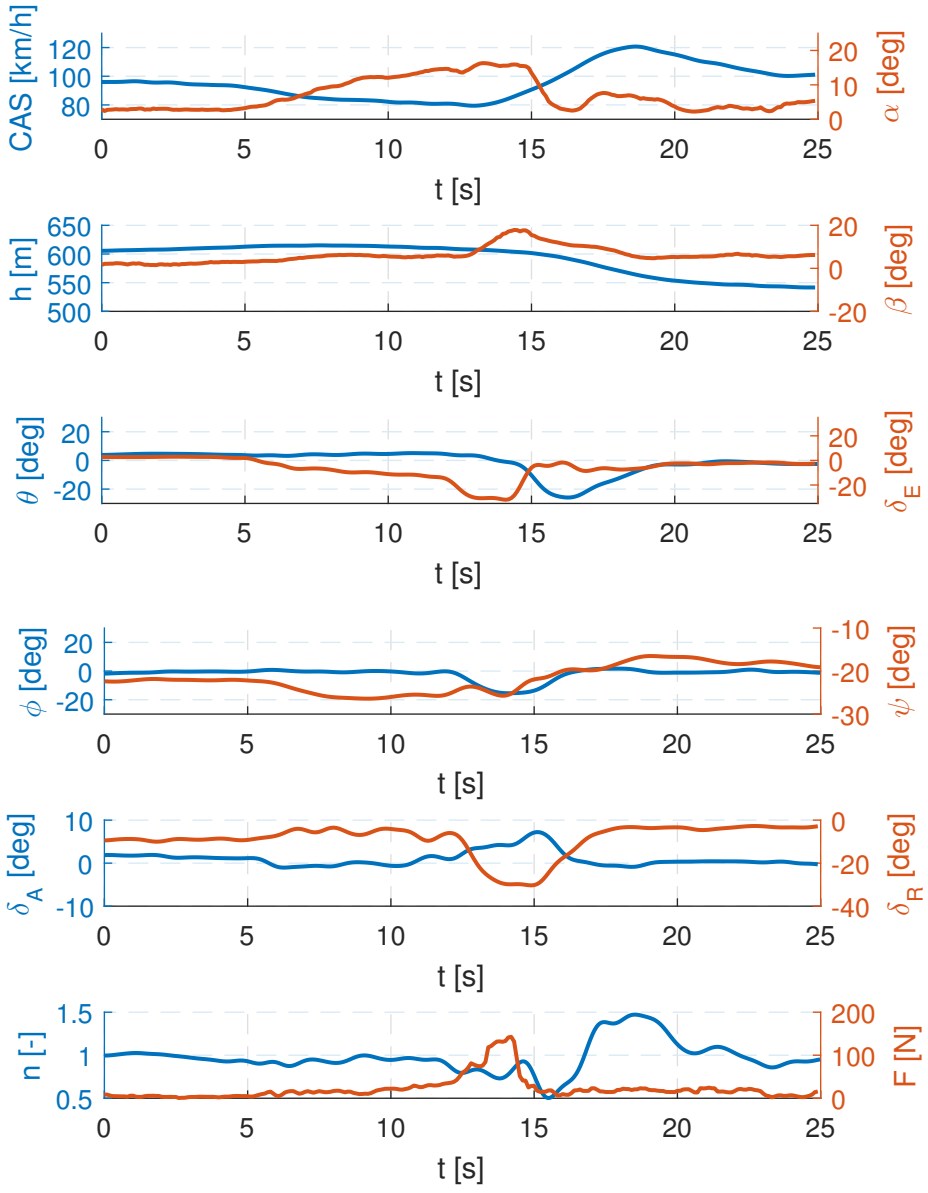

Figure 5.1: Stall in LND configuration, showing a clear roll break.

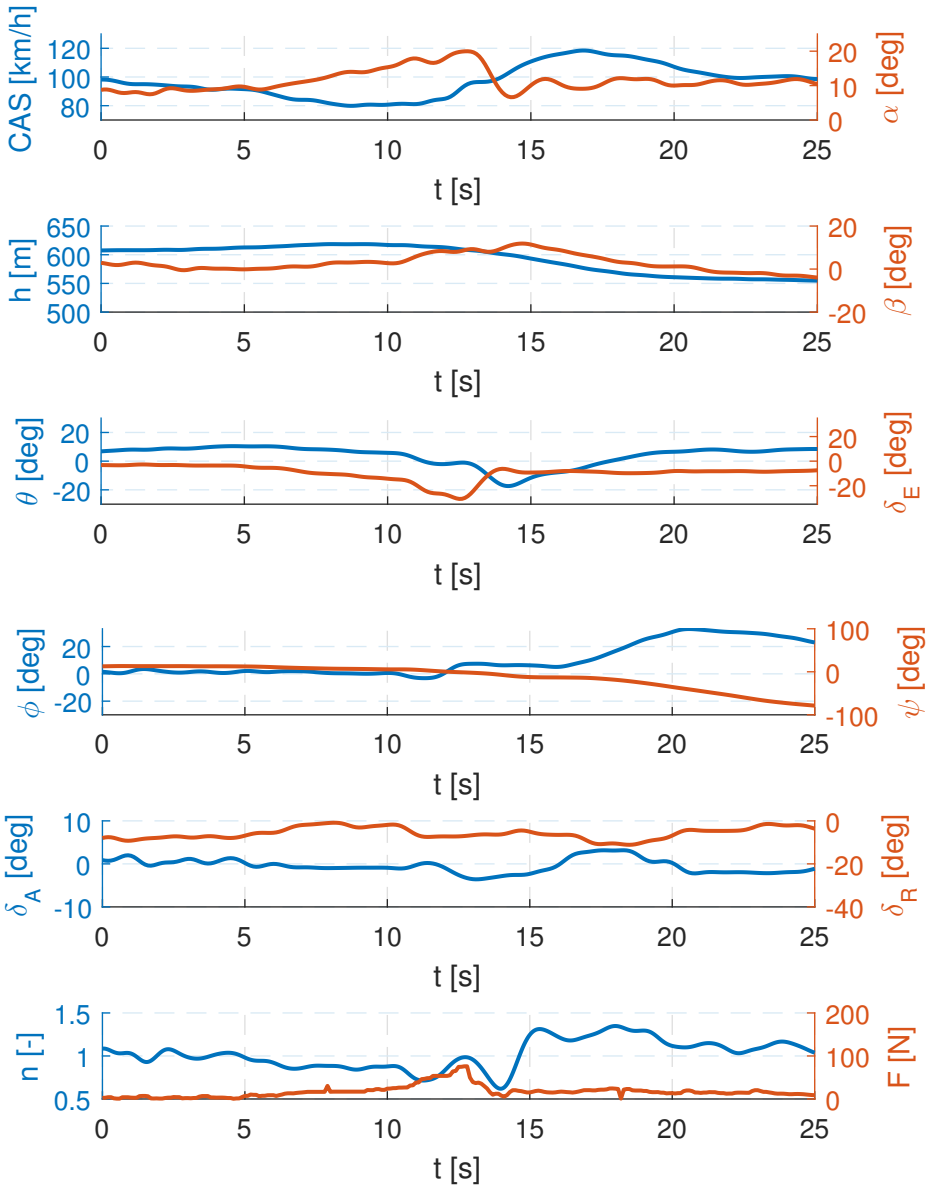

Figure 5.2: Stall in TO configuration, showing maximum elevator deflection at stall.

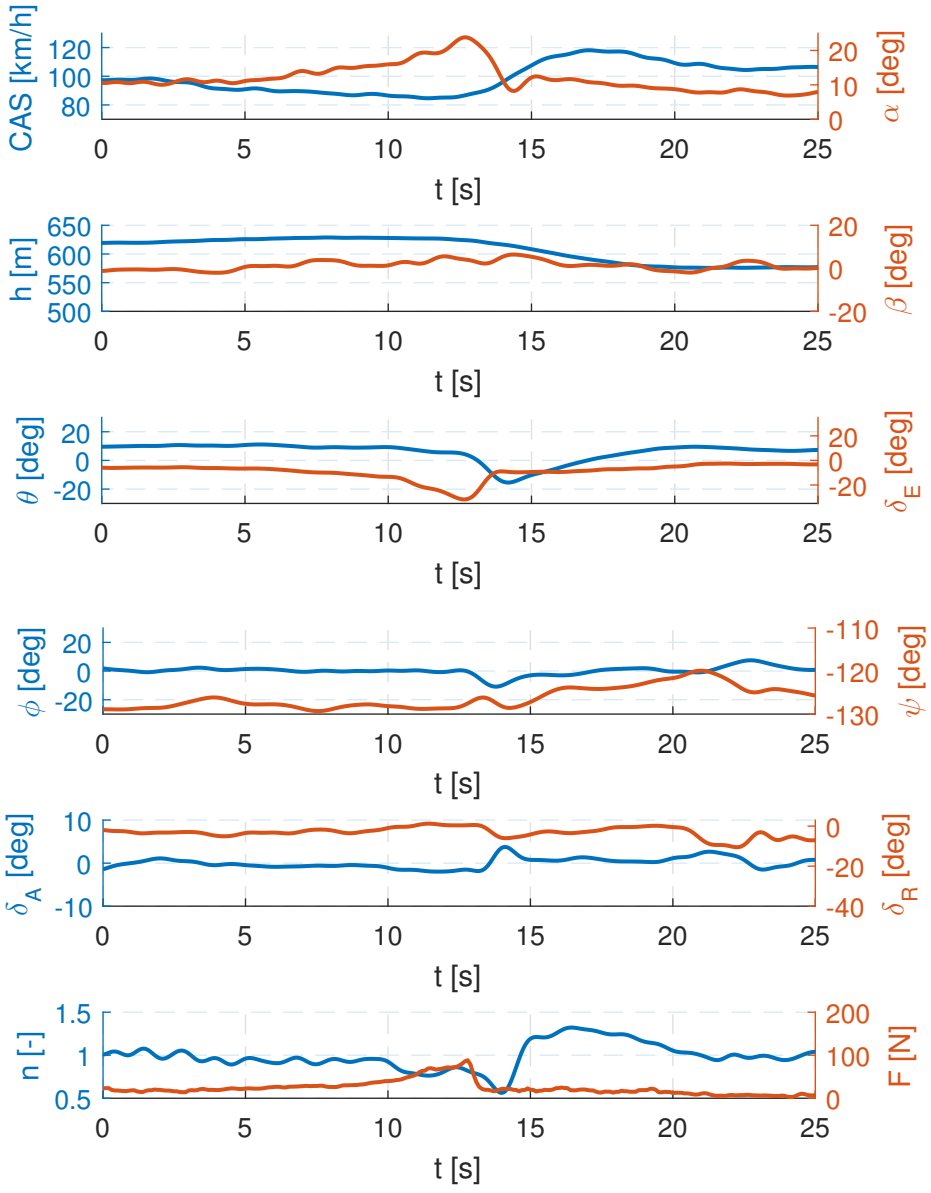

Figure 5.3: Stall in CR configuration.

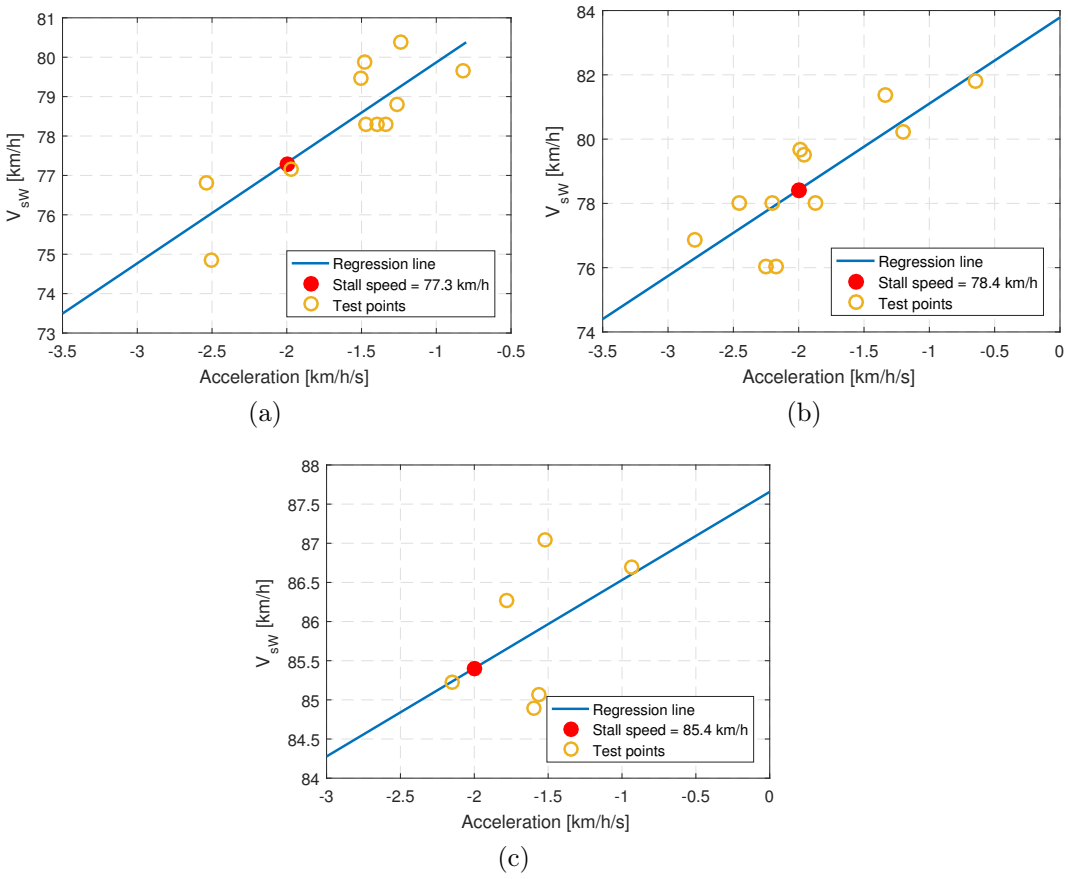

Figure 5.4: Linear regressions of the test points in LND (5.4a), TO (5.4b) and CR (5.4c) configuration.

5.3 Stall behaviour

5.3.1 Introduction

Since the importance of stall behaviour, which means the qualitative and quantitative study of the reaction of the aircraft before, after and during the stall, a separate section has been dedicated to it. LTF-UL ([5]), as long as CS23 ([1]) and CS-VLA ([2]), dedicates to stall behaviour the sections 201 and 203. According to them, all the possible stall behaviour have to be explored, from idle throttle to MCP, both in level flight and during a turn. Throughout the campaign, for logistic constraints, only idle level stalls have been tested.

5.3.2 Test objectives

Test objective is to assess the controllability of the aircraft and its aptitude to regain level flight without jeopardizing the safety of the operations. Moreover, LTF-UL 201 has precise quantitative requests about aircraft behaviour:

- During the recovery, *it must be possible to prevent more than 20° of bank, by the normal use of controls*;
- *The loss of altitude from the beginning of stall until regaining level flight [...] and the maximum pitch attitude below the horizon must be determined.*

Moreover, LTF-UL 207 prescribes an adequate stall warning, either through the inherent aerodynamic qualities of the aeroplane (buffeting) or by a device that clearly indicates the stall.

5.3.3 Test execution

The flights aimed at stall performance testing have been the same ones of stall speed determination, as reported in 5.2.3.

5.3.4 Test results

The only configuration which the aircraft experienced a roll brake with has been the LND one. Time history shows how the maximum of 20° of bank can be easily avoided, as shown in Fig. 5.5. Tabb. 5.2, 5.3, 5.4 report maximum pitch angle below the horizon and the total loss of altitude. Not all the stall tests have been considered, in particular:

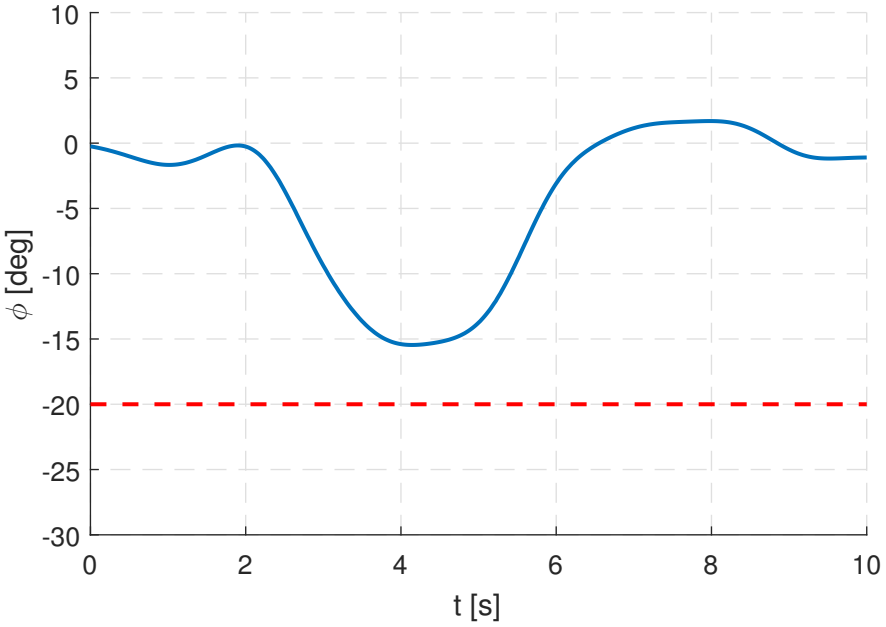

Figure 5.5: Roll angle during the first stall of flight 01.1106, LND configuration.

- only the stalls already analysed for stall speed determination have been reported, since, how already stated, some test points shown an unusual behaviour which suggested a non-conventional test technique and consequently the impossibility to establish a comparison;

- last stall test points of some flights have a very high loss of altitude compared to other test points with the same configuration. The reason is to be found in the fact that after these last test points the pilot took advantage of the altitude drop to reach a lower flight level. These test points, although employed for stall speed calculation, do not appear in this section.

Pitch variations during stall never exceed 30 deg and they are all due to the recovery manoeuvre. Altitude drop from the stall to the end of the recovery seldom overreaches 70 m (230 ft): this does not represent a danger in any of the flight phases except in the terminal ones, where a certain level of risk has to be accounted for all the airplanes. Fig. 5.6 clearly show how there is no correlation between any of these parameters, namely deceleration during the stall test does not influence the pitch brake as much as does not affect altitude drop; besides, pitch brake and altitude drop have no correlation, too.

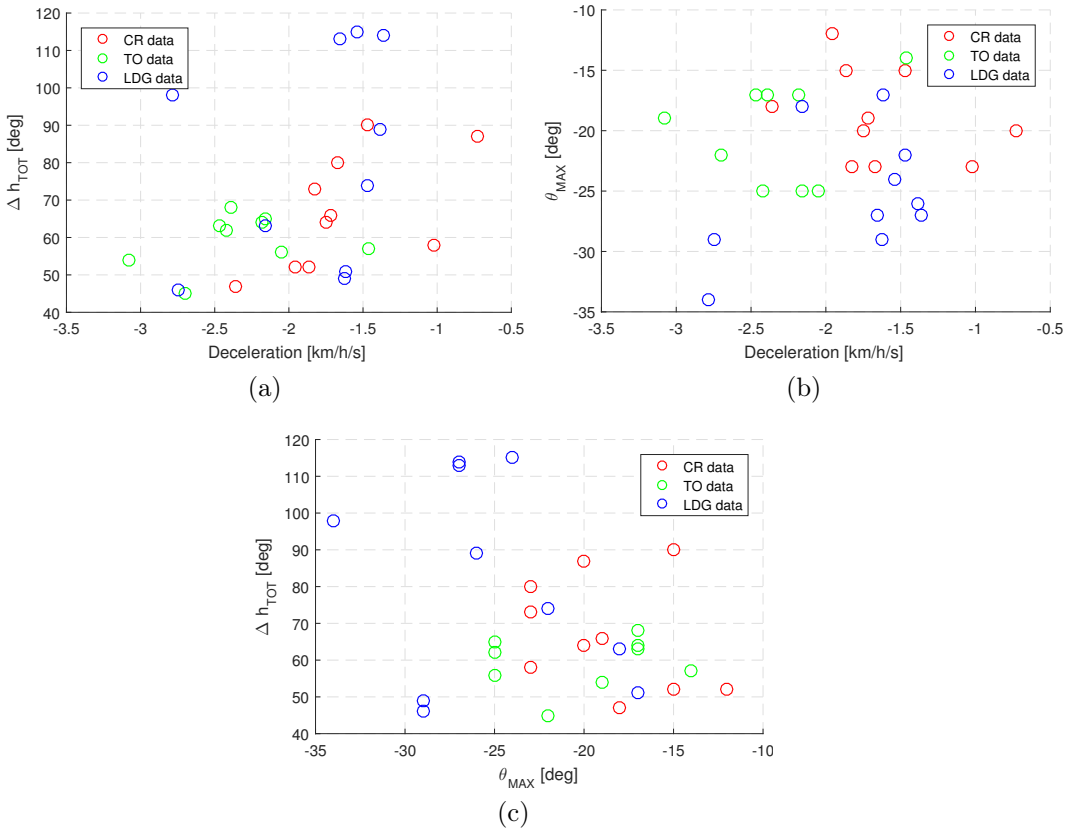

Figure 5.6: Scatter plot of the various parameters analyzed in this section: deceleration versus pitch brake and altitude drop (5.6a and 5.6b) and pitch brake versus altitude drop (5.6c).

Table 5.2: Maximum pitch angle below horizon and total loss of altitude for stalls in CR configuration, flights 02.1706 and 03.1706.

Flight Nr.	Conf.	θ_{MAX} [deg]	Δh_{TOT} [m]
02.1706	CR	-23	58
		-12	52
		-20	64
		-18	47
		-19	66
		-23	80
03.1706	CR	-15	52
		-23	73
		-20	87
		-15	90

Table 5.3: Maximum pitch angle below horizon and total loss of altitude for stalls in TO configuration, flights 03.1106 and 04.1106.

Flight Nr.	Conf.	θ_{MAX} [deg]	Δh_{TOT} [m]
03.1106	TO	-19	54
		-14	57
		-17	68
		-17	63
		-22	45
04.1106	TO	-25	62
		-17	64
		-25	65
		-25	56

5.3.5 Conclusions

Stall speed behaviour is satisfying: it is always possible to regain the level flight without any danger for the safety of the operations and it is proved how the aircraft is able to maintain aerodynamic brakes and altitude drop within acceptable limits. It is worthy to underline how the aim of the test was to determine the stalling speed; consequently, all the stalls were executed with the engine in idle how prescribed by the normative. The following certification campaign will definitely focus also on turning and MCP stalls, how stated in LTF-UL 203.

Table 5.4: Maximum pitch angle below horizon and total loss of altitude for stalls in LND configuration, flights 01.1106 and 02.1106.

Flight Nr.	Conf.	θ_{MAX} [deg]	Δh_{TOT} [m]
01.1106	LND	-26	89
		-27	113
		-34	98
		-27	114
		-24	115
02.1106	LND	-18	63
		-17	51
		-29	46
		-29	49
		-22	74

5.4 Take-off and landing distance

5.4.1 Introduction

Take-off and landing distance is a major performance indicator influencing the safety of the flight for a UL aircraft; for instance, it is not seldom that there is the need to take-off or land in very short runways, sometimes even in airfield without a proper runway. The past campaign on the first G70 showed how the aircraft was able to take-off and land in 276 and 328 m, respectively. The expected result for this test is not far from the old one and probably even better due to the aerodynamic improvements of the fuselage and the vortex generators removal.

5.4.2 Test objectives

LTF-UL 51 ([5]) states that *the distance required to take-off under maximum weight condition from a dry, level, short-mown grass strip and climb over a 15 metres obstacle must be determined and must not exceed 300 metres.* There is no mention about landing distance, which, however, has been calculated in order to fill in the flight manual with an accurate value. The final take-off distance must be the average between six demonstration flights; the same standard has been used for landing distance.

5.4.3 Test execution

All the take-off were full-power ones, which are subjected to the following procedure:

1. Hold the brakes and give full throttle;
2. Release the brakes;
3. Rotation at an indicated airspeed of $V_R = 70$ km/h;
4. Lift-off and climb to 15 m (50 ft).

Landing procedure follows an analogous method, namely:

- Maintain a stable approach, with power as necessary;
- Descend through 15 m (50 ft);
- Touch-down at an indicated airspeed of $V_{TD} = 80$ km/h;

- Brake until full stop.

The first issue about take off and landing distance is to make all the tests comparable: it means that the flight technique should be the same between all the considered tests, not only in general terms of full power take-off or full stop landing, but also in terms of lift-off and touch-down airspeed. This task has been accomplished by analysing a certain number of take-off and landings, finding out lift-off and touch-down airspeed (CAS) and verifying they are almost the same after a reduction with respect to the weight, according to the formulas:

$$V_{LO_W} = V_{LO}\sqrt{\frac{W_S}{W_T}} \tag{5.2a}$$

$$V_{TD_W} = V_{TD}\sqrt{\frac{W_S}{W_T}} \tag{5.2b}$$

Once six similar take-off and landings are found, the empirical reduction formulas suggested by Kimberlin in [15] have to be applied.

Take-off reduction formulas

Firstly, observed ground distance S_{g0} (from brake release to lift-off) and observed air distance S_{a0} (from lift-off to 15 m height) have to be determined. Once the two raw distances are available, they must be corrected for wind speed, as follows:

$$S_{gT_{TO}} = S_{g0_{TO}}\left(1 + \frac{V_{W_{TO}}}{V_{GS_{LO}}}\right)^{1.85} \tag{5.3a}$$

$$S_{aT_{TO}} = S_{a0_{TO}} + V_{W_{TO}} t_{TO} \tag{5.3b}$$

Distances reduced for wind speed must be corrected for weight, with respect to the standard weight of 472.5 kg, and for air density, with respect to standard air density:

$$S_{gS_{TO}} = S_{gT_{TO}}\left(\frac{W_S}{W_T}\right)^{2.6}\left(\frac{\sigma_T}{\sigma_S}\right)^{1.9} \tag{5.4a}$$

$$S_{aS_{TO}} = S_{aT_{TO}}\left(\frac{W_S}{W_T}\right)^{2.6}\left(\frac{\sigma_T}{\sigma_S}\right)^{1.9} \tag{5.4b}$$

Once the standard ground and air distances are found, the standard distance over a 15 m (50 ft) obstacle is their sum:

$$S_{50_{TO}} = S_{gS_{TO}} + S_{aS_{TO}} \tag{5.5}$$

Landing reduction formulas

The formulas are similar to the take-off ones. Firstly, observed air distance S_{a0} (from 15 m to touch-down) and observed ground distance S_{g0} (from touch-down to full stop) have to be reduced with respect to wind speed at the time of the test:

$$S_{gT_{LD}} = S_{g0_{LD}} \left(1 + \frac{V_{W_{LD}}}{V_{GS_{TD}}}\right)^{1.85} \tag{5.6a}$$

$$S_{aT_{LD}} = S_{a0_{LD}} + V_{W_{LD}} t_{LD} \tag{5.6b}$$

The standardization with respect to weight and density is quite different from the one used for take-off, namely:

$$S_{gS_{LD}} = S_{gT_{LD}} \left(\frac{W_S}{W_T}\right)^2 \left(\frac{\sigma_T}{\sigma_S}\right) \tag{5.7a}$$

$$S_{aS_{LD}} = S_{aT_{LD}} \tag{5.7b}$$

The total landing distance from the 15 m obstacle to full stop is the sum of the standardized air and ground landing distances:

$$S_{50_{LD}} = S_{gS_{LD}} + S_{aS_{LD}} \tag{5.8}$$

5.4.4 Test results

Six flights from 01.1006 to 06.1006 have been considered for take-off and landing analyses. Test results will be detailed separately for sake of clarity.

Take-off analysis

Time history of all the take-off has been analysed in order to find the time of the three remarkable events, that are brake release, lift-off and 15 m obstacle. For the first, EVT marker is reliable; the second and the third are found with GPS height. An example of time history is reported in Fig. 5.7.

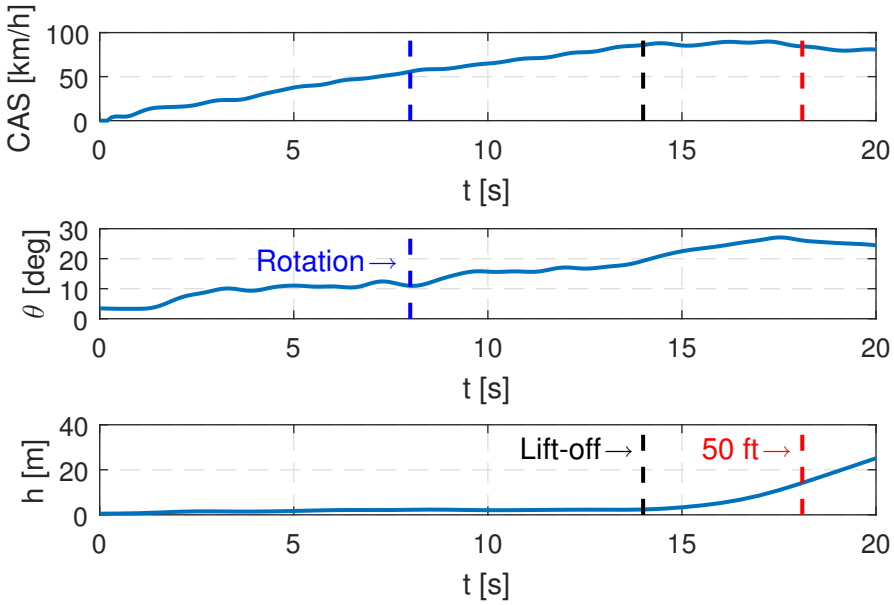

Figure 5.7: CAS, pitch angle and GPS height during take-off of flight 03.1006.

Once all the lift-off CAS have been found, they can be reduced with respect to weight by using the 5.2a. Results for the examined flights are reported in Tab. 5.5: the six take-off are comparable, since the difference between minimum and maximum is only 6 km/h.

Table 5.5: Reduced CAS at lift-off of the six examined flights.

V_{LO} [km/h]	V_{LO_W} [km/h]
85	76
77	71
80	73
84	77
79	73
82	77

Observed ground and air distances are found directly from the GPS, as much as $V_{GS_{LO}}$ (Fig. 5.8). All the data and results are summarized in Tab. 5.6.

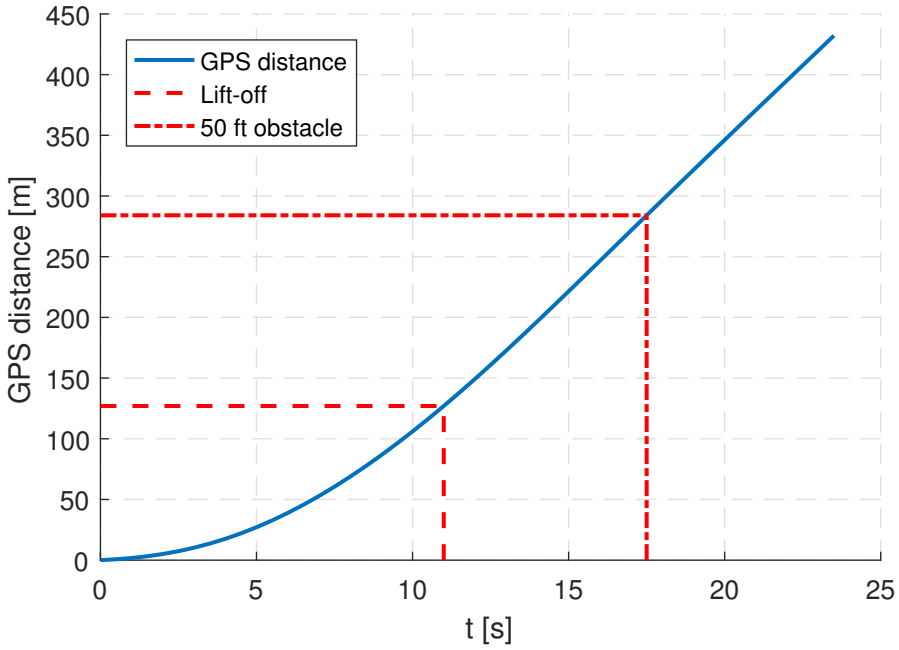

Figure 5.8: GPS distance during take-off of flight 02.1006.

Landing analysis

Time history of all the landings has been analysed in order to find the time of the three remarkable events, that are 15 m obstacle, touch-down and full stop. For the latter, EVT marker is reliable; the second coincides with the time when load factor starts wavering and the first is found with GPS height. An example of time history is reported in Fig. 5.9.

Once all the touch-down CAS have been found, they can be reduced with respect to weight by using the 5.2b. Results for the examined flights are reported in Tab. 5.7: the six landings are comparable, since the delta between minimum and maximum is only 5 km/h.

Observed ground and air distances are found directly from the GPS, as much as $V_{GS_{TD}}$ (Fig. 5.10). All the data and results are summarized in Tab. 5.8.

5.4.5 Conclusions

The improvement in terms of take-off distance with respect to the first G70 is well clear: the new prototype lifts off in 80 m less. The reason if this surprising behaviour has to be found in the general aerodynamic improvement of the aircraft, which is further confirmed, and in the new propeller with an

Table 5.6: Take-off distance data and results.

Flight Nr.	$S_{g0_{TO}}$ [m]	$S_{a0_{TO}}$ [m]	$V_{W_{TO}}$ [km/h]	$V_{GS_{LO}}$ [km/h]	t_{TO} [s]	$S_{50_{TO}}$ [m]
01.1006	206	155	-3.7	95	25	**189**
02.1006	150	134	-2.6	75	27	**167**
03.1006	216	109	-1.9	90	30	**179**
04.1006	124	152	2.1	85	33	**171**
05.1006	200	144	-1.9	90	30	**199**
06.1006	175	158	2.3	90	30	**214**
					Avg.	**187 m**

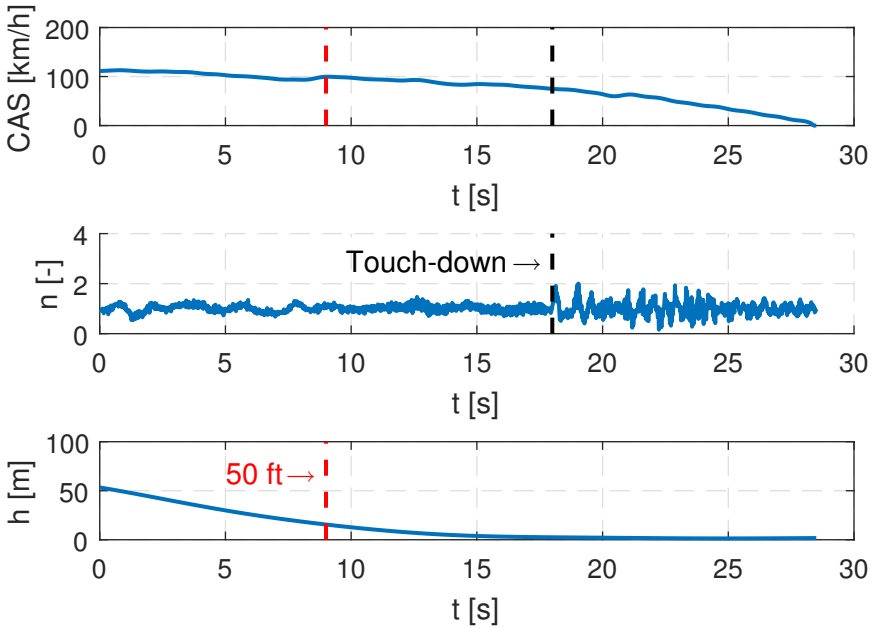

Figure 5.9: CAS, load factor and GPS height during landing of flight 02.1006.

increased pitch, which makes the airplane faster. Moreover, part of the improvement should be attributed to the vortex generator removal, which have undeniable advantages for stall speed, but they increase the overall drag of the aircraft.

Landing distance is lower of the former aircraft's one, but the difference is not as pronounced as the take off one and the main differences are in the air distance, which might be due to the different execution of the approach.

Table 5.7: Reduced CAS at touch-down of the six examined flights.

V_{TD} [km/h]	V_{TD_W} [km/h]
75	69
75	70
79	73
78	73
79	74
79	74

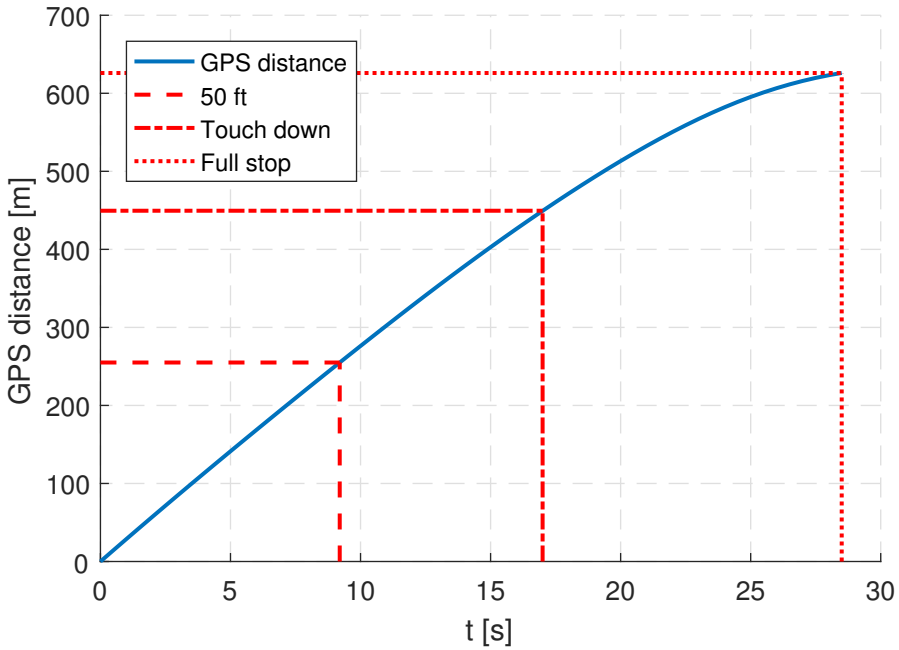

Figure 5.10: GPS distance during landing of flight 02.1006.

Table 5.8: Landing distance data and results.

Flight Nr.	$S_{g0_{LD}}$ [m]	$S_{a0_{LD}}$ [m]	$V_{W_{LD}}$ [km/h]	$V_{GS_{TD}}$ [km/h]	t_{LD} [s]	$S_{50_{LD}}$ [m]
01.1006	110	292	3.2	80	12	**294**
02.1006	176	195	0.7	80	8	**281**
03.1006	187	171	-1.9	82	7	**245**
04.1006	133	297	2.1	85	12	**337**
05.1006	181	235	-1.9	90	9	**298**
06.1006	121	187	2.3	82	8	**258**
					Avg.	**286 m**

5.5 Climb performance

5.5.1 Introduction

Climb performance test is not trivial for a UL aircraft: altitude limitations make the airplane face some obstacles which have to be properly avoided. The expectation for this test is good, since the former version had already demonstrated a full compliance to LTF-UL and, more in general, a satisfying maximum climbing speed of 5 m/s, approximately. Due to the aerodynamic improvement of the new aircraft, it is expected to behave at least in the same way of the former. Climbing test has been performed for all the aircraft configurations and the main differences between them will be detailed in the Appendix. The test has been performed both in TO and in CR configuration, which are the most critical conditions to be tested for climbing test: LND configuration is used in the very terminal phase of the flight where there is no necessity of climbing; even if a go-around were necessary, the flaps would be instantly armed in the TO position to climb.

5.5.2 Test objectives

LTF-UL 65 states that *the best rate of climb must be at least 1.5 m/s, not exceeding any temperature limit, after correcting for Standard Atmosphere at Sea Level*, with:

- not more than take-off power;
- landing gear retracted (if possible);
- maximum weight;
- wing flaps in the climb position.

Moreover, the test provides speed of fastest and steepest climb for the aircraft.

5.5.3 Test execution

The technique to determine the aircraft ROC is the sawtooth climb, consisting in a series of climb segments, flown through the same altitude gap with full throttle. Every climb has a different speed, in order to sweep a sufficiently broad range of velocities to provide a good 2nd order approximation. One maximum speed trim shot (with null rate of climb) is needed at the end of the test, at the same target altitude, to provide the closing point of the

approximation. The theory which sawtooth climbs test is based on can be found in Appendix B. Test procedure traces the steps of CS23-FTG ([1]), namely:

1. set the flap in the desired configuration;
2. trim the aircraft sufficiently below the entry altitude;
3. full throttle;
4. start climbing and time the climb, careful to maintain the same airspeed throughout the whole climb;
5. when reached the upper altitude, set power as necessary and descend in order to repeat the climb along the same altitude range with a different airspeed.

Raw Rate of Climb is the ratio between the altitude gap and the time to climb and a normalization is needed. LTF-UL prescribes a correction for Atmosphere Sea Level and does not specify any other correction. In order to provide a better reliability of the corrected results, procedure of Ref. [12] is accomplished.

Data reduction

The following steps are implemented for a correct data reduction:

1. Calculate the raw ROC from the pressure altitude slope:

$$\left(\frac{\Delta h}{\Delta t}\right)_m \tag{5.9}$$

2. Normalize with respect to the standard temperature, by multiplying the test temperature Θ_T versus the standard temperature at the height of the test Θ_S:

$$\left(\frac{\Delta h}{\Delta t}\right)_t = \left(\frac{\Theta_T}{\Theta_{std}}\right)\left(\frac{\Delta h}{\Delta t}\right)_m \tag{5.10}$$

3. Correct for the actual power P_b, temperature deviation, test weight W_T and propeller efficiency, as described in 5.1:

$$\Delta\left(\frac{\Delta h}{\Delta t}\right)_P = \frac{\eta_p P_b}{W_T}\left(1 - \sqrt{\frac{\Theta_S}{\Theta_T}}\right) \tag{5.11}$$

4. Correct for TAS variation with altitude:

$$\Delta\left(\frac{\Delta h}{\Delta t}\right)_{AF} = \frac{V}{g}\left(\frac{dTAS}{dh}\right)\left(\frac{\Delta h}{\Delta t}\right)_{t} \tag{5.12}$$

5. Correct all the previous contributions with respect to standard weight W_S:

$$\left(\sum \frac{\Delta h}{\Delta t}\right)\frac{W_T}{W_S} \tag{5.13}$$

6. Correct for induced drag due to a non-standard weight:

$$\Delta\left(\frac{\Delta h}{\Delta t}\right)_{ind} = \frac{2}{\pi\lambda e\sigma\rho_0 V_{\mathrm{TAS}} S}\left[\frac{W_T^2 - W_S^2}{W_S}\right] \tag{5.14}$$

The final equation is:

$$\left(\frac{\Delta h}{\Delta t}\right)_{std} = \left[\left(\frac{\Delta h}{\Delta t}\right)_{t} + \Delta\left(\frac{\Delta h}{\Delta t}\right)_{P} + \Delta\left(\frac{\Delta h}{\Delta t}\right)_{AF}\right]\frac{W_T}{W_S} + \Delta\left(\frac{\Delta h}{\Delta t}\right)_{ind} \tag{5.15}$$

5.5.4 Test results

Climb tests have been executed with the aircraft in all the configurations; this section shows the only results with the third and last aircraft configuration. The reader is asked to refer to Appendix B for the results with the aircraft in all the configurations. Sawtooth climbs were properly executed during the following flights:

- Flight 05.1006, CR configuration, 1600 ft;
- Flight 01.1507, CR configuration, 1200 and 2100 ft;
- Flight 03.1006, TO configuration, 1600 ft;
- Flight 05.1106, TO configuration, 1300 ft.

In this section are analysed flight 05.1006 and 03.1006. Further analyses of the other climbs are in Appendix B. Tab. 5.9 and Tab. 5.11 gather the test data for flight 05.1006 and 03.1006, respectively. Tab. 5.10 and Tab. 5.12 summarize corrections applied to each test point of the climbs.

The final results for the two flights, meant as the Rate of Climb 2nd order least-squares approximation curves, are reported in Fig. 5.11 and Fig. 5.12 and summarized in Tab. 5.13. Compliance with LTF-UL is demonstrated with a broad margin.

Table 5.9: Climb data in aircraft configuration 3, CR, flight 01.1507.

Climb	1	2	3	4	5
IAS [km/h]	95	100	110	120	192
CAS [km/h]	98	102	110	118	175
TAS [km/h]	99	103	111	120	178
ROC [m/s]	3.09	3.43	3.39	3.53	0

Table 5.10: Corrections for every climb during flight 01.1507.

Climb	1	2	3	4	5
$\left(\frac{\Delta h}{\Delta t}\right)_t \frac{W_T}{W_S}$ $[m/s]$	3.91	4.35	4.28	4.47	0
$\Delta\left(\frac{\Delta h}{\Delta t}\right)_P \frac{W_T}{W_S}$ $[m/s]$	0.10	0.10	0.10	0.12	0.13
$\Delta\left(\frac{\Delta h}{\Delta t}\right)_{AF} \frac{W_T}{W_S}$ $[m/s]$	0.19	0.23	0.27	0.32	0
$\Delta\left(\frac{\Delta h}{\Delta t}\right)_{ind}$ $[m/s]$	0.20	0.19	0.18	0.16	0.11
$\left(\frac{\Delta h}{\Delta t}\right)_{std}$ $[m/s]$	4.40	4.87	4.83	5.07	0.24

Table 5.11: Climb data in aircraft configuration 3, TO, flight 03.1006.

Climb	1	2	3	4	5	6
IAS [km/h]	85	90	95	100	105	125
CAS [km/h]	90	94	98	102	106	122
TAS [km/h]	92	96	100	104	108	124
ROC [m/s]	3.10	2.85	3.05	3.69	3.48	3.17

5.5.5 Conclusions

Last aircraft configuration shows a maximum rate of climb which is 1 m/s lower than the one of aircraft configurations 1 and 2, whose results are detailed in Appendix B. The reason is with no doubt linked to the propeller pitch modification, which has been increased: more pitch benefits efficiency at high speeds and disadvantages traction in the medium-low range of speeds, which is the one of the test. There is no particular difference between climb performance in CR and TO configuration in terms of best rate of climb,

Table 5.12: Corrections for every climb during flight 03.1006.

Climb	1	2	3	4	5	6
$\left(\frac{\Delta h}{\Delta t}\right)_t \frac{W_T}{W_S}$ $[m/s]$	3.20	2.93	3.14	3.81	3.59	3.27
$\Delta\left(\frac{\Delta h}{\Delta t}\right)_P \frac{W_T}{W_S}$ $[m/s]$	0.08	0.09	0.09	0.09	0.09	0.10
$\Delta\left(\frac{\Delta h}{\Delta t}\right)_{AF} \frac{W_T}{W_S}$ $[m/s]$	0.16	0.16	0.18	0.24	0.25	0.30
$\Delta\left(\frac{\Delta h}{\Delta t}\right)_{ind}$ $[m/s]$	0.18	0.17	0.17	0.16	0.15	0.13
$\left(\frac{\Delta h}{\Delta t}\right)_{std}$ $[m/s]$	4.23	3.92	4.19	5.03	4.78	4.42

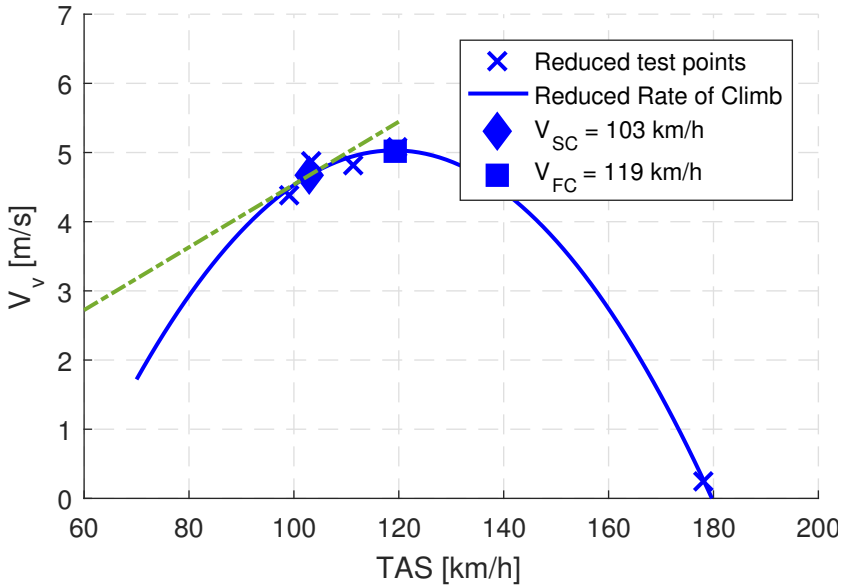

Figure 5.11: Rate of Climb during flight 01.1507, CR configuration, 1200 ft.

Table 5.13: V speeds after flight 01.1507 and 03.1006 climbs analysis.

Aircraft conf.	Flap conf.	V_{SC} [km/h]	V_{FC} [km/h]	$maxROC$ [m/s]
03	CR	102	119	5.03
03	TO	101	112	4.78

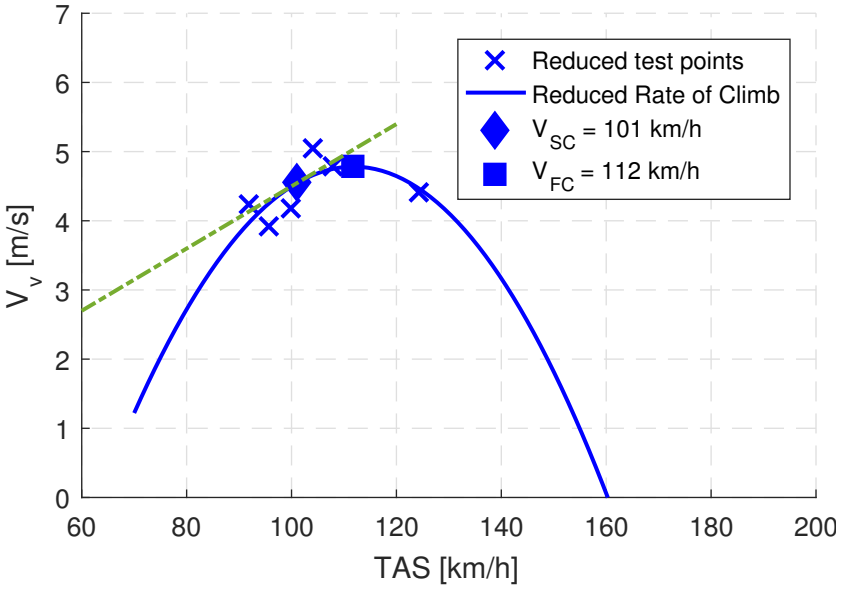

Figure 5.12: Rate of Climb during flight 03.1006, TO configuration, 1600 ft.

except for the fastest climb speed V_{FC}, which, as expected, is lower in TO configuration.

Compliance with LTF-UL has been widely demonstrated. ROC value is similar to the one of the former G70, which climbed at a maximum speed of 4.7 m/s.

Steepest and fastest climb velocities, obtained during all the test flights devoted to climb performance, show a good resemblance between themselves, as demonstrated in Appendix B.

Chapter 6

Controllability and manoeuvrability test

This chapter focuses on the main characteristics which contribute to make the aircraft easy and intuitive for the pilot. Firstly, the attitude of the aircraft to be manoeuvred around the longitudinal axis has been tested with excellent results, with a time to roll well below the limit imposed by the normative. Secondly, some wind-up turns have been performed, in order to verify the stick force feedback to the pilot during a manoeuvre. The feedback is correct, since more force is required to increase load factor, but the gradient is low and it is quite easy to reach high values of load factor with a medium effort on the stick. Eventually, trimmability test demonstrated how the airplane can be perfectly levelled with any centre of gravity configuration without excessive effort of the pilot.

6.1 Lateral and directional control

6.1.1 Introduction

Lateral and directional control test (or *bank-to-bank*) has been performed during flight 02.2005 in order to assure the perfect manoeuvrability of the aircraft even with the new connections between stick and ailerons, made of cables and pulleys (2.1.2). The results were expected to be satisfying, as much as in the former G70, since the shape and the mass of the aircraft is unchanged around the roll axis.

Theoretically, since the aircraft configuration during the test was the 1st one, the results are not strictly applicable for the final configuration: in fact, dihedral angle has a relevant role in the lateral-directional stability. However,

if the test result is totally satisfying with a good margin, it will be regarded as valid also for the 3rd aircraft configuration, which will require only a fast check to prove the regulation compliance.

6.1.2 Test objectives

The objective of the test is to assess the response of the aircraft around the roll axis with a series of bank-to-bank manoeuvres. LTF-UL 147 requires that *it must be possible, using a favourable combination of controls, to roll the aeroplane from a steady 30 degrees bank turn in one direction to a 30 degrees bank turn in the opposite direction within 5 seconds.*

6.1.3 Test execution

Test has been executed as follows:

1. trim the aircraft at a coordinated turn on one side, right or left, with a bank angle slightly greater than 30°;

2. start a rapid roll manoeuvre to the opposite direction and stop the turn when sure to have reached a 30° bank angle in the other direction;

3. repeat the test the other way round.

Bank angle measure has been taken from the EFIS screen and the time from a manual stopwatch; however, the final result is based only on the post-processing analysis, where bank angle time history has been taken into consideration to obtain bank-to-bank time.

6.1.4 Test results

The test has a fully satisfactory result, with a time from -30° of bank to 30° of 1.8 s and 2.2 s in the opposite direction. There is no signal of non-linearity between roll rate and aileron deflection: the command is always predictable to the pilot, as shown in Fig. 6.1.

6.1.5 Conclusions

As expected, the result is fully satisfying and the command shows a perfect response to the pilot. Nevertheless, dihedral angle reduction has the effect to provide more lateral-directional stability and, consequently, to stiffen the

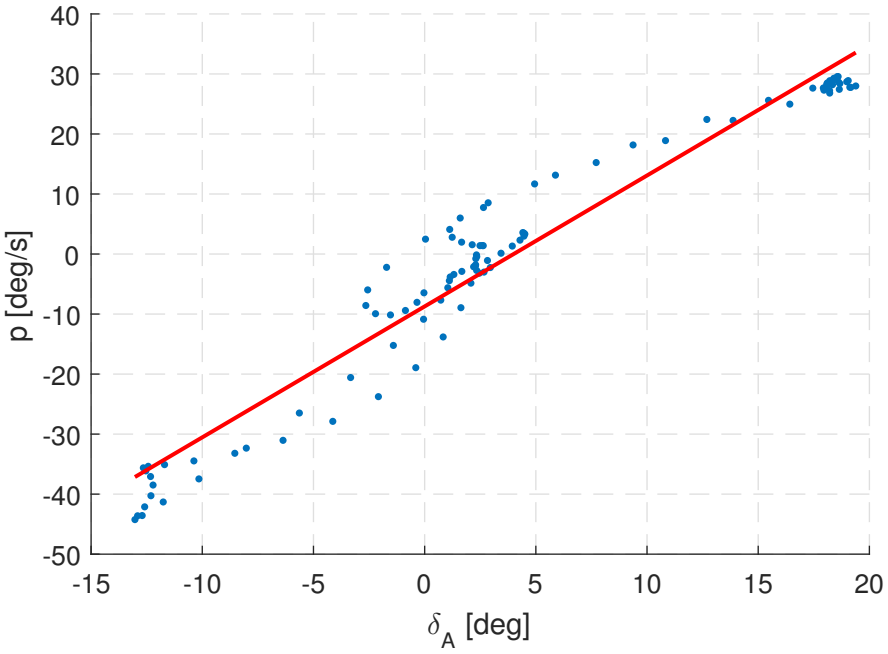

Figure 6.1: Roll rate with respect to aileron deflection during bank-to-bank test

response to the bank-to-bank test; therefore, the aircraft in its final configuration is expected to behave worse. Since the result is totally satisfying with a very good margin, they are not expected important variations in the 3rd and last configuration. A fast check will be required to assess the positive result of the test for type certification.

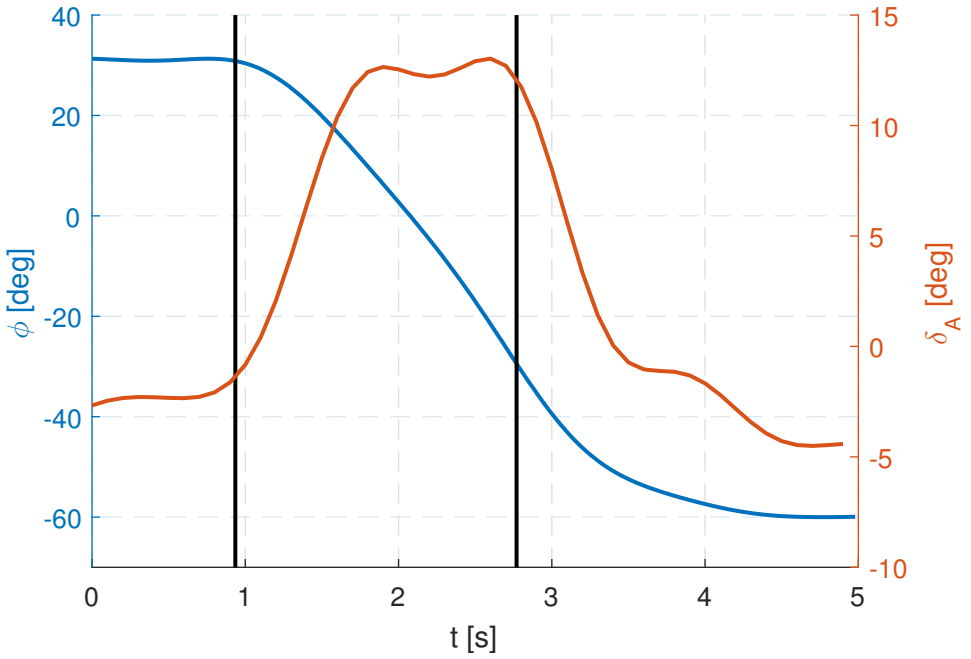

(a)

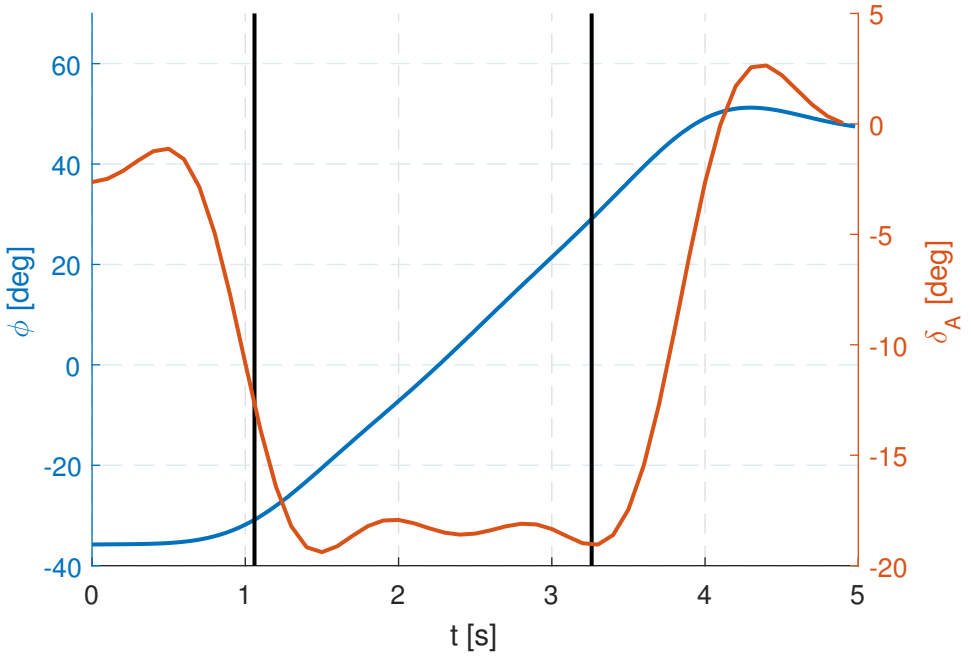

(b)

Figure 6.2: Bank-to-bank test with roll angle and aileron deflection in the right (6.2a) and left (6.2b) direction.

6.2 Elevator control forces in manoeuvres

6.2.1 Introduction

Every time the pilot pushes or pulls the stick, he causes the load factor to increase or decrease; if he does not have a prompt feeling of the rising load factor, the risk to overload the aircraft structure is real. The former G70 showed stable and positive gradient of elevator deflection with respect to load factor, although a quite low gradient was found: it meant that the aircraft was subjected to a great increase of load factor with a moderate effort of the pilot. There is to underline that the flight safety had never been endangered and no overload had been experienced. The current prototype employs the same connections between stick and elevator and the aircraft length is exactly the one of the former G70: test result is not supposed to distance itself a lot from the one of the past campaign.

6.2.2 Test objectives

The aim of this test is to demonstrate that an increase in control force is necessary to raise the load factor. LTF-UL 155 does not prescribe any force limit for the manoeuvre, but only requires a stable gradient during all the turn which gives to the pilot a feedback of the load factor according to the force necessary to accomplish the turn.

6.2.3 Test execution

Compliance is demonstrated with the wind-up turn, namely a continuous turn performed at the same airspeed, increasing bank angle. If the turn remains coordinated for the whole test point, the increase of bank angle makes load factor increase. A descent is allowed to maintain the same airspeed throughout the manoeuvre. During the turn three stabilized points have been marked, in order to fit them with a linear regression and calculate the stick force gradient per g.

Aircraft configuration for this test was the 2nd one during flight 02.0206, but the successive aircraft modifications should not have invalidated the test results: propeller pitch does not definitely influence airplane controllability and dihedral angle variations only influences lateral-directional stability.

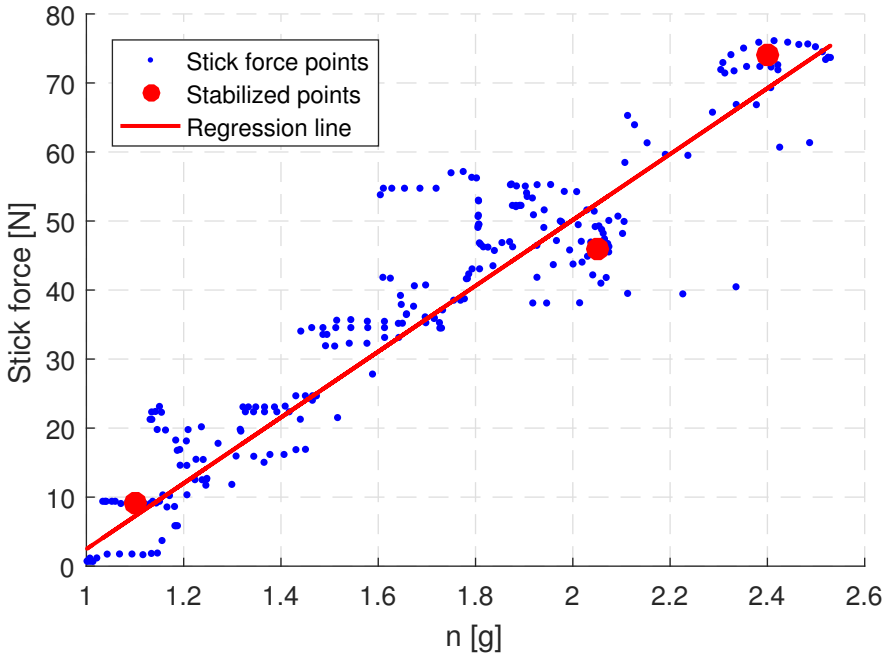

Figure 6.3: Stick force vs Load factor points during wind-up turn.

6.2.4 Test results

Tab. 6.1 summarizes the three stabilized points gathered during the test. Final result is shown in Fig. 6.3: Force versus load factor points are all along a line and the linear regression between the stabilized points has a slope which is similar to the one of the test points cloud. Stick force versus g gradient is:

$$\frac{\Delta F}{\Delta n} = 47.7 \quad \frac{N}{g} \tag{6.1}$$

Table 6.1: Stabilized test points during wind-up turn.

Stick Force [N]	Load Factor [g]
9	1.1
46	2.0
74	2.4

6.2.5 Conclusions

Test result shows a stable and positive slope of the stick force versus load factor curve, but, as expected, the gradient is low: just over 4 kg are required to increase load factor of 1 g, even less than the force observed in the past campaign. The manufacturer should consider to make the command more stiffen. Nevertheless, the maximum load factor reached during all the tests has been of 2.8, far from the upper limit of the manual coming from a static test on the ground, which is $n = 4$.

6.3 Trimmability

6.3.1 Introduction

Trimmability is a simple but important test because the aircraft attitude to be trimmed affects directly flight quality and reduces pilot workload.

During the campaign various trim shots have been executed before other test points in order to check the atmospheric conditions, for instance in order to write down the OAT before sawtooth tests. Nevertheless, the performed trim shots were too short to assess with no doubt the capability of the aircraft to maintain the steady level flight and, moreover, there was the necessity to execute the trim test at various airspeeds with different CG locations for neutral point estimation (9.1). For those reasons, it was decided to devote two separate flights to the trimmability test, with long enough time of level flight and with different CG locations.

6.3.2 Test objectives

LTF-UL 161 requires that *the speed to achieve lateral, longitudinal and directional trim must be between* $1.3V_{S1}$ *and* $2.0V_{S1}$ *at all engine powers and the extreme c.g. positions.*

6.3.3 Test execution

Trimmability test has been executed during the flights aimed at the experimental positioning of the neutral point:

- Flight 03.1706, with $X_G = 32\%$ MAC;
- Flight 04.1706, with $X_G = 25\%$ MAC;
- Flight 05.1706, with $X_G = 35\%$ MAC.

Test technique is straightforward:

1. Level the aircraft at the desired airspeed;
2. Set power and trim tabs deflection as necessary to maintain level flight;
3. When the aircraft is stabilized, leave the stick to confirm the trim condition.

Table 6.2: Speeds of trim test.

Flight	Trim speeds [km/h]
03.1706	90, 120, 130, 160, 170
04.1706	90, 110, 130, 150, 170
05.1706	110, 130, 150, 170

Figure 6.4: Ballasts position to achieve full forward CG, during flight 04.1706.

Trim speeds for each test point are reported in Tab. 6.2.

Different positions of CG have been obtained with ballasts of 12.5 kg each in forward and aft position: three of them have been located beyond the pedals and in the feet-zone of the FTE to advance the CG (Fig.6.4), which has been moved back in the successive flight with two ballasts in the luggage compartment. The full aft CG flight has been executed with a lighter FTE, in order not to exceed the maximum project weight of 600 kg.

6.3.4 Test results

Test results are satisfactory: the only remarkable oscillations of the trim speed are present when a sudden gust is encountered. Trimmability has been reached without any excessive workload for the pilot. Fig. 6.5, 6.6 and 6.7 show CAS behaviour during each flight. It is remarkable how the trim speed is more easily maintained with a forward CG, i.e. a greater static margin.

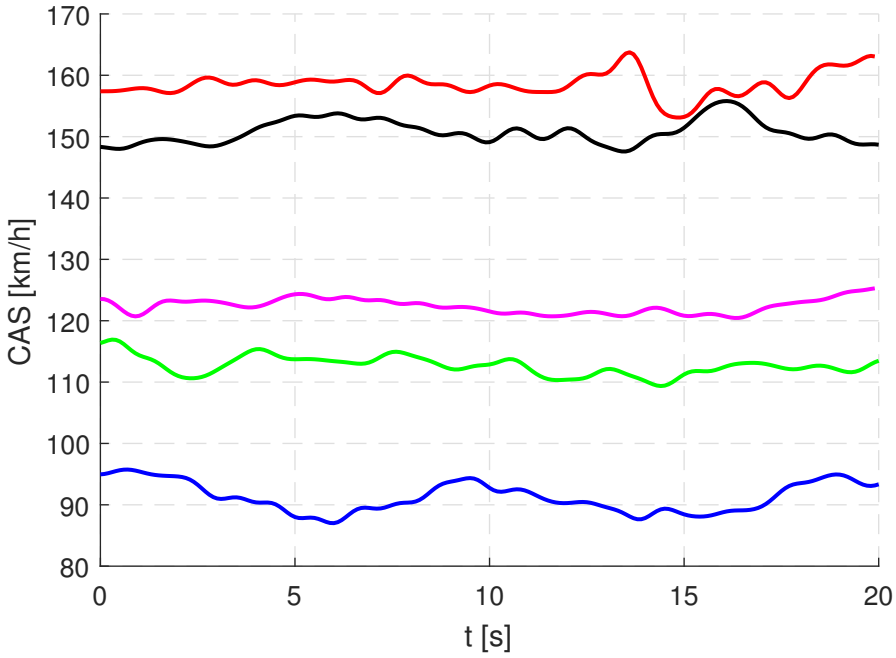

Figure 6.5: Speed during trimmability test, flight 03.1706

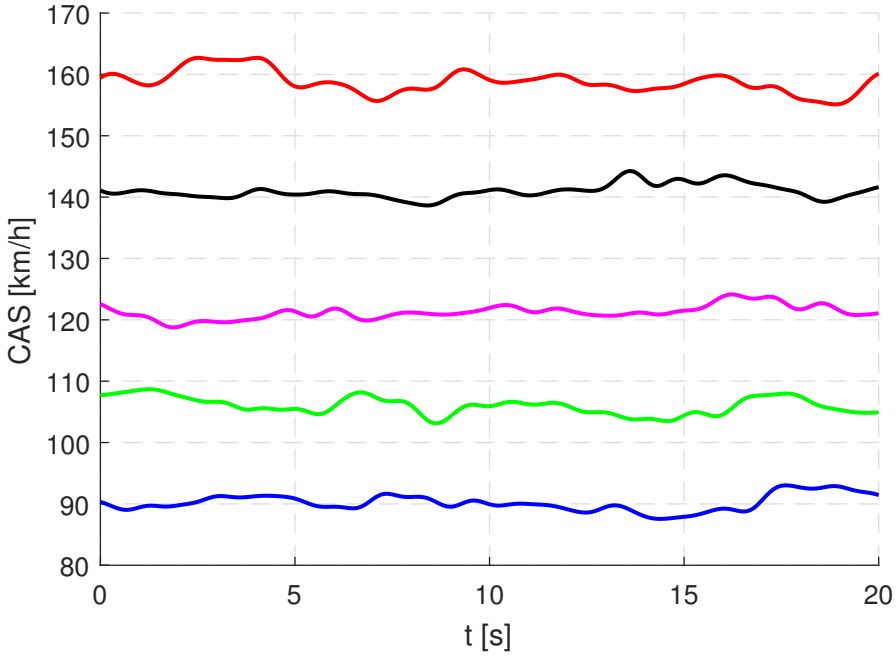

Figure 6.6: Speed during trimmability test, flight 04.1706

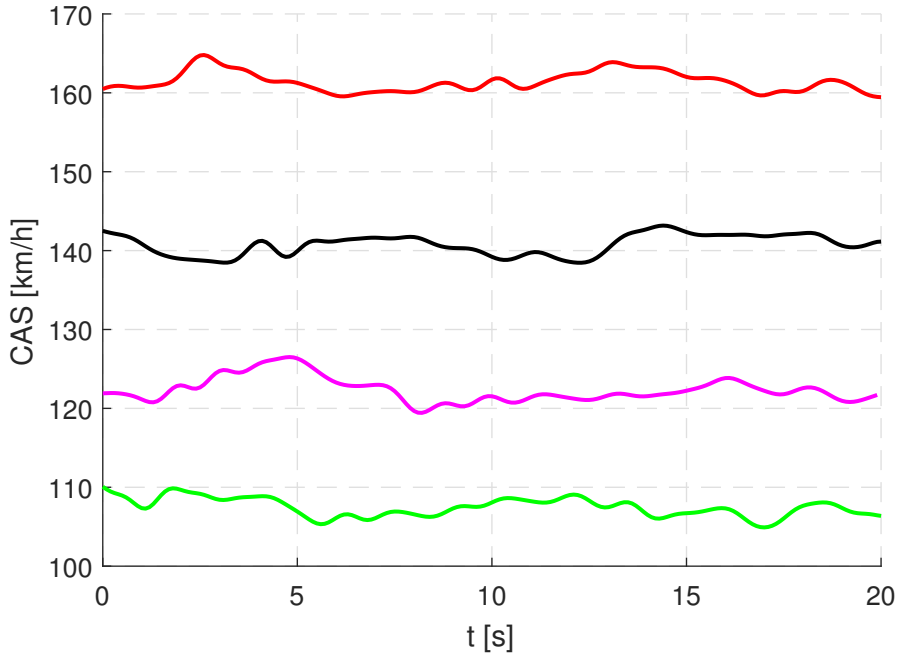

Figure 6.7: Speed during trimmability test, flight 05.1706

6.3.5 Conclusions

Test results are more than enough to assess the aircraft trimmability for all the CG locations along the whole envelope. It is recommended, if there is the need to perform some trim shots during a flight, to execute them with the correct technique and trying to span different velocities in order to save time for a potential successive trim test.

Chapter 7

Static stability test

Static stability concerns the tendency of the aeroplane to return to the equilibrium position after a perturbation. This section concerns longitudinal and lateral-directional stability, by means of speed stability and Steady Heading Side-Slip (SHSS) tests. Both of them have been demonstrated, although the strong influence of the flaps on the air stream on the elevator has been pointed out.

7.1 Static longitudinal stability

7.1.1 Introduction

Speed stability (or *stick force per V*) test translates into an experimental procedure the concept of static stability in the longitudinal plane: if the aircraft tends to return to the equilibrium, it means that the force requested to move it away from the trim condition must grow gradually as the perturbation increases. As already mentioned in the wind-up test (6.2), the stick force needed to move the elevator far from the neutral position is low and, accordingly, the expectation of this test is that a slight stick force is needed to increase or decrease considerably the flight speed.

7.1.2 Test objectives

The test aims at demonstrating that the force requested to move the aircraft from the trim condition should increase with the stick position. Moreover, control has to be instinctive: push the stick to increase and pull to decrease the velocity. No quantitative values are specified for the degree of stability required by LTF-UL 173.

7.1.3 Test execution

Procedure is the same as detailed in CS23 FTG ([1]):

1. Trim the aircraft at the desired airspeed and altitude;
2. Apply a pull force and stabilize at a slower airspeed;
3. Continue this process with appropriate increments (approximately 15-20 km/h), until a velocity close to the minimum for steady flight is reached;
4. Gradually relax the force to allow the aeroplane to return to the trim airspeed;
5. Push the stick and repeat the procedure, with gradual increments until 115% of the original trim airspeed, and gradually relax the stick force to allow the aeroplane to come back to the trim position.

The test has been executed in CR, TO and LND configuration, respectively in flights 03.1706, 04.1106, 02.1106, since the longitudinal static stability is an important topic which must be evaluated in all the possible flap configurations.

7.1.4 Test results

Test results are hereby reported. In order not to weigh down the main corpus of this work, examples of time history for CR, TO and LND configuration can be found in Appendix C.

CR configuration

Fig. 7.1 shows the overall results, with the force gradients obtained for this test.

The gradients are:

- $\frac{\partial F}{\partial V}_{PULL} = -0.32 \frac{N}{km/h}$
- $\frac{\partial F}{\partial V}_{PUSH} = -0.20 \frac{N}{km/h}$
- $\frac{\partial F}{\partial V}_{TOT} = -0.32 \frac{N}{km/h}$

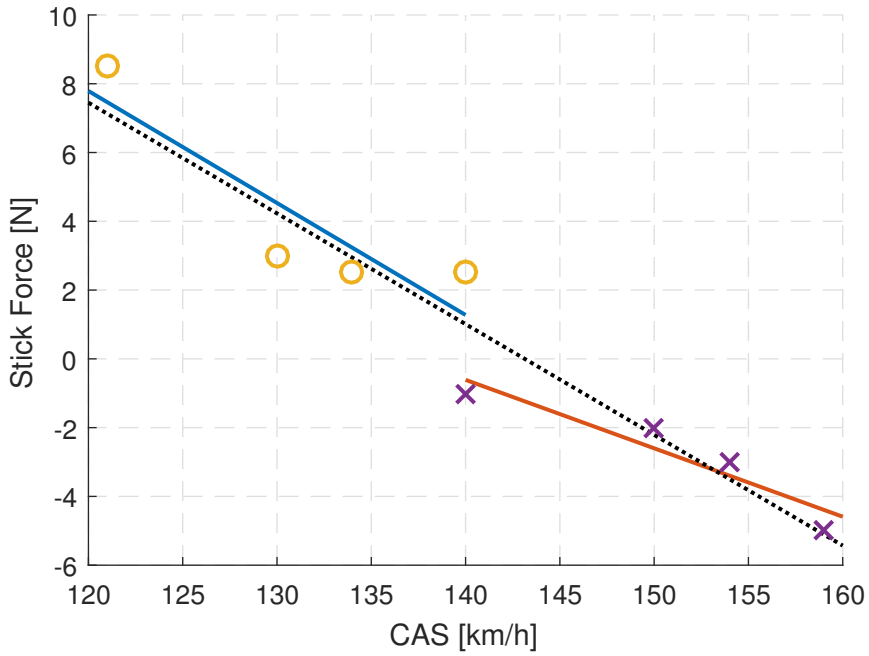

Figure 7.1: Speed stability stick force versus speed, CR configuration.

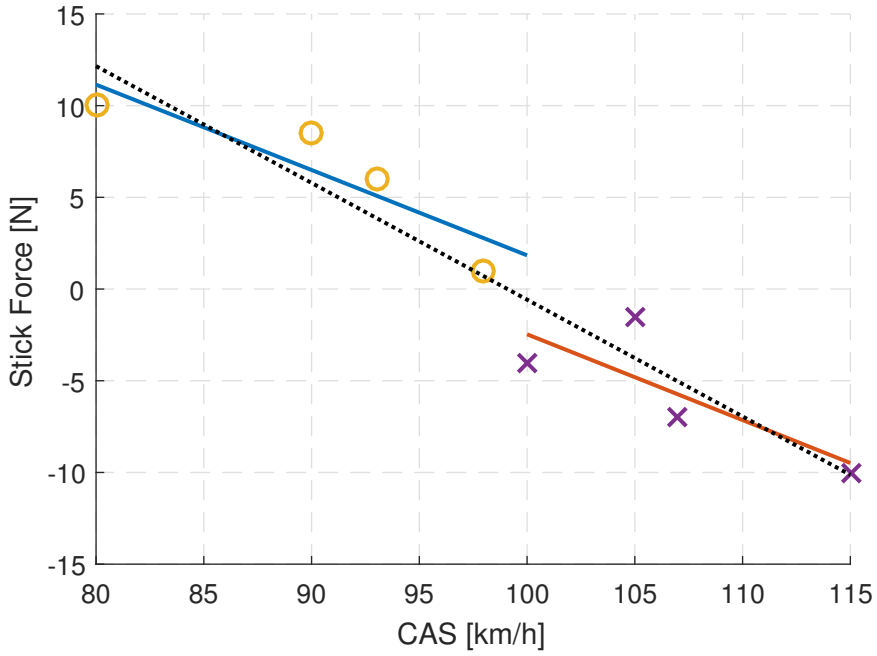

Figure 7.2: Speed stability stick force versus speed, TO configuration.

TO configuration

Fig. 7.2 shows the overall results, with the force gradients obtained for this test.

The gradients are:

- $\frac{\partial F}{\partial V}_{PULL} = -0.47 \frac{N}{km/h}$
- $\frac{\partial F}{\partial V}_{PUSH} = -0.47 \frac{N}{km/h}$
- $\frac{\partial F}{\partial V}_{TOT} = -0.64 \frac{N}{km/h}$

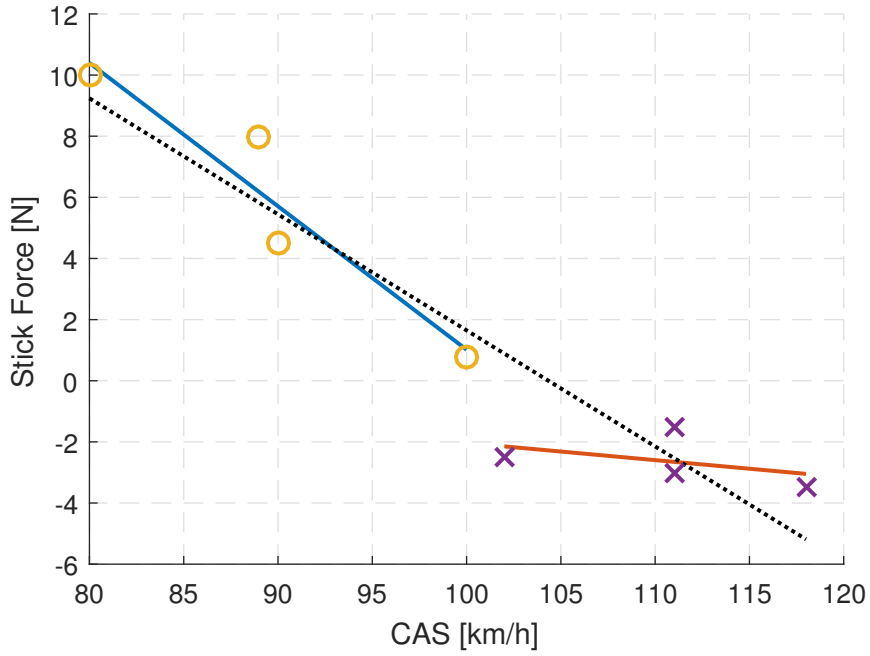

Figure 7.3: Speed stability stick force versus speed, LND configuration.

LND configuration

Fig. 7.3 show the overall results, with the force gradients obtained for this test.

The gradients are:

- $\frac{\partial F}{\partial V}_{PULL} = -0.47 \frac{N}{km/h}$
- $\frac{\partial F}{\partial V}_{PUSH} = -0.06 \frac{N}{km/h}$
- $\frac{\partial F}{\partial V}_{TOT} = -0.38 \frac{N}{km/h}$

7.1.5 Conclusions

Test results are fully satisfactory both in CR and TO configuration: the aircraft is statically stable and the control is instinctive, although the command looks stiffer in TO with respect to CR configuration. An hysteresis is present between push and pull phase due to the command friction. The only drawback is the relatively low force to vary the airspeed of 20 km/h; as already stated (see 6.2.4), the control should be stiffened in order to be more

intuitive to the pilot and preserve the approach to dangerous flight envelope speeds.

In LND configuration the gradient is satisfactory in the pull phase, with a similar gradient to the TO configuration, but the control loses authority during the push phase; this tendency has been observed in all the LND configuration tests and the pilot feedback confirmed what observed in the post-processing phase. One test point, whose results are reported in Appendix C, even showed a positive slope of the regression line during the push phase: it means that the elevator command was sucked down without any effort from the pilot. A reason of this misleading result is that the fully extended flaps cause a down-wash which makes the elevator losing authority when deflected downwards. The manufacturer will verify if the solution to close the gap between flaps and wing, which will be employed to try to reduce stall speed (already discussed in 5.2), is enough to limit the phenomenon.

7.2 Static lateral and directional stability

7.2.1 Introduction

The aircraft is statically stable in the lateral and directional plane when an increase of rudder deflection is necessary to increase the sideslip angle[1]. Simultaneously, an increasing β will cause the aircraft to roll, according to the *dihedral effect*, which induces the pilot to use the ailerons to maintain the steady flight. The strength of this coupling effect is found by measuring the amount of rudder and aileron deflection necessary to maintain the steady flight: the higher is rudder deflection, the higher is directional stability; the higher aileron deflection, the higher is dihedral effect.

7.2.2 Test objectives

The requests of the normative can be briefly summarized in the following sign requirements on the derivatives:

- $\dfrac{\partial \beta}{\partial \delta_R} > 0$
- $\dfrac{\partial \delta_A}{\partial \delta_R} < 0$

7.2.3 Test execution

Static lateral-directional stability has been demonstrated through a series of steady heading side-slip, during flights 07.1006 and 01.1706 for CR configuration, 05.1106 and 06.1106 for TO one. Test procedure is the following:

1. Trim the aircraft at the desired trim airspeed and flap configuration;
2. Increase the sideslip angle of about 10° with one pedal and maintain the steady heading with the ailerons;
3. Increase the sideslip angle with the same pedal until the limit;
4. Slowly release the pedals to let the aircraft go back to the trim position;
5. Repeat in the opposite direction.

[1]The adopted convention is generally $\beta > 0$ when the wind comes from the right and $\delta_R > 0$ when rudder is deflected to the left.

The analyses of this section focus on one test point of flight 01.1706 for CR configuration and one test point of 05.1106 flight for TO configuration. Further graphs of other test points, with examples of time history, are available in the Appendix C.

7.2.4 Test results and conclusions

Test results are hereby reported. In order not to weigh down the main corpus of this work, examples of time history for both CR and TO configuration can be found in Appendix C.

CR configuration

The results in terms of gradients (Figg. 7.4 and 7.5) are:

- $\frac{\partial \beta}{\partial \delta_R} = 1.22$
- $\frac{\partial \delta_A}{\partial \delta_R} = -0.46$

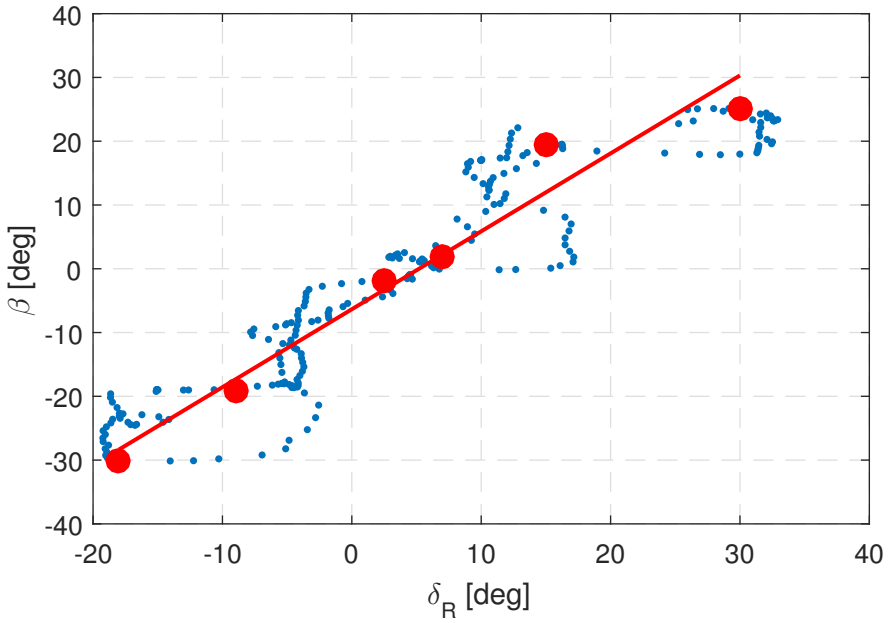

Figure 7.4: SHSS β vs δ_R, CR configuration, flight 01.1706 TOP 9.

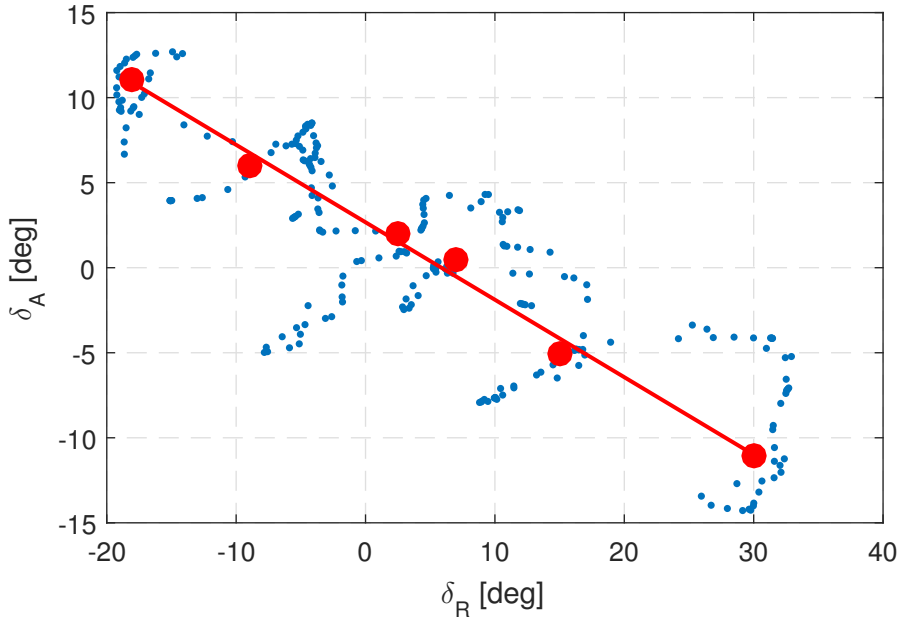

Figure 7.5: SHSS δ_A vs δ_R, CR configuration, flight 01.1706 TOP 9.

TO configuration

The results in terms of gradients (Figg. 7.6 and 7.7) are: The found gradients are:

- $\frac{\partial \beta}{\partial \delta_R} = 1.30$
- $\frac{\partial \delta_A}{\partial \delta_R} = -0.47$

7.2.5 Conclusions

Static lateral-directional stability has been proved in CR and TO configuration. Time history shows how roll angle tends to increase when sideslip angle increases, but it is promptly corrected by the pilot with the ailerons. Pitch angle has a slight decrease at the end of the test when sideslip angle returns to the initial position. Gradients are almost the same in CR and TO configuration: it means that the rudder authority is not lowered by the air stream down-wash from flaps in TO position. Unfortunately, the same cannot be said for the LND configuration, since no test point with full flaps has been executed for logistic constraints.

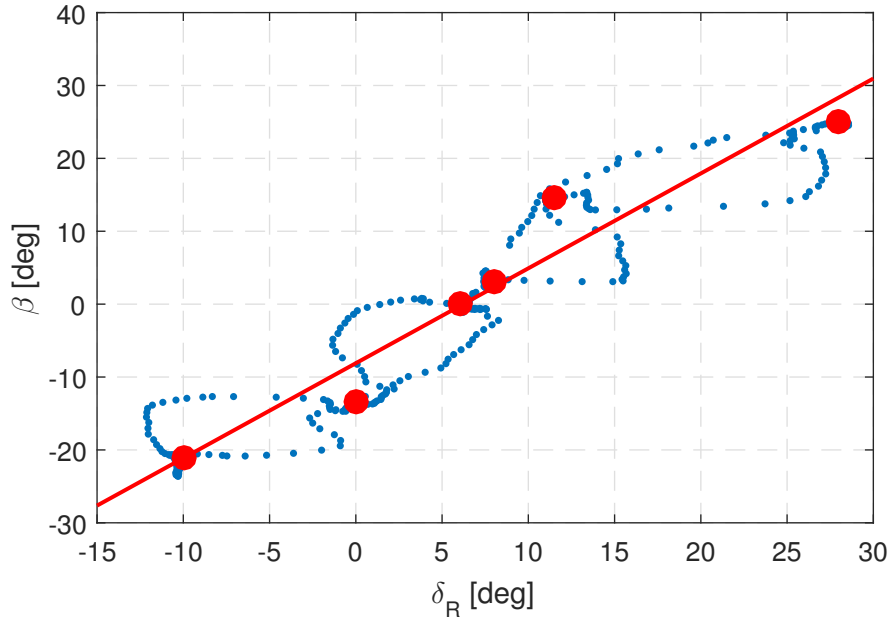

Figure 7.6: SHSS β vs δ_R, CR configuration, flight 05.1106 TOP 9.

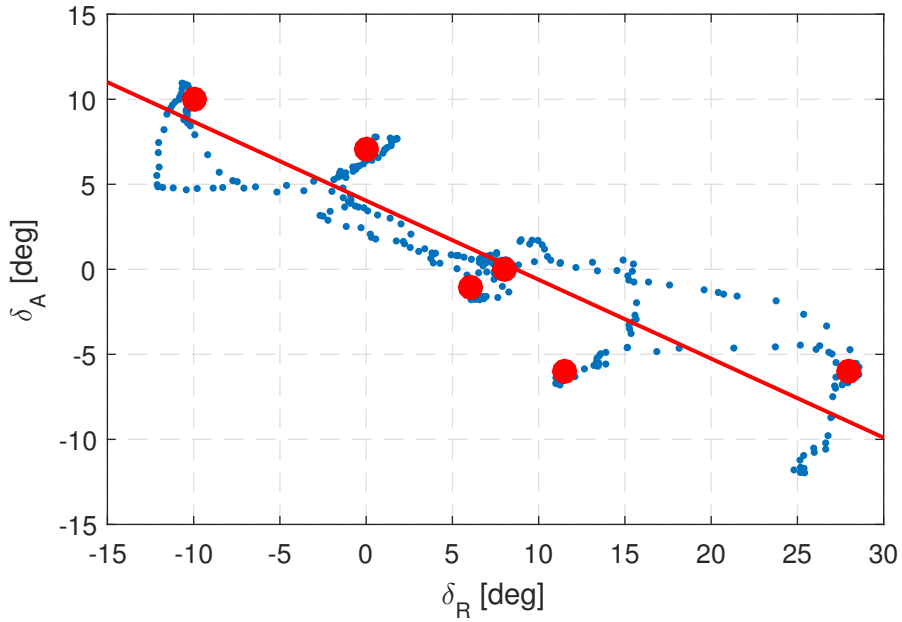

Figure 7.7: SHSS δ_A vs δ_R, CR configuration, flight 05.1106 TOP 9.

It is observable a decrease of the $\frac{\partial \beta}{\partial \delta_R}$ gradient at higher speed: Appendix C shows other two test points at higher speed, namely 110 km/h for TO con-

figuration and 130 km/h for CR one. It means that an increase of speed reduces the rudder effectiveness on the directional plane; no substantial differences are observed with speed on the dihedral effect.

It is not seldom that during a SHSS test, some aircraft encounters a phenomenon called *rudder lock*, which consists in a reduction of the pedal force at high sideslip angles. It is due to the loss of authority of the rudder, partially hidden by the vertical fin. Unfortunately the aircraft was not equipped with a load cell to measure the force on the pedals, nevertheless the pilot did not experience any kind of rudder lock in any of the tests performed, both in CR and TO configuration.

Chapter 8

Dynamic stability test

LTF-UL is very brief about dynamic stability: it prescribes that any short period mode must be heavily damped. It is not clear whether *short period* means the longitudinal motion of the aircraft which has exactly this name, or, more in general, any fast oscillation of the aircraft both for longitudinal and lateral-directional motion. CS23 is more detailed, as a matter of fact it prescribes that all the dynamic modes of the aircraft, namely short period, phugoid and Dutch roll, must be damped in all the configurations. For reasons of time, only CR and LND configurations have been tested: if stability is proved for the most extreme flap conditions, the aircraft must be stable also in the TO one. Dynamic stability tests aim at demonstrating that all the aircraft modes are damped and do not endanger the normal flight conditions.

8.1 Short period

8.1.1 Introduction

Short period is very difficult to excite because of its heavy damping and high frequency. Generally, it is not of interest during a UL flight test campaign, because of its damping makes the frequency not dangerous for the aircraft; as a matter of fact, in the past test campaign no short period test has been executed.

Tornado model of the aircraft has been used to predict short period frequency, which results to be $\hat{\omega}_{SP} = 2.65$ rad/s at a speed of 100 km/h; the procedure and the hypothesis which have been employed to predict this frequency are detailed in Appendix C. An appropriate procedure for frequency sweep is necessary, in order to be sure to have excited in the best way the whole frequency spectrum interested by short period mode.

8.1.2 Test objective

Test objective is to assess the correct damping of short period mode, besides to evaluate its frequency.

8.1.3 Test execution

The best input to induce this motion is the doublet, because it tends to suppress phugoid and provides a pure short period mode. The doublet causes a pitch attitude deviation in one direction, then cancels it with an input in the opposite direction, in order to have a null total deviation in pitch attitude. The movement should be fast enough to excite the high frequency of the short period. Jategaonkar ([14]) suggests an empiric formula to find out the best doublet semi-period to excite the mode:

$$\Delta t_{\mathrm{DBLT}} = \frac{2.3}{\hat{\omega}_{SP}} \tag{8.1}$$

With the supposed value of $\hat{\omega}_{SP}$, the value of doublet period should be $\Delta t_{\mathrm{DBLT}} \approx 0.85$ s. Moreover, according to the analysis of Appendix C, higher airspeed makes short period faster and, consequently, more difficult to excite. Trim speed has been 100 km/h: far from stall, but low enough not to make the manoeuvre too abrupt and difficult. Test procedure is the following:

1. Trim the aircraft at 100 km/h;
2. With a reduced stick excursion, try to excite the aircraft with:

   $\Delta t_{\mathrm{DBLT}} = 0.5$ s,

   $\Delta t_{\mathrm{DBLT}} = 1$ s,

   $\Delta t_{\mathrm{DBLT}} \approx 0.75$ s (an intermediate value between the previous two);
3. If no short period motion has been experienced, the procedure is repeated with an increased stick displacement.

Short period test took place in the 05.1706 flight and in other previous flights, to increase the pilot sensitivity to the mode. Flight 05.1706 has been performed with a full aft CG.

8.1.4 Test results

Short period excitation has been attempted five times during flight 05.1706, trying to vary the doublet input period every time, as far as possible with a

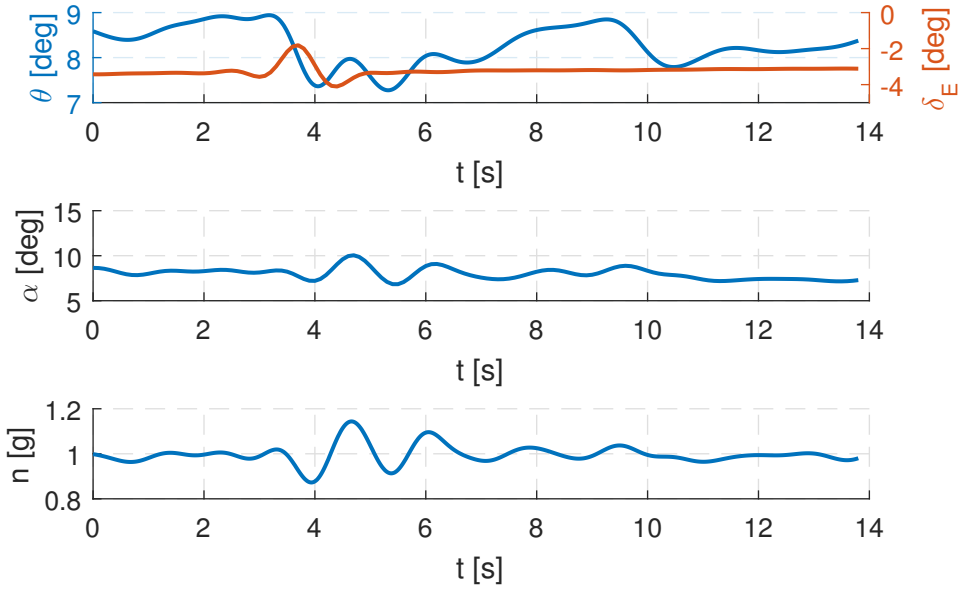

Figure 8.1: Time history during short period test, flight 05.1706, TOP 7

human hand. One of these five attempts succeeded, with a very good result, as shown in Fig. 8.1.

Pitch angle has an oscillatory motion after the input, but it is not clear enough to understand whether a short period has been excited or not. Angle of attack and load factor clarify all the doubts: angle of attack has a manifest oscillatory motion, as much as vertical acceleration; after the doublet input the aircraft started a slight climb, as proved by the increase of pitch angle and the constant angle of attack. The test results in terms of period, ω_{SP} and Δt_{DBLT} are reported in Tab. 8.1.

Table 8.1: Short period test results, flight 05.1706, TOP 7.

$\overline{T}$ [s]	ξ [-]	ω_{SP} [rad/s]	Δt_{DBLT} [s]
1.5	2 cycles	4.18	0.8

8.1.5 Conclusions

Test result is fully satisfactory: firstly, short period has been clearly excited, which is not trivial given the mode characteristics, and it does not constitute a danger for the flight safety; secondly, the mode frequency has been calculated and it is possible to develop further analyses on a numerical model of the

aircraft.

Mode frequency has been badly predicted by the Tornado model, which underestimated it of 1.5 rad/s. The main reason can be the inertia prediction, which has been executed with Roskam ([23]), as detailed in Appendix C, by means of a comparison with other airplanes and therefore it is not accurate. Tornado model showed is reliability for neutral point estimation and it is less likely to be the cause of the bad prediction, as long as the approximation of constant airspeed, which has been verified in the post processing phase. Jategaonkar formula to predict doublet semi-period shows its unreliability, too; in fact, according to it and to the value of short period frequency, the semi-period of the doublet would be 0.55 s. The difference is 0.25 s, imperceptible by the pilot's hand, but it is quite lower with respect to the predicted one.

8.2 Phugoid

8.2.1 Introduction

Phugoid has a longer period than short period mode and it is regarded as not dangerous for the flight management, since it can be easily controlled by the pilot. Test procedure is simpler than the one of short period: phugoid frequency is more feasible by the pilot and the input magnitude is not dangerous for the aircraft. The former campaign showed a fully satisfactory result about phugoid response.

8.2.2 Test objective

Test objective is to assess the correct damping of the phugoid mode, besides to evaluate its frequency.

8.2.3 Test execution

An appropriate control input for the phugoid is a relatively slow elevator pulse to cause the aircraft to increase and decrease speed from the trim point. Once the speed deviation is attained, the control is moved back and released (CS23 FTG, [1]).

Phugoid test has been executed during flights 05.1006 and 06.1006 with CR configuration, during flights 03.1006 and 04.1006 with LND configuration.

8.2.4 Test results

Phugoid test results are reported in Fig. 8.2 for CR configuration and in Fig. 8.3 for LND configuration.

From the CAS time history it is possible to obtain the phugoid mode basic information, like period, ω_{PH} and Δt_{IMP}, as much as the number of cycles to damp the mode. Results are summarized in Tab. 8.2. Phugoid mode affects generally the cruise flight, as a matter of fact the oscillation after elevator input in LND configuration is not as clear as the one with zero degrees of flap.

The CS23 FTG procedure has been respected: the elevator comes back to the original position and is released, as shown by the null stick force for all the oscillation duration. Pitch angle oscillates with the same characteristics of the airspeed, but with a slight delay and in counterphase; it can be used

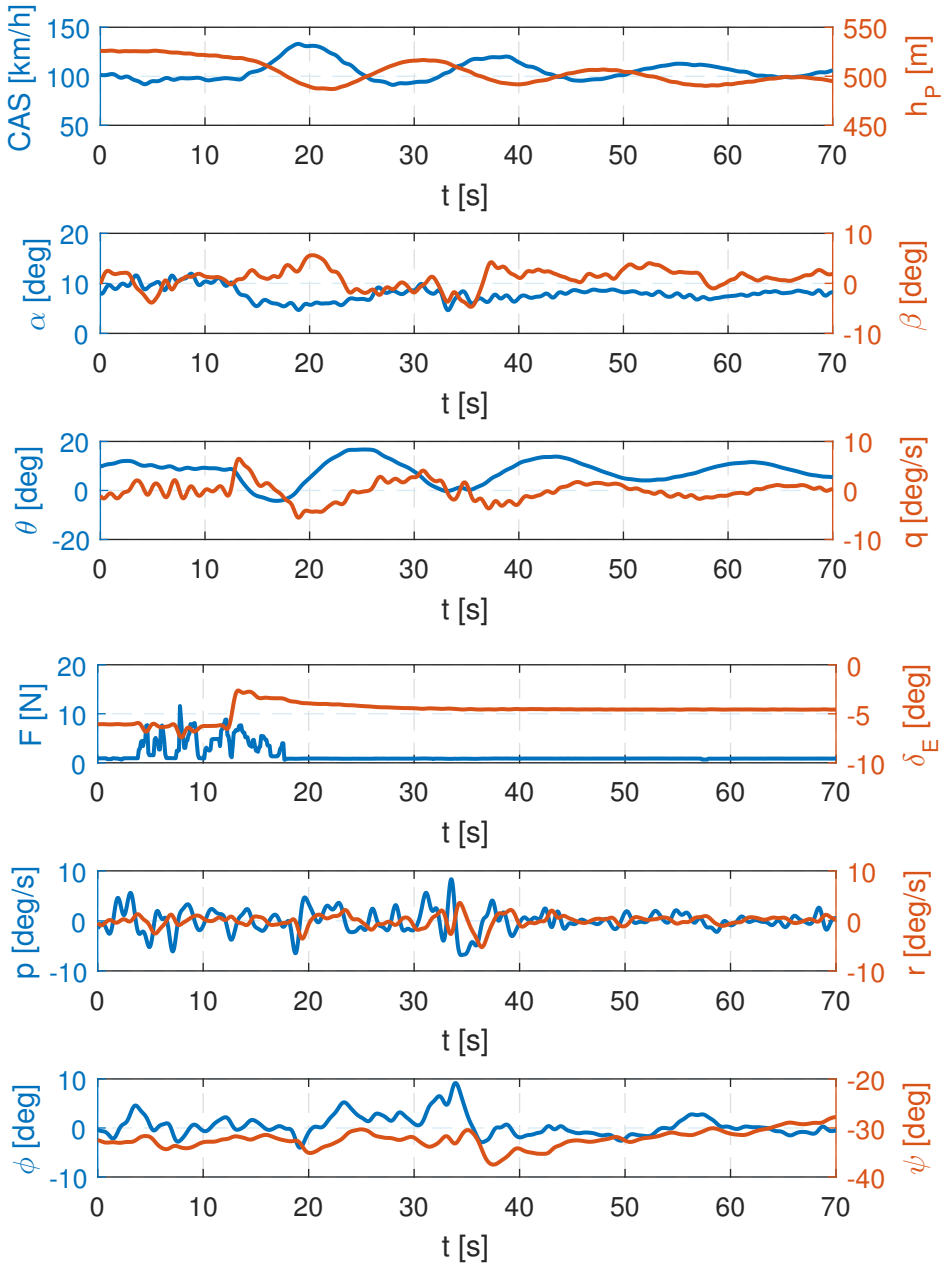

Figure 8.2: Phugoid test time history, CR configuration, flight 05.1006, TOP 7.

to determine the mode characteristics as much as the airspeed. Angle of attack, as expected, is constant during the oscillations. Sideslip and yaw angle fluctuate of no more than 5 degrees, which testifies the absence of directional motion; roll angle experiences larger fluctuations, but never exceeds $\pm 10°$.

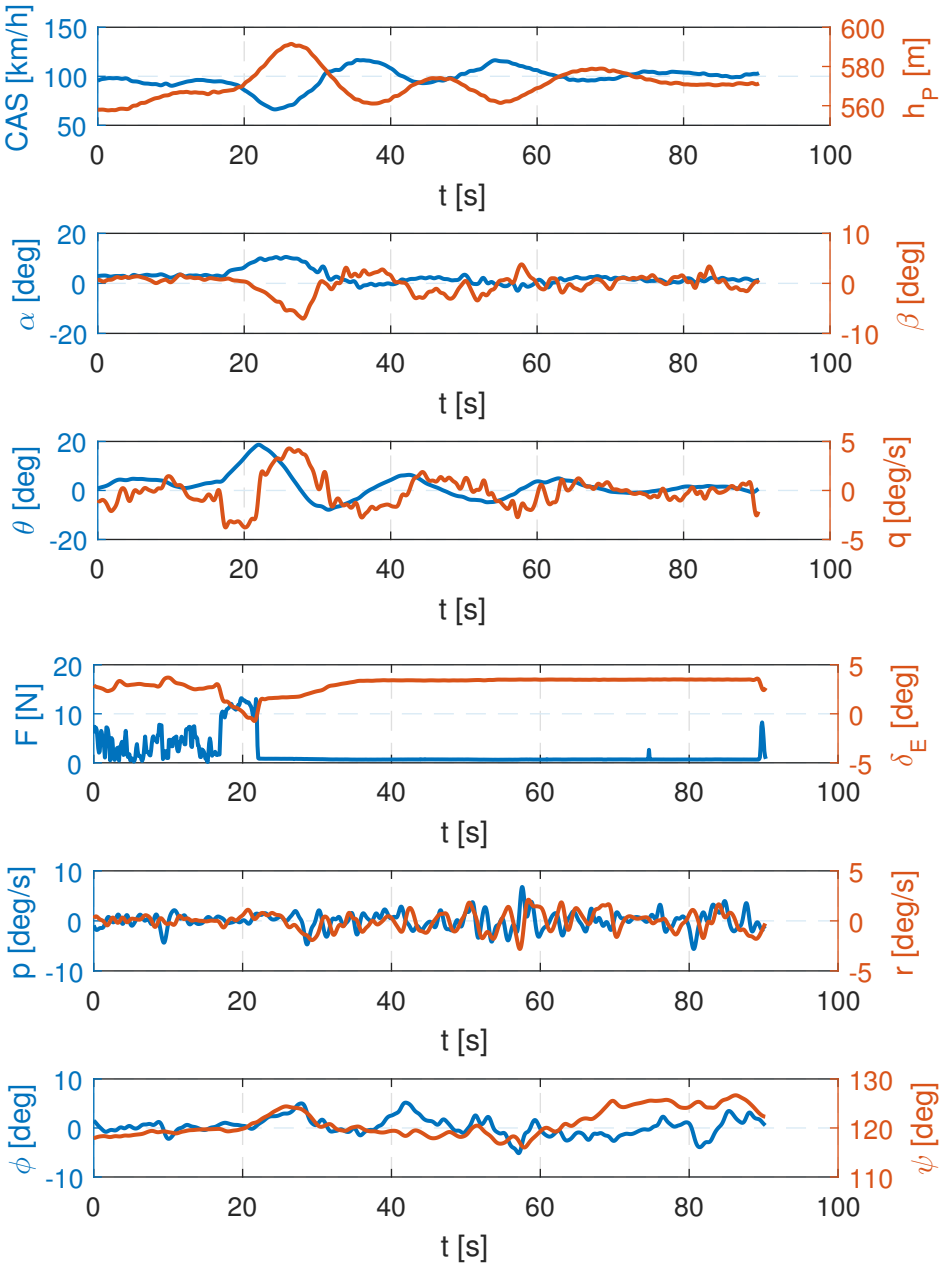

Figure 8.3: Phugoid test time history, LND configuration, flight 04.1006, TOP 7.

Is can be stated that the phugoid mode has been excited in the proper way, without any lateral-directional influence.

Table 8.2: Phugoid test results, both in CR and LND configuration, flights 05.1006 and 04.1006.

Conf.	$\overline{T}$ [s]	ξ [-]	ω_{PH} [rad/s]	Δt_{IMP} [s]
CR	18	3 cycles	0.35	5
LND	20	2 cycles	0.31	5

8.2.5 Conclusions

The test shows an appreciable behaviour to phugoid excitation and excellent damping characteristics, similar to the ones obtained with the former aircraft. However, LTF-UL requires the test with fixed commands, too; CS23, which LTF-UL comes from, has the same request. Theoretically, if the aircraft has a certain response with free commands, it should definitely have a more damped oscillation if the pilot holds the bar in position. This theoretical assumption has been confirmed during flight test. For sake of brevity, only remarkable results are reported in this section; the reader is asked to refer to Appendix C for more phugoid graphs, executed with different techniques.

8.3 Dutch-Roll

8.3.1 Introduction

Dutch roll is an oscillating movement with coupling effects between roll and yaw. The frequency covers a medium-low range, between 0.4 and 4 rad/s, as much as the damping. The mode is not dangerous for the flight management, but it can be very annoying for the passengers; therefore, it must be heavily damped.

8.3.2 Test objective

Test objective is to assess the correct damping of the Dutch roll mode, besides to evaluate its frequency.

8.3.3 Test execution

Flight technique consists in applying alternating left and right rudder inputs to excite and reinforce the Dutch-roll mode; the input has to go on, with increasing frequency, until an oscillatory motion is attained. The Dutch-roll method is a kind of *trial and error*, since the pilot sensitivity should understand when the proper input frequency is reached and stop the rudder pulsing. When the oscillation is reached, the pilot can alternatively return the pedals to trim position and release or restrain them in the trim position.

Dutch roll test has been executed during flights 01.1006 and 02.1006 with CR configuration, 07.1106 and 08.1106 with LND configuration.

8.3.4 Test results

Dutch roll test results are reported in Fig. 8.4 for CR configuration and in Fig. 8.5 for LND configuration.

8.3.5 Conclusions

During all the flights devoted to the Dutch roll mode test, there has been no way to excite this mode. As it is clear from the graphs, once the rudder input ceases, the aircraft stabilizes itself with null sideslip, roll and yaw angles, both in CR and LND configuration. The reason of this non-sensitivity to Dutch roll excitation is to find firstly in the deep lateral-directional stability of the aircraft, confirmed by all the tests executed. Secondly, the flight technique has not been the canonical one prescribed in CS23 FTG, since it is not visible

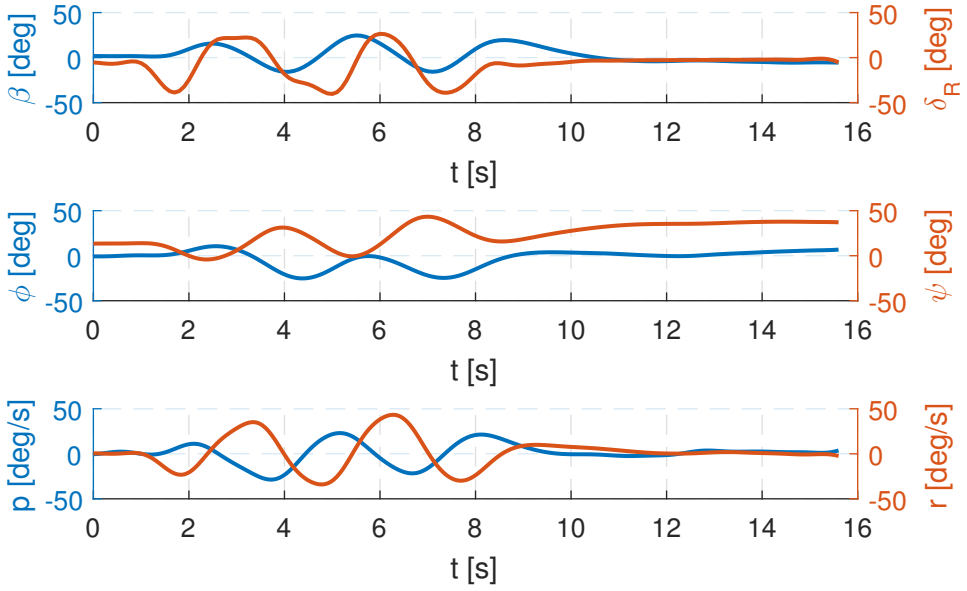

Figure 8.4: Time history during dutch roll test, CR configuration, flight 01.1006, TOP 12

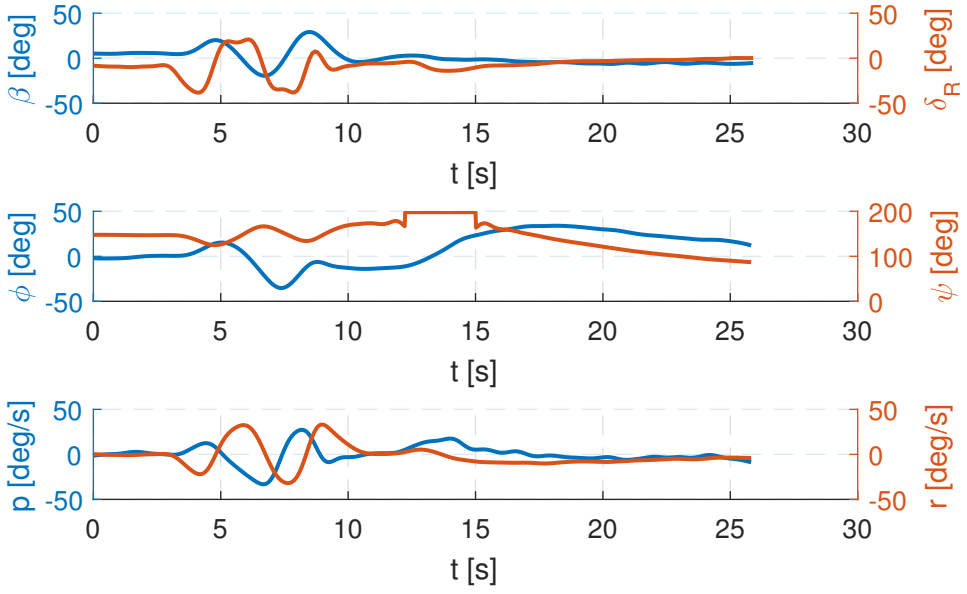

Figure 8.5: Time history during dutch roll test, LND configuration, flight 01.1006, TOP 12

a proper frequency sweep with the rudder pulse. In the tests whose time histories are presented in this section the semi-period of the excitation has been a fixed value of $\Delta t_{\mathrm{RUDD}} = 1.5$ s repeated five times for CR configuration

and $\Delta t_{\mathrm{RUDD}} = 1.8$ s repeated three times for LND configuration. Although the lateral-directional dynamic stability of the aircraft is confirmed, it is necessary to execute the procedure of the Flight Test Guide in order to demonstrate the aircraft full compliance.

Chapter 9

Additional analysis

This chapter groups the results of tests which are not directly linked to the certification requirements, namely neutral point position estimation and drag polar characteristics. Neutral point has been firstly localized with a series of flights with different CG positions and the results has been compared with the one originating from a Tornado model of the G70 and then with the result with the empirical values from the well-known Airplane Design of Roskam ([24]).

The drag polar curve has been obtained by means of glide tests and provided a very good result in terms of data scattering, namely the points were well disposed for being approximated by a 2nd order curve. Thanks to the drag polar curve, it is possible to calculate the drag constants C_{D0} and K.

9.1 Stick-fixed neutral point estimation

9.1.1 Introduction

Neutral point, that is the aerodynamic center of the aircraft, is the point where pitch moment does not depend on incidence. Its position is useful to be identified for a double reason: firstly, it provides an important indication of the theoretical aft CG limit, because the condition of static stability requires the CG in front of the neutral point; secondly, the information provides a reliable value to develop a two surfaces model of the aircraft, for further analyses.

Firstly, neutral point has been located with an experimental procedure, and then the result has been compared with the one obtained by means of two theoretical procedures: one is based on a Tornado model, whereas

the other concerns a two-surface model whose parameters have been found with the empirical formulas provided by Roskam ([24]). The Tornado model reproduces the exact aircraft geometry and the same flight conditions, with an uncertainty linked to the fuselage shape, which is obtained by means of two orthogonal panels.

The neutral point of the first G70 was located at 49% MAC, which is not supposed to be greatly changed in the present campaign.

9.1.2 Test objectives

Test objective is the neutral point estimation with:

- experimental procedure based on the execution of three trim tests with CG location substantially different between the flights;
- numerical procedure with the Vortex-Lattice method employed in Tornado;
- two-surface model approach with the aerodynamic coefficients obtained with *Airplane Design VI*, by Roskam.

9.1.3 Test execution

Experimental procedure

Stick-fixed neutral point position is derived through a series of trim shots performed with different longitudinal balancing and airspeeds. Every flight requires an exact indication of CAS and elevator deflection during the test. Once all these information are available, it is possible to plot the elevator deflection $\delta_{E,eq}$ as a function of $C_{L,eq}$, with

$$C_{L,eq} = \frac{2W/S}{\rho_0 V_{CAS}^2} \tag{9.1}$$

A linear regression between all these points provides a relation with negative slope:

$$\frac{\partial \delta_{E,eq}}{\partial C_{L,eq}} = -\frac{C_{L/\alpha}}{\Delta}\frac{X_G - X_N}{c} < 0 \tag{9.2}$$

where Δ is a parameter indepentent of X_G:

$$\Delta = C_{L/\alpha}C_{M/\delta_E} - C_{M/\alpha}C_{L/\delta_E} < 0 \tag{9.3}$$

All the $\frac{\partial \delta_{E,eq}}{\partial C_{L,eq}}$ slopes have to be plotted as a function of the X_G position and a linear regression between them is drawn. Stick-fixed neutral point position is that point where:

$$\frac{\partial \delta_{E,eq}}{\partial C_{L,eq}} = 0 \tag{9.4}$$

Flights devoted to this topic have been the same of the trimmability test:

- Flight 03.1706, with $X_G = 32\%$ MAC;
- Flight 04.1706, with $X_G = 25\%$ MAC;
- Flight 05.1706, with $X_G = 35\%$ MAC.

Trim speeds are reported in Tab. 9.1

Table 9.1: Trim speeds during neutral point estimation test.

Flight	$V_{\text{CAS,trim}}$ [km/h]
03.1706	90, 120, 130, 160, 170
04.1706	90, 110, 130, 150, 170
05.1706	110, 130, 150, 170

For best accuracy, the aircraft was weighted before and after each flight, with the complete crew on board in order to extrapolate the X_G position of each flight. Test procedure is the same of trimmability test: the reader would refer to 6.3.3 for further details.

Tornado model

By definition the neutral point is the N point with respect to pitch moment is not influenced by α:

$$C_{MN,\alpha} = 0 \tag{9.5}$$

Therefore, $C_{M,\alpha}$ is computed with Tornado for different CG locations and a linear regression is drawn; the point which satisfies Eq. 9.5 represents the neutral point location.

Two-surface model

By means of a two-surface model of the aircraft, which has been formulated following the formulation by Atkin ([10]) and Trainelli ([28]), it is possible to

find out the position of the neutral point along the airfoil, normalized with respect to the MAC, which, according to [28], is located at:

$$\xi_N = \xi_A^{wb} - \frac{\tau}{1+\tau}(\xi_A^{wb} - \xi_A^t) \tag{9.6}$$

This value increases from aft to bow; hence, if one considers the aerodynamic center of the tail as the origin of the reference frame, the ξ_A^{wb} term becomes the distance between the aerodynamic centers of tail and wing-body.
τ is a positive, non-dimensional, parameter, defined as:

$$\tau := \eta \frac{S_t}{S} \frac{a^t}{a^{wb}}(1 - \epsilon_{,\alpha}) \tag{9.7}$$

In detail:

- η is the *tail efficiency*, that is the ratio between the dynamic pressure of the tail and the one on the wing. The former depends on the location of the tail: if the tail is located in the wake of the wing or the fuselage, the dynamic pressure on it will be less than the free-stream value; otherwise, if the tail is in the slipstream of the propeller, its dynamic pressure will be greater than the one in the free-stream. Its value is normally between 0.8 and 1.2 ([20]) and for our purposes it can be taken as equal to one.

- The ratio between wing and horizontal empennage surfaces is way lower than one, in our airplane $\frac{S_t}{S} = 0.22$.

- Lift coefficient slopes of tail and wing-body are found out thanks to the experimental formulas reported by Roskam ([24]), which, without considering the terms due to the Mach number, negligible for the condition existing in this test, is:

$$a^{wb} = \frac{2\pi\lambda}{2 + \sqrt{\frac{\lambda^2}{k^2} + 4}} \tag{9.8}$$

  where:

$$k = \frac{C_{l_\alpha}}{2\pi} \tag{9.9}$$

  C_{l_α} is the airfoil lift slope, specifically a NACA 2415, experimentally determined thanks to Abbott in [8]. The formula is the same for the horizontal empennage, with the only difference in the tail airfoil, which is a NACA 0012 symmetric one.

- $\epsilon_{,\alpha}$ is the slope of the linear function describing the downwash angle on the tail due to the wing. It is determined with another experimental formula from Roskam ([24], p. 272), which accounts wing aspect ratio, a^{wb}, sweep angle and the horizontal and vertical distance between wing and tail.

- The aerodynamic center of the horizontal empennage can be located at 25% of the tail chord without losing accuracy in the results, as expressed by Roskam itself, which suggests this simplification for aspect ratios above 5 and sweep angles below 35 degrees.

- The aerodynamic center of the wing body configuration does not coincide with the aerodynamic center of the wing alone, since by adding the fuselage a destabilizing effect rises, namely the aerodynamic center is shifted forward, towards the center of gravity ([13]). Roskam ([24], p. 320) provides a method to determine the shift of the aerodynamic center due to the adding of the fuselage, starting from its position in the alone wing, taken as the 25% of the MAC, as already stated for the horizontal empennage. The method consists in the division of the fuselage into 13 parts along its length, each of them with specific characteristics of width w_i and length Δx_i, which contribute to the definition of the down-wash gradient provided by each of the fuselage partitions. For sake of brevity, the detailed procedure is not reported, but the reader might refer to [24] for the full method.
  The shift of the aerodynamic center depends on:

$$\Delta x_A^{wb} = f(w_i, \Delta x_i, \epsilon_{\alpha_i}(w_i, \Delta x_i)) \tag{9.10}$$

  It is worthy to underline that Δx_A^{wb} is positive from bow to aft, therefore its sign will be most likely negative, since the fuselage contribution is destabilizing.

9.1.4 Test results

Experimental procedure

$\delta_{E,eq}$ versus $C_{L,eq}$ are shown in Fig. 9.1 and the linear regression between all the $\dfrac{\partial \delta_{E,eq}}{\partial C_{L,eq}}$ slopes versus X_G is in Fig. 9.2. The stick-fixed neutral point position is:

$$X_N = 46.2\% MAC \tag{9.11}$$

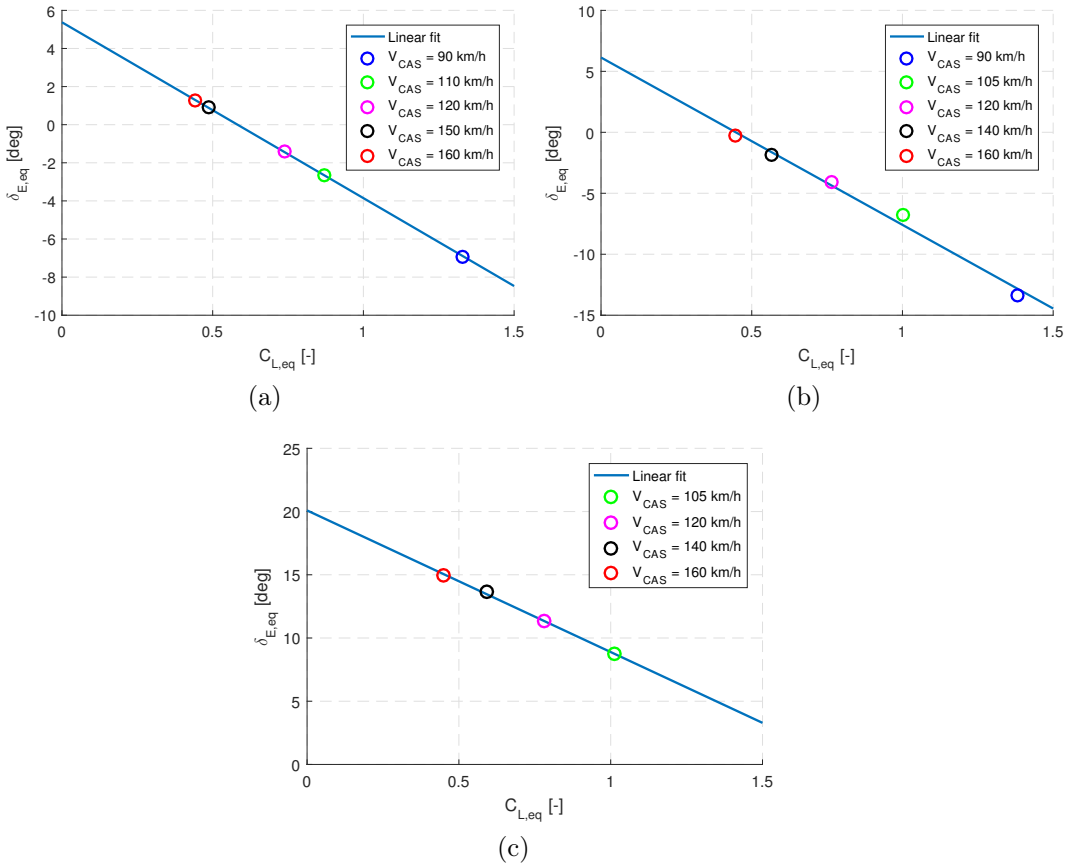

Figure 9.1: $\delta_{E,eq}$ versus $C_{L,eq}$ slopes, with X_G position in % of the MAC equal to 32 (9.1a), 25 (9.1b) and 35 (9.1c).

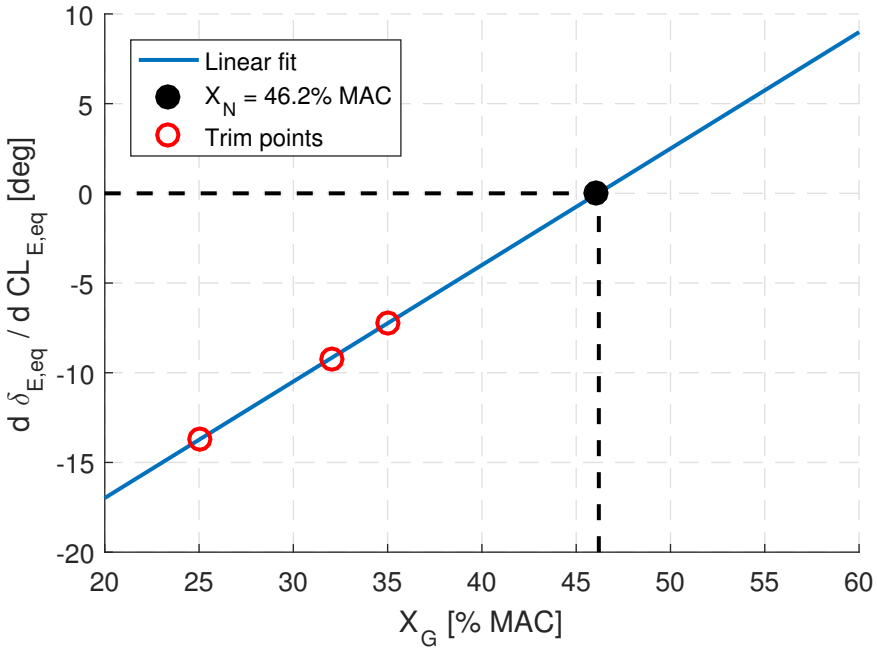

Figure 9.2: Stick-fixed neutral point position according to the experimental test.

Tornado model

The result, as shown in Fig. 9.3, is:

$$X_N = 46.1\% MAC \tag{9.12}$$

Two surfaces model

The obtained values are reported:

- $a^t = 3.43$ 1/rad;
- $a^{wb} = 4.70$ 1/rad;
- $\epsilon_\alpha = 0.44$;
- $\Delta x_A^{wb} = -2.50$ cm.

The position of the neutral point with the two-surface model and the empirical formulas of Roskam is:

$$X_N = 47.1\% MAC \tag{9.13}$$

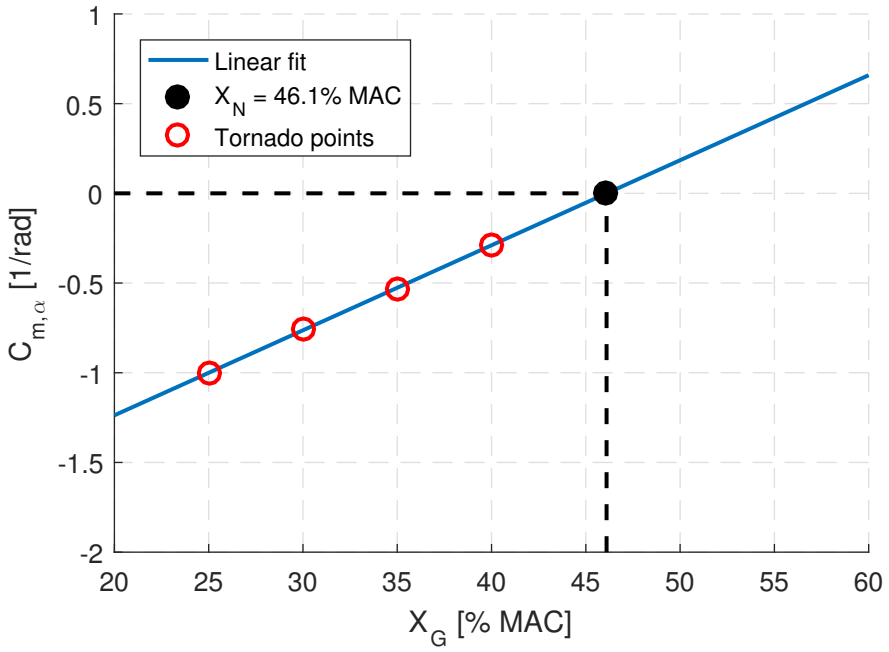

Figure 9.3: Stick-fixed neutral point position according to the Tornado model.

9.1.5 Conclusions

The result with the in-flight procedure is similar to the one obtained by Gadarco and Terzaghi ([11]) for the first generation of Nando Groppo G70, whose stick-fixed neutral point was estimated at 49% of the MAC. The difference is slight, but it is definitely due to the differences in terms of fuselage between the two generations of G70; additionally, the improved configuration of the trim tab (2.1.2) might have influenced the results. Tornado model provides the same result obtained with the experimental procedure: this fact enforces the quality of the model, capable to produce the same results in terms of longitudinal stability derivative of the real aircraft, although considering the fuselage made of two orthogonal planes. Even the two surfaces output is in accordance with the previous two and, in spite of the empirical nature of the method, the error with respect to the in-flight calculation is minimal, equal to the 0.9% of MAC; translated in metrical units, it means that the model, fed with the empiric Roskam coefficients, miscalculates the neutral point position of 1 cm.

9.2 Drag polar estimation

9.2.1 Introduction

For drag polar estimation two different approaches have been followed: sawtooth glides and speed powers through trim test. The advantage of the former is that the whole process is less subject to error, since the test is relatively simple, with only two parameters to record in-flight, namely time and altitude at different airspeeds without any data reduction; the weight is noted before and after the flight and, if the IAS has been maintained constant during the sawtooth glides, it is possible to calculate the CAS by means of the anemometer calibration: the margin of error is minimum. The drawback of this approach is that only high C_L test points are feasible: test is executed with the idle throttle, which allows to explore only a medium-low speed range. The advantage of drag polar estimation with speed power test is in the possibility to explore the whole speed envelope and consequently to obtain data for a wider range of C_L with respect to the glide test. The drawback is that data are more subject to error, especially in the C_D calculation, for the following reasons:

- the BHP is calculated from the engine chart provided by the manufacturer, which is not that detailed as necessary and a certain degree of uncertainty should be included in its value;
- the propeller efficiency is estimated with the automatic calculator ([31]) already employed in 5.1, which reports an error in the efficiency of $\pm 5\%$.

Therefore, the error on the C_D measure will probably be higher at low airspeeds, since the third order CAS at the denominator of the C_D (Eq. 9.23) should mitigate the numerator's error.

Roskam ([24]) illustrates a method to predict drag coefficients C_{D0} and K. The former is found with the empirical formula:

$$C_{D0} = C_f \frac{S_{wet}}{S} = 0.0431 \tag{9.14}$$

where C_f is the skin friction coefficient, which, for airplanes similar to the G70, is 0.01; S_{wet} is the wet surface of the aircraft and it is found with the CAD model. K is found by analogy from the Oswald's coefficient of similar airplanes: Cessna 150 has $e = 0.77$, leading to:

$$K = \frac{1}{\pi \lambda e} = 0.0530 \tag{9.15}$$

9.2.2 Test objectives

Drag polar estimate is of paramount importance for a double reason: firstly, the manufacturer has an immediate tool to understand the aircraft performance with the purpose to evaluate potential improvements to the overall efficiency of the airplane. Secondly, drag polar is useful to the definition of a six degree of freedom model of the aircraft for further studies.

9.2.3 Test execution

Drag polar from glides

During the fligth test campaign many glides tests have been executed:

- Flight 02.1405, aircraft configuration 1, 1000 ft, CR flap;
- Flight 02.0206, aircraft configuration 2, 1100 ft, CR flap;
- Flight 01.1006, aircraft configuration 3, 1800 ft, CR flap;
- Flight 01.1507, aircraft configuration 3, 1200 and 2100 ft, CR flap;
- Flight 07.1006, aircraft configuration 3, 1800 ft, TO flap;
- Flight 01.1706, aircraft configuration 3, 1300 ft, TO flap;

Drag polar estimate requires the same aircraft configuration, therefore only glides with the 3rd aircraft configuration and CR flaps have been analysed for this test.

Sawtooth glides test consists in a series of glide segments, flown through the same altitude gap with idle power. Every descent has a different sirspeed, in order to sweep a sufficiently broad range of velocities. The detailed procedure is the following:

1. set flaps in the desired configuration;
2. trim the aircraft sufficiently above the entry altitude;
3. set power to idle;
4. start gliding and time the glide, careful to maintain the same airspeed throughout the whole descent;
5. when reached the lower altitude, set power as necessary and repeat the test with a different airspeed.

Vertical speed V_d is found as the ratio between the pressure altitude gap and the recorded time; V_{TAS} during the descent is known, since IAS has to be maintained constant and anemometer calibration, as well as pressure altitude, are available. Descent angle is defined as:

$$\gamma_d = \arcsin\left(\frac{V_d}{V_{TAS}}\right) \tag{9.16}$$

Lift and drag in a steady state glide are the only forces balancing the weight, namely:

$$L = W_T \cos\gamma_d \tag{9.17}$$
$$D = W_T \sin\gamma_d \tag{9.18}$$

Lift and drag coefficients are now easily calculated as:

$$C_L = \frac{2W_T \cos\gamma_d}{\rho_0 S V_{CAS}^2} \tag{9.19}$$
$$C_D = \frac{2W_T \sin\gamma_d}{\rho_0 S V_{CAS}^2} \tag{9.20}$$

Drag polar from trim test

Drag polar from trim test is a *speed power test*, based on the fact that for level, unaccelerated flight thrust is equal to drag. Therefore, if thrust, or power, at a given test point is known, drag at that speed may also be determined. Test procedure and test points are the same used for trimmability test and stick-fixed neutral point estimation, therefore the reader is asked to refer to 6.3.3 for further information.

To sum up, all the flights, both trim and glide test, whose results contributes to drag polar estimation are:

- Flight 01.1006 (1800 ft, glide);
- Flight 01.1507 (1200 ft, glide);
- Flight 01.1507 (2100 ft, glide);
- Flight 03.1706 (trim);
- Flight 04.1706 (trim);
- Flight 05.1706 (trim).

For steady, level, unaccelerated flight:

$$P_a = P_r \tag{9.21}$$

where:

$$P_a = P_b \eta_p \tag{9.22a}$$

$$P_r = \frac{1}{2}\rho V_{TAS}^3 S C_D = \frac{1}{2}\rho_0 V_{CAS}^3 \sqrt{\frac{1}{\sigma}} S C_D \tag{9.22b}$$

P_b is extrapolated from the engine manual ([7]), known RPM, MP and test altitude. Propeller efficiency is found from [31], whose principle and limitations have been described in 5.1.
Drag coefficient is immediately known:

$$C_D = \frac{P_b \eta_p \sqrt{\sigma}}{1/2 \rho_0 V_{CAS}^3 S} \tag{9.23}$$

Lift coefficient is:

$$C_L = \frac{2W_T}{\rho_0 S V_{CAS}^2} \tag{9.24}$$

9.2.4 Data uncertainty

Trim test data error has been estimated by evaluating the error of the two terms which most contribute to it, namely the value of available power and propeller efficiency. The latter's estimation accuracy is provided with the calculator ([31]) and is rated as $\pm 5\%$. Engine power accuracy has to be estimated from the engine chart of [7]: its resolution is 5 kW, or 6.7 HP, which makes it reasonable to suppose an accuracy of 2.5 kW, or 3.4 HP, in the available power. In order to evaluate how random experimental errors of the variables can be propagated in the final C_D result, the Root of the Sum of the Squares (RSS) approach have been followed ([30] and [26]). The uncertainty ΔC_D of the C_D function (9.23) depends on the uncertainties of P_b and η_p, namely ΔP_b and $\Delta \eta_p$:

$$\Delta C_D = \sqrt{\left(\frac{\partial C_D}{\partial P_b}\Delta P_b\right)^2 + \left(\frac{\partial C_D}{\partial \eta_p}\Delta \eta_p\right)^2} \tag{9.25}$$

Two hypothesis are at the base of the RSS method:

- the uncertainties must be independent, namely no correlation exists between them;

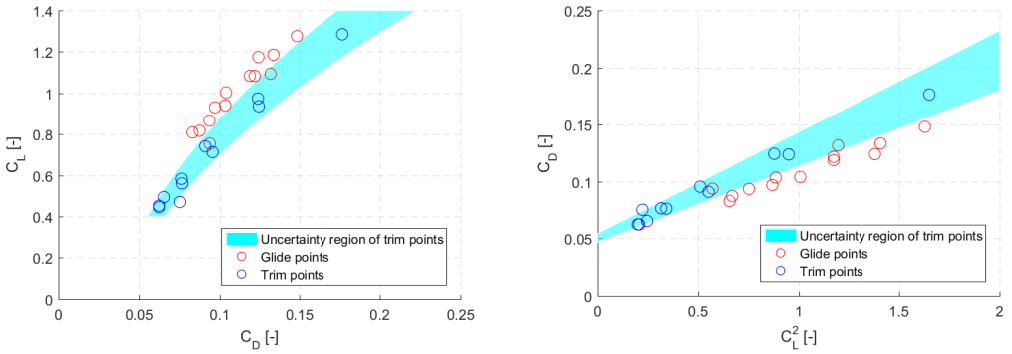

(a) (b)

Figure 9.4: Uncertainty area of the trim test points with a second order fitting (9.4a) and a linear one (9.4b).

- positive and negative deviations have the same likelihood to happen.

There are no reasons to presume that the second hypothesis is not verified, while the first one is harder to accept: as a matter of fact, propeller efficiency calculation accounts the engine power as a variable and the software does not provide any indication about the model method implemented in it; moreover, the software developer was not helpful when consulted by e-mail. Consequently, a trial-and-error method has been tried and the observed result leads to the conclusion that variations of ± 2.5 kW in the engine power provided to the calculator do not vary the efficiency value of more than 1%. This variation of efficiency with engine power cannot be accounted in the RSS since it would make it un-applicable, because it does not verify the second hypothesis, but it is assumed negligible and it will not take part in the analysis. It is worthy to underline how the RSS is a linearization of the output function with respect to each input experimental data; therefore its principle is to account all the possible error contributions in their most likely occurrence, which is not the maximum error, or worst case.

The result is shown in Fig. 9.4: the error is, as expected, lower at higher airspeeds and, consequently, low C_L trim data are regarded as more reliable. The reason of the greater error at lower airspeeds is due to the third order exponent CAS at the denominator: higher airspeeds contribute to reduce the overall error.

9.2.5 Test results

Three different data sets have been considered for drag polar approximation:

- only glide points;
- only trim points;
- all glide and low C_L trim points. The C_L threshold has been defined as $C_L = 0.6$, which corresponds, in the test conditions, at 140 km/h of CAS.

Drag polar has been fitted according to a second order function between the C_L and C_D test points and with a linear fitting between C_L^2 and C_D. The first is in the form:

$$C_{D,par} = C_{D0,par} + HC_L + K_{par}C_L^2 \tag{9.26}$$

which can be rewritten as:

$$C_{D,par} = C_{D,min} + K(C_L - C_{L_{C_{D,min}}})^2 \tag{9.27}$$

The coefficients $C_{D,min}$ and $C_{L_{C_{D,min}}}$ are the polar vertex coordinates, namely the point where drag coefficient is minimum.
The latter is a further simplification, which neglects the first order term:

$$C_{D,lin} = C_{D0} + KC_L^2 \tag{9.28}$$

whose coefficients C_{D0} and K are generally different with respect to $C_{D0,par}$ and K_{par}.

Fig. 9.5 represents the second order drag polar for all the enumerated sets of points, while Fig. 9.6 plots the linear polar C_D versus C_L^2; the resultant coefficients are reported in Tab. 9.2.

Table 9.2: Drag coefficients as calculated from the aircraft experimental polar.

Points	$C_{D,min}$ [-]	$C_{L_{C_{D,min}}}$ [-]	K [-]	C_{D0} [-]	e [-]
Glides-only	0.0766	0.4645	0.0591	0.0501	0.7509
Trim-only	0.0276	-0.3851	0.0778	0.0508	0.5455
Glides and low C_L trim	0.0626	0.2004	0.0565	0.0530	0.7340

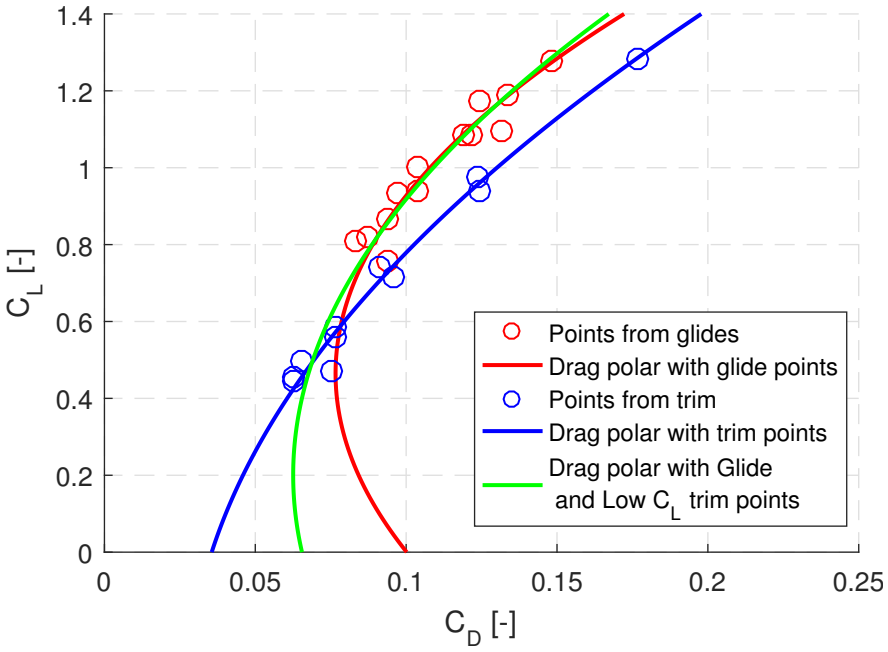

Figure 9.5: Experimentally drawn drag polar of the aircraft.

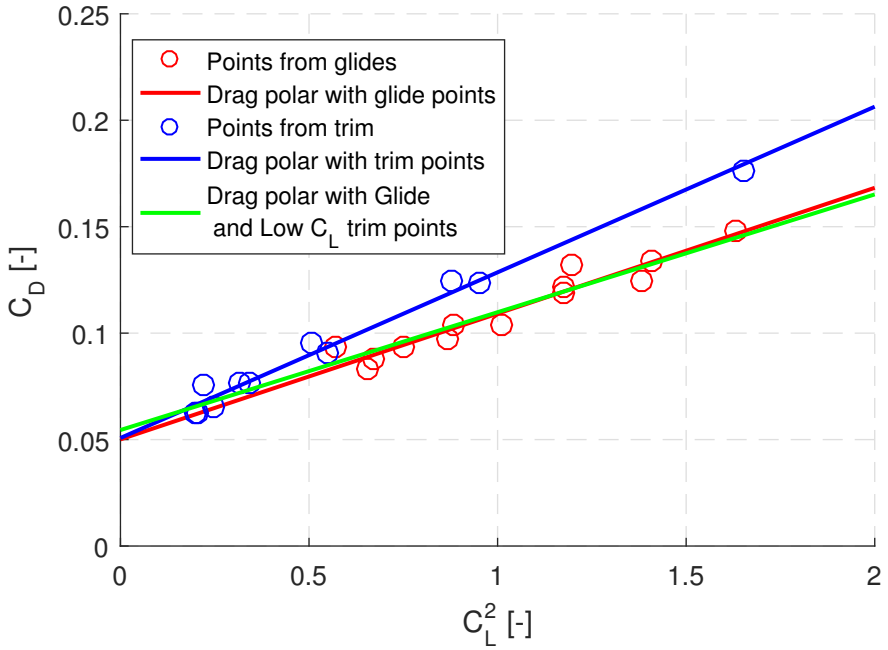

Figure 9.6: Experimentally drawn drag polar of the aircraft in the form $C_D = C_{D0} + KC_L^2$.

9.2.6 Conclusions

All the high C_L points stand on the right of the glide ones: the C_D of the trim points is always higher for the same values of C_L, which enforces the doubts that a systematic error is present. Probably the online calculator of propeller efficiency ([31]) is too optimistic and its high value provides a higher value of C_D, as it is clear from 9.23. As a matter of fact, the propeller mounted on the G70 is optimised for high speed cruise, which makes the efficiency peak located at higher speed, hence lower C_L; for this reason, it is justified to think that the calculator overrates the efficiency at low speed. This last consideration, coupled with the higher grade of uncertainties highlighted in 9.4, makes the test points executed at low speed not reliable for drag polar approximation, as long as a better method for propeller efficiency calculation is found.

The sets of points made by only glides and glides plus low C_L trim points have very similar results in terms of C_{D0} and K (and consequently of e); their main difference is in the minimum drag point. The most reliable set of points is the one made of glide and low C_L trim points, because they cover a wider range of velocities with an acceptable accuracy, as demonstrated.

C_{D0} and K prediction from Roskam is good for the latter, while the former has been badly predicted: zero lift drag coefficient of the G70 is way higher than the one of general aviation airplanes with similar geometry. Nevertheless, C_{D0} from drag polar is regarded as reliable, because it is comparable to the values obtained by other works on *Groppo* airplanes ([11] and [21]).

Chapter 10

Bootstrap approach to predict flight performance

The Bootstrap approach for flight performance evaluation is a procedure published by J. T. Lowry ([16], [17]), which aims at estimating flight performance of a fixed-pitch propeller airplane for every combination of altitude and weight. The parameters influencing the solution have to be determined with a single sawtooth test, both for climb and glide phase; in particular, they are speed of fast and steepest climb and maximum speed in level flight (V_{FC}, V_{SC} and V_M), speed of maximum efficiency during climb (V_{BG}) and its correspondent angle $\gamma_{d,BG}$.

The Bootstrap approach is based on four assumptions about aircraft performance, namely:

- Parabolic aircraft polar;
- Linear propeller polar;
- Shaft torque not dependent on flight speed;
- Torque decreasing as a function of the only altitude.

All these assumptions will be employed in the following section to mathematically derive the performance formulas with Bootstrap approach, which is mainly based on the analytical dissertation of [29].

10.1 Bootstrap approach performance equations

Assuming a parabolic polar of the entire airplane in the form

$$C_D = C_{D0} + KC_L^2 \tag{10.1}$$

it is possible to write drag:

$$\begin{aligned} D &= \frac{1}{2}\rho V^2 S C_D = \\ &= \frac{1}{2}\rho V^2 S (C_{D0} + K C_L^2) = \\ &= \frac{1}{2}\rho V^2 S C_{D0} + \frac{1}{2}\rho V^2 S K \underbrace{\left(\frac{2W}{\rho S V^2}\right)^2}_{C_L^2} = \\ &= W\left(C_{D0}\frac{\rho S}{2W}V^2 + K\frac{2W}{\rho S}\frac{1}{V^2}\right) \end{aligned} \tag{10.2}$$

and requested power:

$$\begin{aligned} P_r &= DV = \\ &= W\left(C_{D0}\frac{\rho S}{2W}V^3 + K\frac{2W}{\rho S}\frac{1}{V}\right) \end{aligned} \tag{10.3}$$

Aircraft performance can be summarized in six V-speeds, namely:

- Maximum and minimum speed in level flight V_M and V_m;
- Steepest climb V_{SC} and fastest climb V_{FC} speed;
- Best glide V_{BG} and minimum descent V_{MD} speed (respectively speed for maximum range and maximum endurance during glide).

The V-speeds are found as the solution of the following equations:

$$P_a = P_r \quad \rightarrow \quad V_m, V_M \tag{10.4a}$$

$$\frac{\partial}{\partial V}T = \frac{\partial}{\partial V}D \quad \rightarrow \quad V_{SC} \tag{10.4b}$$

$$\frac{\partial}{\partial V}P_a = \frac{\partial}{\partial V}P_r \quad \rightarrow \quad V_{FC} \tag{10.4c}$$

$$\frac{\partial}{\partial V}D = 0 \quad \rightarrow \quad V_{BG} \tag{10.4d}$$

$$\frac{\partial}{\partial V}P_r = 0 \quad \rightarrow \quad V_{MD} \tag{10.4e}$$

Propeller polar is the function which links C_T/J^2 and C_P/J^2, where C_T and C_P are the thrust and power coefficients and J is the advance ratio, defined as

$$J = \frac{V}{N D_p} \tag{10.5}$$

Assuming a linear propeller polar means:

$$C_T/J^2 = mC_P/J^2 + b \tag{10.6}$$

hence:

$$C_T = mC_P + bJ^2 \tag{10.7}$$

Propeller efficiency is defined as the ratio between available power P_a and shaft power P_b:

$$\eta_p = \frac{P_a}{P_b} \tag{10.8}$$

which leads to:

$$\eta_p = \frac{TV}{P_b} = \frac{\rho N^2 D_p^4 C_T}{\rho N^3 D_p^5 C_P} J N D_p = \frac{C_T}{C_P} J \tag{10.9}$$

By substituting Eqq. 10.5, 10.6 in Eq. 10.9, the result is:

$$\eta_p = \frac{m}{N D_p} V + b \frac{\rho D_p^2}{P_b} V^3 \tag{10.10}$$

which, compared to Eq. 10.8, leads to:

$$P_a = T_0 V + T_2 V^3 \tag{10.11}$$

and, consequently:

$$T = \frac{P_a}{V} = T_0 + T_2 V^2 \tag{10.12}$$

with the coefficients T_0 and T_2 defined as:

$$T_0 := \frac{m P_b}{N D_p} = \frac{2\pi m}{D_p} C \tag{10.13a}$$

$$T_2 := b \rho D_p^2 \tag{10.13b}$$

Eq. 10.13a accounts the definition of shaft torque, which is:

$$C := \frac{P_b}{2\pi N} \tag{10.14}$$

For sake of readability the following term is employed:

$$A := \frac{2W}{\rho S} \tag{10.15}$$

Maximum and minimum speed in level flight

The equation which has to be solved, according to Eq. 10.4a is:

$$\frac{C_{D0}}{A^2}V^4 - \frac{P_a(v)}{WA}V + K = 0 \tag{10.16}$$

$$\left(C_{D0} - \frac{T_2 A}{W}\right)\frac{1}{A^2}V^4 - \frac{T_0}{WA}V^2 + K = 0 \tag{10.17}$$

The last equation leads to the solution:

$$V = \sqrt{\frac{\tau_0 A}{2C^*_{D0}}\left(1 \pm \sqrt{1 - \frac{4C^*_{D0}K}{\tau_0^2}}\right)} \tag{10.18}$$

Where other two coefficients have been defined:

$$C^*_{D0} = C_{D0} - \frac{T_2 A}{W} = C_{D0} - 2b\frac{D_p^2}{S} \tag{10.19a}$$

$$\tau_0 = \frac{T_0}{W} = \frac{2\pi m C}{D_p W} \tag{10.19b}$$

Speed of steepest climb V_{SC}

According to Eq. 10.4b, the equation to solve is:

$$\frac{C_{D0}}{A^2}V^4 - \frac{1}{2WA}\frac{\partial T}{\partial V}V^3 - K = 0 \tag{10.20}$$

$$\frac{C^*_{D0}}{A^2}V^4 - K = 0 \tag{10.21}$$

The last equation offers the solution:

$$V = \sqrt{A}\sqrt{\frac{K}{C^*_{D0}}} \tag{10.22}$$

Speed of fastest climb V_{FC}

According to Eq. 10.4c, the equation to solve is:

$$\frac{3C_{D0}}{A^2}V^4 - \frac{1}{WA}\frac{\partial P_a}{\partial V}V^2 - K = 0 \tag{10.23}$$

$$\frac{3C^*_{D0}}{A^2}V^4 - \frac{\tau_0}{A}V^2 - K = 0 \tag{10.24}$$

Hence:

$$V = \sqrt{\frac{\tau_0 A}{6C^*_{D0}}\left(1 \pm \sqrt{1 - \frac{12C^*_{D0}K}{\tau_0^2}}\right)} \tag{10.25}$$

Speed of maximum range during glide V_{BG}

From Eq. 10.4d, the derivative of drag with respect to speed V is:

$$\frac{\partial}{\partial V}\left(\frac{1}{2}\rho V^2 S C_{D0} + \frac{2KW^2}{\rho S V^2}\right) = 0 \tag{10.26}$$

$$\rho V S C_{D0} - 2\frac{2KW^2}{\rho S V^3} = 0 \tag{10.27}$$

hence:

$$V = \sqrt{A}\sqrt[4]{\frac{K}{C_{D0}}} \tag{10.28}$$

Speed of maximum endurance during glide V_{MD}

From Eq. 10.4e, the derivative of requested power with respect to speed V is:

$$\frac{\partial}{\partial V}\left(\frac{1}{2}\rho V^3 S C_{D0} + \frac{2KW^2}{\rho S V}\right) = 0 \tag{10.29}$$

$$\frac{3}{2}\rho V^2 S C_{D0} - \frac{2KW^2}{\rho S V^2} = 0 \tag{10.30}$$

hence:

$$V = \sqrt{A}\sqrt[4]{\frac{K}{3C_{D0}}} \tag{10.31}$$

Now it is time to use the last hypotesis, that is the one which states that torque is a function of the only altitude, in particular:

$$C = \Phi(\sigma) C_0 \tag{10.32}$$

where $\sigma = \frac{\rho}{\rho_0}$ and $\Phi(\sigma)$ is the *power drop-off factor*, defined as:

$$\Phi(\sigma) = \frac{\sigma - c_e}{1 - c_e} \tag{10.33}$$

with $c_e \in [0.11 \div 0.15]$, which is a parameter characteristic of the engine ([16]). By means of this last approximation:

$$T_0 = \frac{2\pi m}{D_p}\Phi(\sigma) C_0 = \Phi(\sigma) T_B \tag{10.34}$$

with $T_B = \dfrac{2\pi m C_0}{D_p}$.

Now all the V speeds equations with the Bootstrap approach can be listed:

$$V_M(h,W) = \sqrt{\frac{\Phi(\sigma)}{\sigma}\frac{\tau_B A_B}{2C^*_{D0}}\left(1+\sqrt{1-\left(\frac{w}{\Phi(\sigma)}z^*_B\right)^2}\right)} \tag{10.35}$$

$$V_m(h,W) = \sqrt{\frac{\Phi(\sigma)}{\sigma}\frac{\tau_B A_B}{2C^*_{D0}}\left(1-\sqrt{1-\left(\frac{w}{\Phi(\sigma)}z^*_B\right)^2}\right)} \tag{10.36}$$

$$V_{SC}(h,W) = \sqrt{\frac{w}{\sigma}A_B\sqrt{\frac{K}{C^*_{D0}}}} \tag{10.37}$$

$$V_{FC}(h,W) = \sqrt{\frac{\Phi(\sigma)}{\sigma}\frac{\tau_B A_B}{6C^*_{D0}}\left(1+\sqrt{1+3\left(\frac{w}{\Phi(\sigma)}z^*_B\right)^2}\right)} \tag{10.38}$$

$$V_{BG}(h,W) = \sqrt{\frac{w}{\sigma}A_B\sqrt{\frac{K}{C_{D0}}}} \tag{10.39}$$

$$V_{MD}(h,W) = \sqrt{\frac{w}{\sigma}A_B\sqrt{\frac{K}{3C_{D0}}}} \tag{10.40}$$

The following parameters have been defined:

$$w = \frac{W}{W_S} \tag{10.41}$$

$$A_B = \frac{2W_S}{\rho_0 S} \tag{10.42}$$

$$\tau_B = \frac{T_B}{W_T} \tag{10.43}$$

$$z^*_B = \frac{2\sqrt{C^*_{D0}K}}{\tau_B} \tag{10.44}$$

All the equations are function of weight and density (or altitude), along with other parameters not depending on the previous two.

Additionally, other performance indicators will be summarized: some of them have already been defined in this section and are listed here for clarity; some others will be defined *ex novo*.

Thrust and drag

$$T(h,V) = \frac{2\pi m C(h)}{D_p} + bD_p^2 \rho_0 \sigma(h) V^2 \tag{10.45}$$

$$D(h,V,W) = \frac{1}{2}\rho_0 \sigma(h) S C_{D0} V^2 + \frac{2KW^2}{\rho_0 \sigma(h) S}\frac{1}{V^2} \tag{10.46}$$

Available, requested and excess power

$$\begin{aligned} P_a(h,V) &= T(h,V)V = \\ &= \frac{2\pi m C(h)}{D_p} V + bD_p^2 \rho_0 \sigma(h) V^3 \end{aligned} \tag{10.47}$$

$$\begin{aligned} P_r(h,V,W) &= D(h,V,W)V = \\ &= \frac{1}{2}\rho_0 \sigma(h) S C_{D0} V^3 + \frac{2KW^2}{\rho_0 \sigma(h) S}\frac{1}{V} \end{aligned} \tag{10.48}$$

$$\begin{aligned} P_{xs}(h,V,W) &= Pa(h,V) - Pr(h,V,W) = \\ &= \left(bD_p^2 \rho_0 \sigma(h) - \frac{1}{2}\rho_0 \sigma(h) S C_{D0} \right) V^3 + \frac{2\pi m C(h)}{D_p} V - \frac{2KW^2}{\rho_0 \sigma(h) S}\frac{1}{V} \end{aligned} \tag{10.49}$$

Rate of climb and rate of sink

$$V_v(h,V,W) = \frac{P_{xs}(h,V,W)}{W} \tag{10.50}$$

The rate of sink is similar to the ROC, but with all the terms regarding the engine power, that is the power available, equal to zero:

$$V_d(h,V,W) = \frac{-P_r(h,V,W)}{W} \tag{10.51}$$

Climb and glide angles

$$\gamma(h,V,W) = \arccos\left(\frac{P_{xs}(h,V,W)}{WV} \right) \tag{10.52}$$

Best angle of climb is found by substituting V_{SC}:

$$\gamma_{SC}(h,V_{SC},W) = \arccos\left(\frac{P_{xs}(h,V_{SC},W)}{WV_{SC}} \right) \tag{10.53}$$

$$\gamma_d(h, V, W) = \arccos\left(\frac{-P_r(h, V, W)}{WV}\right) \tag{10.54}$$

Best angle of glide is found by substituting V_{BG}:

$$\gamma_{d,BG}(h, V_{BG}, W) = \arccos\left(\frac{-P_r(h, V_{BG}, W)}{WV_{BG}}\right) \tag{10.55}$$

10.2 Experimental procedure

The parameters needed for Bootstrap performance prediction are the coefficients of the parabolic polar of the aircraft and of the linear propeller polar, in particular:

- C_{D0},
- K,
- m,
- b.

In order to acquire these parameters, four data have to be obtained with flight test:

- $\gamma_{d,BG}$,
- V_{BG},
- two between:
  - V_{SC},
  - V_{FC},
  - V_M.

In the following dissertation these parameters will be referred as 'V-speeds', although $\gamma_{d,BG}$ is not a speed.

In other words, the Bootstrap approach for aircraft performance works as follows:

- the method receives as input the V-speeds obtained with flight test;
- the V-speeds are used to determine the coefficients of the parabolic drag polar and of the linear propeller polar;
- with the coefficients of the two polars, it is possible to find out the V-speeds at any configuration of weight and altitude, along with all the other performance indicators.

Sawtooth glide test

Sawtooth glide test is employed to obtain $\gamma_{d,BG}$ and V_{BG}, which allow to calculate the aircraft drag polar coefficients C_{D0} and K. V_{BG} is found as the intersection of the glide 2nd order approximation with the tangent line from the origin, after the test executed as detailed in 9.2.3. Once this speed is known, the procedure to find $\gamma_{d,BG}$ is straightforward: the angle of best glide is found as:

$$\gamma_{d,BG} = \arcsin\left(\frac{\Delta h}{V_{BG}\Delta t}\right) = \arcsin\left(\frac{V_{d,BG}}{V_{BG}}\right) \tag{10.56}$$

where the Rate of Descent $V_{d,BG}$ is found from the 2nd order approximation. The parabolic drag polar coefficients are found:

$$C_{D0} = \frac{1}{2}\frac{w}{\sigma}\frac{A_B}{V_{BG}^2}\sin\gamma_{d,BG} \tag{10.57}$$

$$K = \frac{1}{2}\frac{\sigma}{w}\frac{V_{BG}^2}{A_B}\frac{\tan^2\gamma_{d,BG}}{\sin\gamma_{d,BG}} \tag{10.58}$$

Sawtooth climb test

Sawtooth climb test, whose procedure is detailed in 5.5.3, provides V_{SC}, V_{FC} and V_M, which is obtained with a null rate of climb test point in order to provide the point to close the 2nd order approximation. Firstly, C_{D0}^* is found:

$$C_{D0}^* = K\left(\frac{w}{\sigma}\right)^2\left(\frac{A_B}{V_{SC}^2}\right)^2 \tag{10.59}$$

The propeller polar coefficient b is found by rearranging Eq. 10.19a:

$$b = \frac{S}{2D_p^2}(C_{D0} - C_{D0}^*) \tag{10.60}$$

Secondly, τ_0 is obtained in two equivalent ways, by means of V_{FC} or V_M, namely:

$$\tau_0 = 3C_{D0}^*\frac{\sigma}{w}\frac{V_{FC}^2}{A_B} - K\frac{w}{\sigma}\frac{A_B}{V_{FC}^2} \tag{10.61}$$

or

$$\tau_0 = C_{D0}^*\frac{\sigma}{w}\frac{V_M^2}{A_B} + K\frac{w}{\sigma}\frac{A_B}{V_M^2} \tag{10.62}$$

Once τ_0 has been obtained, m comes from Eq. 10.19b, conveniently rearranged:

$$m = \frac{D_p W}{2\pi C}\tau_0 \tag{10.63}$$

where C is found from Eq. 10.32 with the conditions of the test.

10.3 G70 Bootstrap approach data set

Once the Bootstrap procedure has been implemented, some suitable experimental data are needed. Along the whole flight campaign, a great number of sawtooth climbs and glides tests have been performed, as listed in 5.5.4 for climb tests and in 9.2.3 for glide tests. The problems related to this great amount of experimental data are:

- some tests have been performed with different configurations in terms of weight and altitude;
- not all the sawtooth glides tests provided data can be approximated with a 2nd order curve, which leads to the impossibility to determine the V-speeds for that test;
- some tests provided bad results in terms of data scattering, which means that the test points, even if the 2nd order approximation is possible, are too scattered and they might lead to misleading conclusions.

The best flights in terms of climb and glide data quality are, respectively, flight 06.1006 and 01.1006, which, however, have been performed with different weight and altitude configurations. This last problem is overcome if a glance is given at the Bootstrap polar coefficient formulas: drag polar ones are found with data coming from glide tests, namely $\gamma_{d,BG}$ and V_{BG}, while the propeller coefficients request the data from climb tests. Hence, it is possible to use two sawtooth tests performed with different configuration to obtain all the needed coefficients, provided that two different sets of weight and density ratio are employed, firstly for the drag coefficients, then for the propeller ones.

It is worth it to underline how the input data of the Bootstrap approach are the raw ones, without any reduction of weight and altitude; otherwise, the meaning of the Bootstrap approach itself, starting from the V-speeds at a given configuration of weight and altitude and leading to general formulas valid for all the configurations, would be lost.

Test results are summarized in Tab. 10.1.

10.4 Bootstrap approach data sensitivity and choice

Since it is an approach based on exclusive experimental data, it is possible that the measure errors of the input parameters strongly influence the output.

Table 10.1: Bootstrap approach experimental data.

Flight	W [kg]	h [ft]	V_{SC} [km/h]	V_{FC} [km/h]	V_M [km/h]	V_{BG} [km/h]	$\gamma_{d,BG}$ [deg]
06.1006	525	1600	100	117	178	-	-
01.1006	570	1800	-	-	-	108	5.99

Bootstrap data are acquired in different ways:

- V_{BG} and $\gamma_{d,BG}$ come from sawtooth glide test, after least-squares second order approximation of experimental data, namely rate of sink versus TAS;
- V_{SC} and V_{FC} come from sawtooth climb test, after least-squares second order approximation of experimental data, namely rate of climb versus TAS;
- V_M is a direct measure of the maximum level flight speed at the altitude of the sawtooth climb test.

In this section all the possible alternatives of data sets for Bootstrap approach will be listed: for each of them, an uncertainty propagation analysis is performed, with additional consideration on data reliability and quality. Possible data combination are:

1. V_{BG}, $V_{d,BG}$, V_{SC}, V_{FC};
2. V_{BG}, $V_{d,BG}$, V_{SC}, V_M;
3. V_{BG}, $V_{d,BG}$, V_M, V_{FC}.

The latter is obtained by solving the system of Eqq. 10.61 and 10.62 to find out C^*_{D0} and τ_0. Since $\gamma_{d,BG}$ is function of V_{BG} and $V_{d,BG}$, the uncertainty analysis will account the latter as input instead of the best glide angle. Tab. 10.2 shows all the output dependences with respect to input data. Inputs from glide are the same for every data combination and they calculate the drag coefficients C_{D0} and K; the differences between the three data sets is in the ways to calculate propeller polar coefficients m and b.

Uncertainty propagation analysis has been performed with RSS, which has already been discussed in 9.2.4. Input data have been perturbed with a variable perturbation, the same for all the input, from 0 to 3%, in order to immediately visualize the weight of each input's error in the overall method

Table 10.2: Bootstrap input possible combinations.

	C_{D0}	K	m	b
1	V_{BG}, $V_{d,BG}$	V_{BG}, $V_{d,BG}$	V_{BG}, $V_{d,BG}$, V_{SC}, V_{FC}	V_{BG}, $V_{d,BG}$, V_{SC}
2	V_{BG}, $V_{d,BG}$	V_{BG}, $V_{d,BG}$	V_{BG}, $V_{d,BG}$, V_M, V_{FC}	V_{BG}, $V_{d,BG}$, V_{SC}
3	V_{BG}, $V_{d,BG}$	V_{BG}, $V_{d,BG}$	V_{BG}, $V_{d,BG}$, V_M, V_{FC}	V_{BG}, $V_{d,BG}$, V_M, V_{FC}

error. Since V_M is a direct measure coming from the anemometer, while all the other input are indirect measures from least-squares approximation, its uncertainty is definitely lower than the one of the other inputs; therefore, the following analysis will account maximum speed uncertainty as null. The general output error expression will account all the input uncertainties, according to the dependencies reported in Tab. 10.2:

$$\Delta O_i = \sqrt{\sum_{i=1}^{N} \left(\frac{\partial(O)}{\partial(I)} \Delta I_i \right)^2} \tag{10.64}$$

10.4.1 Input combination 1: V_{BG}, $V_{d,BG}$, V_{SC} and V_{FC}

Input combination 1 employs both the V-speeds obtained from the second order least-squares approximation of the sawtooth climb data. The RSS result shows a dramatic error transmission from input to output: in fact, with a 3% perturbation of all the input V-speeds, the resulting b coefficient has an error of 140 %, while m uncertainty remains under the 20 %. This fact is not surprising after a look to b equation (Eq. 10.60), which receives the strong influence of V_{SC} as a 4th grade exponent from C^*_{D0} (Eq. 10.59); also the glide speeds greatly influence b, although with a lower magnitude. m coefficient is way less sensitive to input variations and the strongest influence is given just by V_{SC}; V_{FC}, V_{BG} and $V_{d,BG}$ have a very mild influence on the overall error.

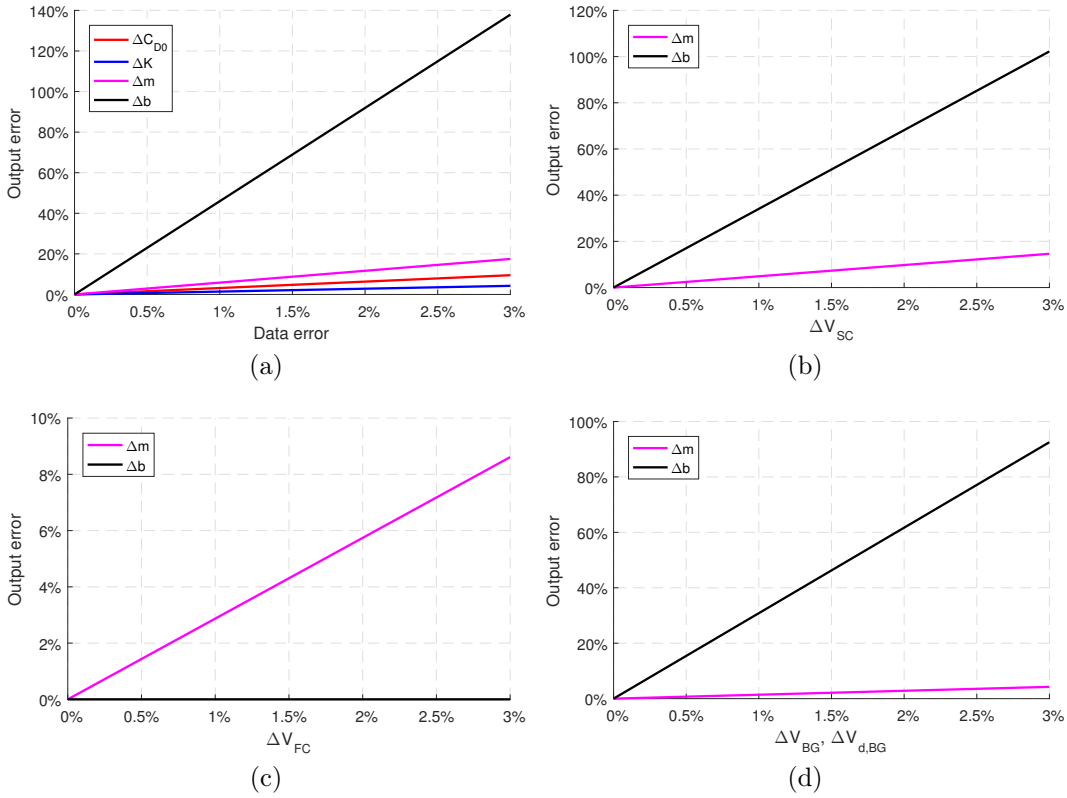

Figure 10.1: Bootstrap outputs sensitivity with perturbations of all the inputs (10.1a), and with single data perturbation (V_{SC} in 10.1b, V_{FC} in 10.1c, V_{BG} and $V_{d,BG}$ in 10.1d).

Another aspect which must be accounted for the data set choice is the higher possibility that V_{SC} calculation is influenced by errors in the climb test

points: it has been observed how, given perturbation of ±5% to the sawtooth climb points, both in the direction of V_v (Y-axis) and V_{TAS} (X-axis), the measure of V_{SC} floats more than V_{FC}. The results of this observation, which has been performed by assuming exact the measure of V_M, are reported in 10.3.

Table 10.3: Bootstrap input possible combinations.

	$\Delta V_v = +5\%$	$\Delta V_v = -5\%$
$\Delta V_{TAS} = +5\%$	$V_{SC} = 108.0$ km/h $V_{FC} = 121.6$ km/h	$V_{SC} = 108.0$ km/h $V_{FC} = 121.6$ km/h
$\Delta V_{TAS} = -5\%$	$V_{SC} = 92.0$ km/h $V_{FC} = 112.7$ km/h	$V_{SC} = 92.0$ km/h $V_{FC} = 112.7$ km/h

To sum up, the first data set is strongly influenced by V_{SC}, which is the input which most feels the effect of the test quality.

10.4.2 Input combination 2: V_{BG}, $V_{d,BG}$, V_M and V_{SC}

The second data set shows a slightly lower sensitivity to the input parameters, since V_{MAX} is a direct measure and its error can be safely regarded as null, with a careful observation of the anemometer during the test point. Fig. 10.2 shows how the error affecting m drops to the 12% for a 3% perturbation of the input data. Most of the uncertainty is due to V_{SC}, which dramatically keeps on influencing b, as already shown for the first data set.

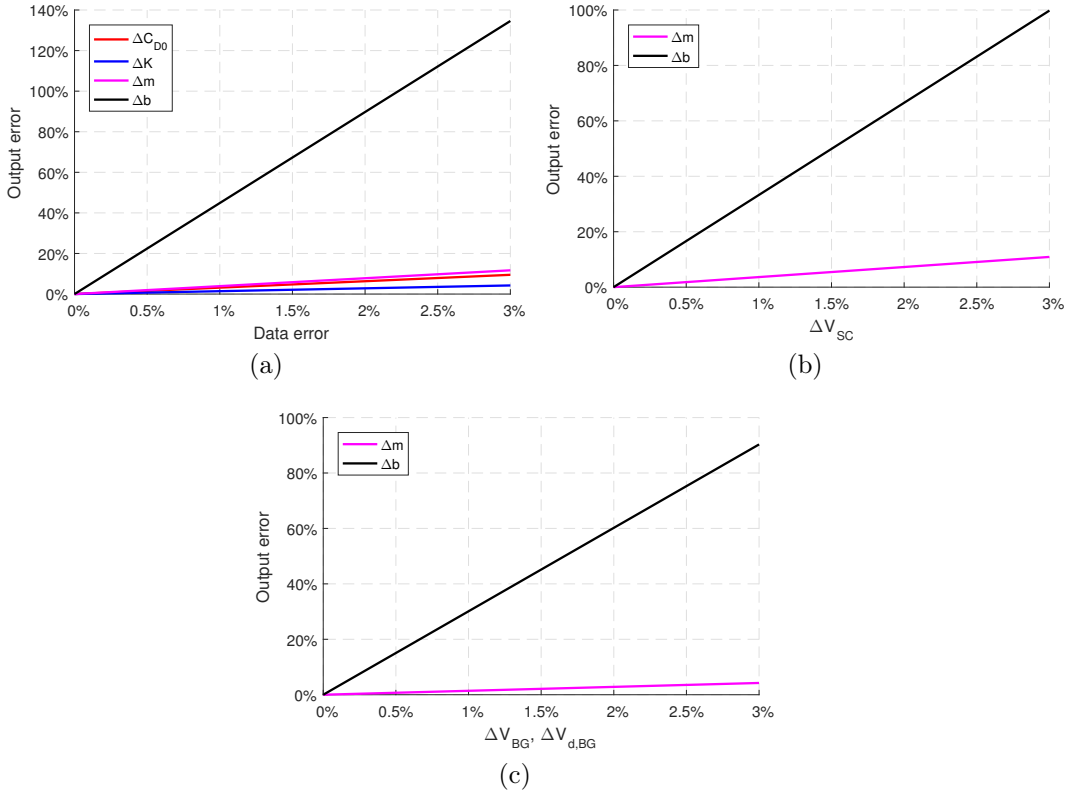

Figure 10.2: Bootstrap outputs sensitivity with perturbations of all the inputs (10.2a), and with single data perturbation (V_{SC} in 10.2b, V_{BG} and $V_{d,BG}$ in 10.2c).

This data set would be perfect if a direct measure of the climb angle γ were available from an appropriate instrumentation for each test point, as a function of flight speed. In fact, a suitable approximation among all the point would allow to find out the value of speed for the steepest climb, namely V_{SC}. With a direct measure of the speed of steepest climb, added to the direct measure of V_{MAX}, the error of the result would be minimized.

10.4.3 Input combination 3: V_{BG}, $V_{d,BG}$, V_M and V_{FC}

This last approach aims at deleting the contribute of V_{SC} from the Bootstrap set of data. It is done by rearranging Eqq. 10.61 and 10.62, in order to find out a new formulation for C^*_{D0} and τ_0. In detail, the linear system is in the form:

$$\begin{bmatrix} 1 & -3C^*_{D0}\frac{\sigma}{w}\frac{V^2_{FC}}{A_B} \\ 1 & -C^*_{D0}\frac{\sigma}{w}\frac{V^2_M}{A_B} \end{bmatrix} \begin{bmatrix} \tau_{0,new} \\ C^*_{D0,new} \end{bmatrix} = \begin{bmatrix} -K\frac{w}{\sigma}\frac{A_B}{V^2_{FC}} \\ K\frac{w}{\sigma}\frac{A_B}{V^2_M} \end{bmatrix} \tag{10.65}$$

which leads to:

$$C^*_{D0,new} = -\left(\frac{w}{\sigma}\right)^2 A^2_B K \left(\frac{1}{V^2_M} + \frac{1}{V^2_{FC}}\right) \frac{1}{V^2_M - 3V^2_{FC}} \tag{10.66}$$

$$\tau_{0,new} = \left(\frac{w}{\sigma}\right) A_B K \left(\frac{1}{V^2_M} - \frac{V^2_{FC} + V^2_M}{V^2_{FC}\left(V^2_M - 3V^2_{FC}\right)}\right) \tag{10.67}$$

Propeller polar coefficients m and b follow from Eqq. 10.63 and 10.60, respectively.

The new equations have removed the strong influence of V_{SC}, but they have introduced an even higher uncertainty due to V_{FC}, which, with a $\pm 3\%$ error, raises at 25% the uncertainty on m and to 160% the b one. In fact, V_{FC} is alone at the denominator of $C^*_{D0,new}$, which justifies the huge consequent error.

The 3rd data set has the quality to cancel out any influence of V_{SC}, which is the most uncertain parameter; the drawback is that it increases the input error on output data, most of all on b.

10.5 TRAIL G70 Bootstrap approach results

The previous section showed how small errors in the input data are dramatically magnified in the Bootstrap results. Therefore, the choice of the proper data set is not trivial: the first one is definitely to be discarded, since errors are greatly propagated and V_{SC} has a higher level of uncertainty with respect to V_{FC} and V_M. The choice is between the second and the third data set: the former has a lower sensitivity to input uncertainties, but it employs the notorious V_{SC}; the latter has a huge sensitivity to errors, but it is made of two parameters which are less subject to uncertainty, namely V_{FC} and the direct measure of V_M.

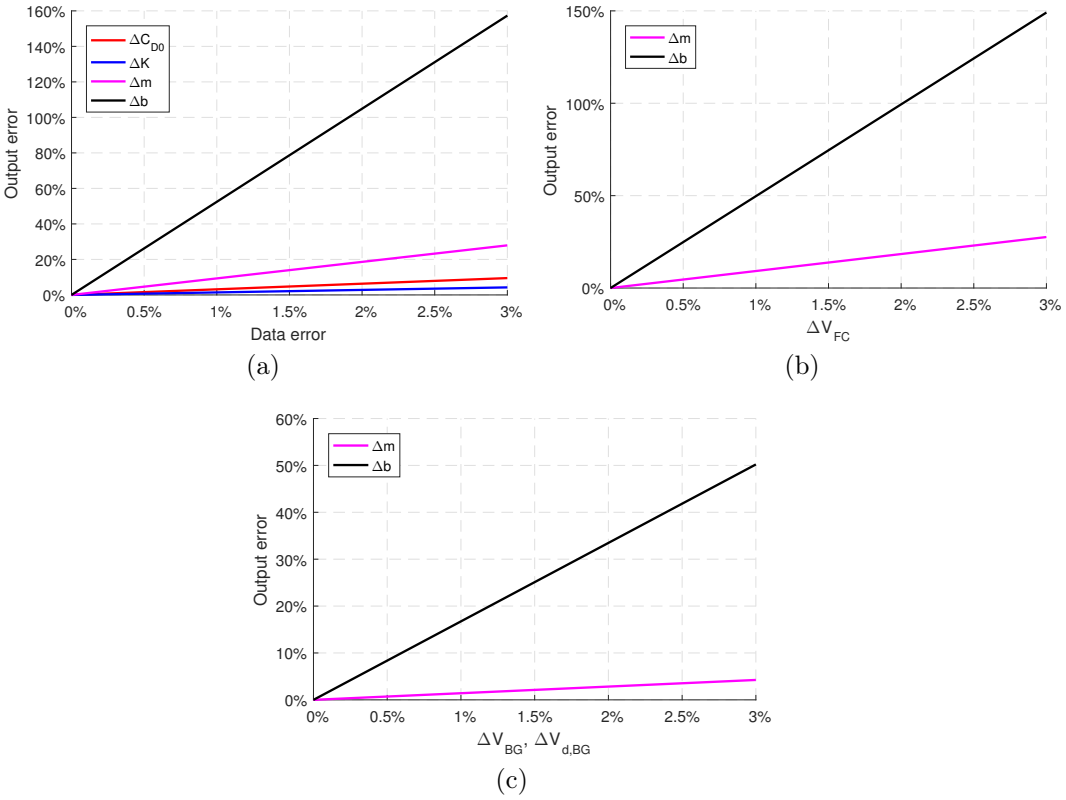

Figure 10.3: Bootstrap outputs sensitivity with single input variations.

Since there is not a direct measure of the climb angle, which would make the steepest climb speed almost exact, the third data set has been employed for TRAIL G70 Bootstrap performance analysis. To avoid misunderstandings, all the possible solutions have been tested and they are reported in Appendix D.

10.5.1 Bootstrap coefficients

The results in terms of drag and propeller polar coefficients are the ones in Tab 10.4. It is possible to immediately have an idea of the magnitude of the error on the drag coefficient by comparing them with the ones obtained in 9.2.5, which are, as a reminder, $C_{D0} = 0.0530$ and $K = 0.0565$; coefficients from polar estimation must be more reliable since they are based on a great amount of data. C_{D0} is very similar, while K is 9% less than the one predicted with the experimental polar.

Table 10.4: Bootstrap approach drag and propeller polar coefficients.

C_{D0}	0.0533
K	0.0516
m	2.6555
b	-0.0226

10.5.2 Speed envelope with Bootstrap approach

The most remarkable result of the Bootstrap approach is the possibility to obtain the whole speed envelope of the aircraft, which is shown in Figg. 10.4 and 10.5; the weight is set as the climb test one. The values of V_m, although correct from a mathematical point of view, are unrealistic for most of the envelope, since the stall speed results higher. Consequently, the lower bound of the flight envelope should be considered the stall speed, which varies with altitude in terms of TAS, while it is constant throughout the envelope if regarded as CAS, as much as the calibrated airspeed of steepest climb, which is constant at all the altitudes, too.

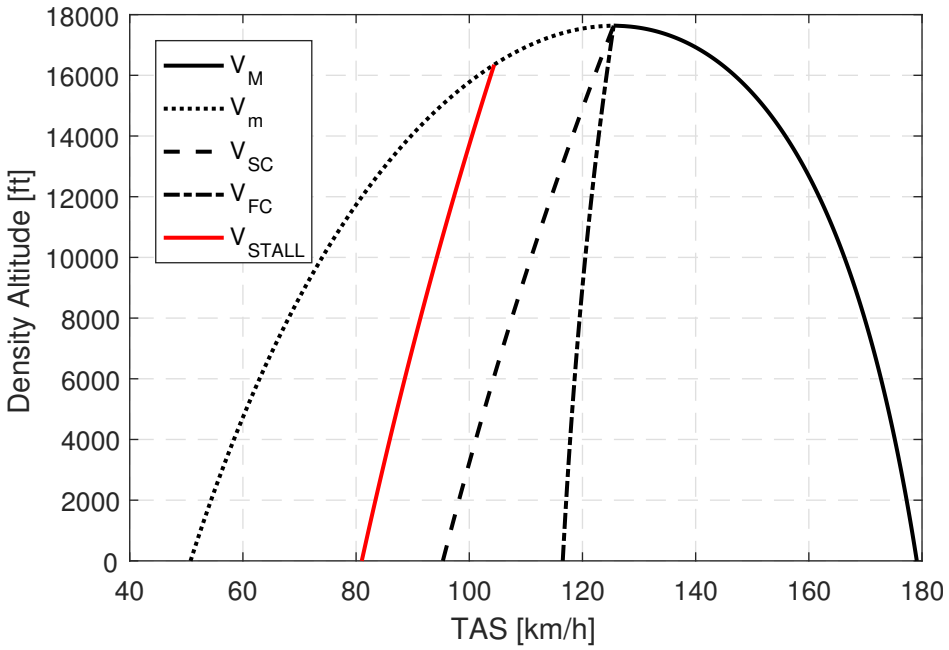

Figure 10.4: TAS envelope by means of the Bootstrap approach.

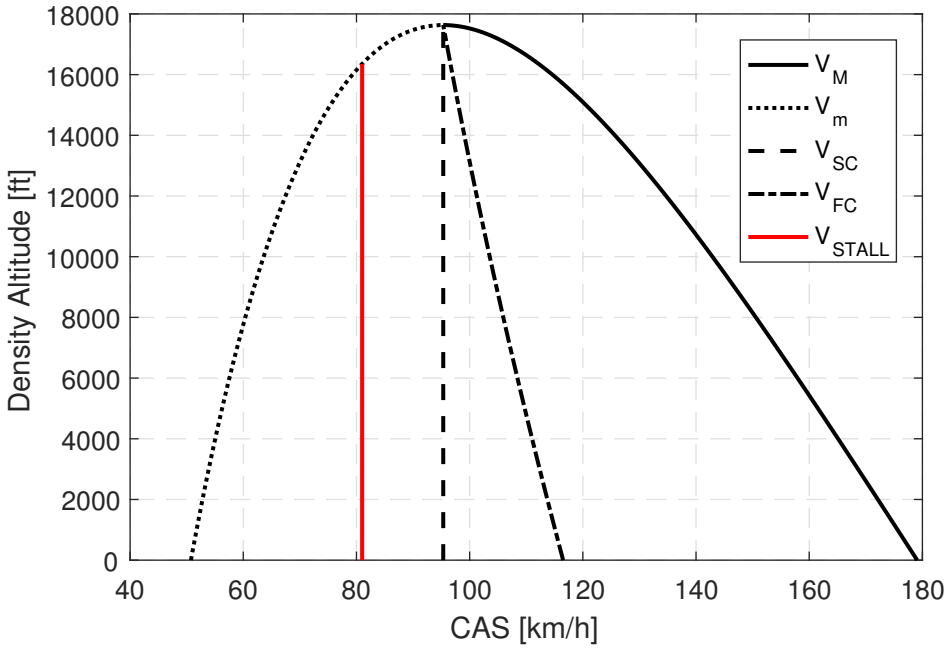

Figure 10.5: CAS envelope by means of the Bootstrap approach.

10.5.3 Bootstrap results at the conditions of the test

This section summarizes the graphs obtained with the Bootstrap approach referred to the test conditions in terms of weight and altitude in order to verify the quality of the performance prediction of the method.

Power available and requested

While the requested power has an acceptable value, even better than the other Groppo aircraft (see [11] and [21]), the available power is definitely low; indeed, the maximum available power during the test, according to the engine chart reported in [7], is about 80 HP, namely 59 kW, in the face of a maximum of 45 kW in the Bootstrap approach available power graph. Moreover, the maximum power has not been recorded at the maximum speed during the flight tests, but during the high speed climbs; the Bootstrap available power has the maximum power at the maximum speed.

The reason of this misleading result has to be found in the high level of uncertainty which affects the Bootstrap approach, even with relatively small errors on the data.

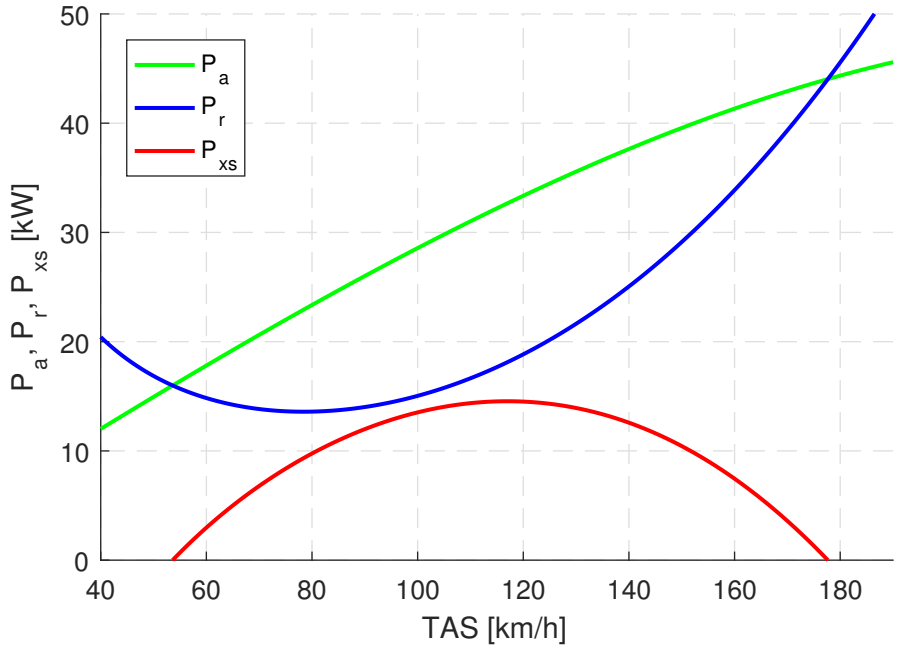

Figure 10.6: Requested, available and excess power obtained with the Bootstrap approach at 1600 ft with W=525 kg.

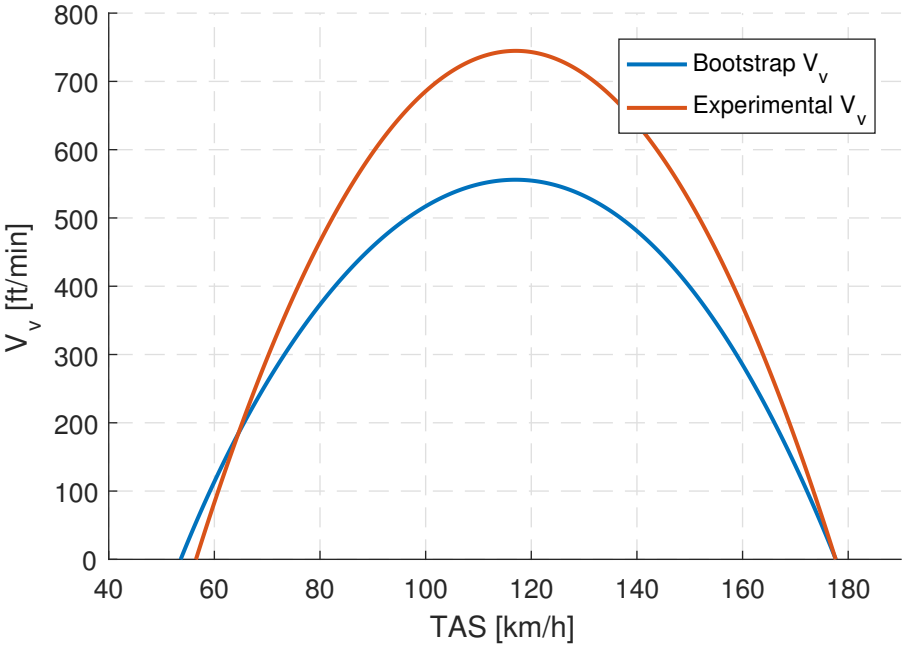

Figure 10.7: Rate of climb obtained with the Bootstrap approach at 1600 ft with W=525 kg.

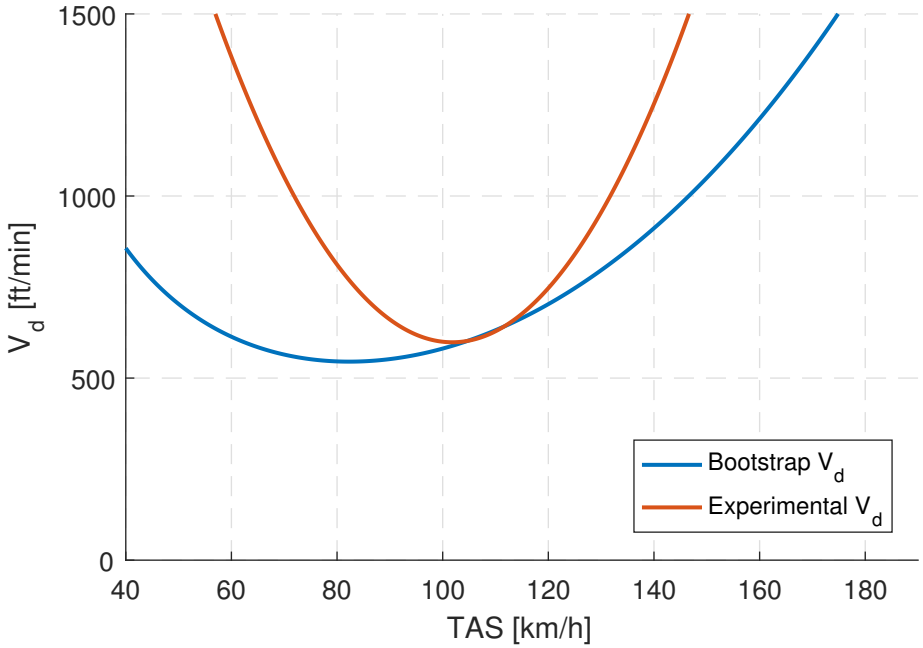

Figure 10.8: Rate of sink obtained with the Bootstrap approach at 2100 ft with W=570 kg.

Rate of climb and rate of sink

The rate of climb and rate of sink have been reported in Figg. 10.7 and 10.8 according to the different conditions of the climb and glide test and compared with the effective ones obtained in flight. Both the Bootstrap rates are dissimilar with respect to the experimental ones: the rate of climb is about 180 ft/min lower, while the rate of sink provides a good approximation only around the experimental V_{BG}, hence between 100 and 120 km/h.

10.5.4 *Ex-post* assessment of the input values

The aim of this subsection is to try to find out *ex-post* the input values which would have provided an acceptable result with the Bootstrap approach, in order to reinforce what previously said about the dramatic method's sensitivity. C_{D0} and K have already been calculated in 9.2.5, with a huge set of data including glide and trim test for the best accuracy: therefore they are regarded as the most reliable estimation of drag coefficients available. In this section they will be indicated as $\hat{C}_{D0}$ and $\hat{K}$. A two variables, non-linear system, is solved to find the values of $\hat{V}_{BG}$ and $\hat{\gamma}_{d,BG}$ needed to have the

mentioned drag coefficients, according to Eqq. 10.57 and 10.58:

$$\begin{cases} \dfrac{wA_B}{2\sigma}\dfrac{\hat{\gamma}_{d,BG}}{\hat{V}_{BG}} = \hat{C}_{D0} \\ \dfrac{\sigma}{2wA_B}\hat{V}_{BG}\hat{\gamma}_{d,BG} = \hat{K} \end{cases} \tag{10.68}$$

The approximation $\sin\gamma_{d,BG} \approx \gamma_{d,BG}$ and $\cos\gamma_{d,BG} \approx 1$ for $\sin\gamma_{d,BG}$ small has been employed, hence:

$$\frac{\tan^2\gamma_{d,BG}}{\sin\gamma_{d,BG}} = \frac{\sin\gamma_{d,BG}}{\cos^2\gamma_{d,BG}} \approx \gamma_{d,BG} \tag{10.69}$$

The solution of the system is:

$$\hat{V}_{BG} = 110.1 \quad km/h$$
$$\hat{\gamma}_{d,BG} = 6.25 \quad deg$$

Differently from drag coefficients, there are not reliable data for m and b for making Bootstrap excess power the same of the real aircraft one. Assuming exact the value of V_M, it is possible to tune the value of V_{FC} until the ROC Bootstrap graph coincides with the one obtained with flight testing. The result is:

$$V_{FC} = 118.0 \quad km/h$$

Tab. 10.5 summarizes the results: variations of speed are very small, in the order of 2% maximum, whilst the variation in the angle of best glide is more pronounced, at 4%; however the latter is a difference of a quarter degree, which, translated in rate of sink, means $\Delta V_{d,BG} = 0.20$ m/s with respect to an original value of $V_{d,BG} = 3.13$ m/s.

Table 10.5: Bootstrap original inputs and modified ones to obtain truthful results.

Input	Original	Modified	Difference
V_{FC} $[km/h]$	117.0	115.2	-1.5%
V_{BG} $[km/h]$	108.0	110.1	$+2.0\%$
$\gamma_{d,BG}$ $[deg]$	5.99	6.25	$+4.3\%$

With such small variations in the inputs, outputs change as reported in Tab. 10.6. The variations are similar to the ones expected with RSS; b, in particular, confirms its high sensitivity to small input perturbation.

Table 10.6: Bootstrap original inputs and modified ones to obtain truthful results.

Output	Original	Modified	Difference
C_{D0}	0.0533	0.0530	-0.6%
K	0.0516	0.0565	$+9.5\%$
m	2.6555	3.3539	$+26.3\%$
b	-0.0226	-0.0540	-138%

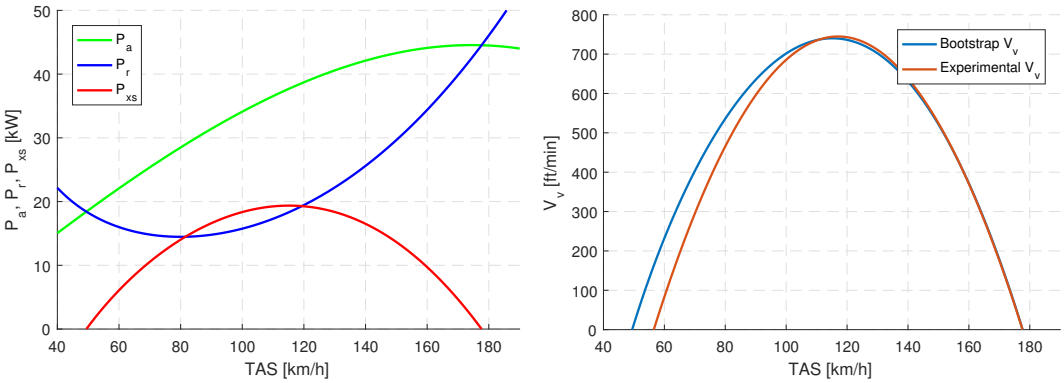

(a) (b)

Figure 10.9: Performance graphs with Bootstrap approach modified input parameters.

The results in terms of Penaud's graphs and rate of climb with the modified data are shown in Fig. 10.9. Available power is still lower than the one registered on-board by means of the Rotax manual ([7]), but now it has a more acceptable shape: its peak has moved backwards and it is no more coincident with the maximum speed.

Chapter 11

Conclusions

This thesis describes the structured flight test campaign executed for final development and pre-certification of a new ultralight aircraft, namely the second generation of the Nando Groppo G70. In contrast to the typical situation in the ultralight aviation segment, where FTI is not commonly employed and flight data are recovered by using native cockpit instrumentation, in the present case the aircraft was fitted with a very easy to handle, complete and accurate FTI developed at *Politecnico di Milano*.

The campaign involved both performance and stability & control test items, with the German LTF-UL norms as reference for airworthiness requirements. Initially, air data calibration was performed in order to investigate the fitness of the static probe. The first reported issue is the high error of the static probe, which is translated in an abnormal indication of airspeed on the on-board anemometer. Therefore, the whole campaign was executed with the static probe inside the cabin, where there is not influence of the propeller air stream; this temporary solution is not acceptable for certification and the static probe has to be shifted in a less disturbed area on the fuselage for final demonstration.

Stall speed has been determined and its value is higher than that of the first generation of the G70; moreover, stall speed in landing configuration is about 10 km/h higher than the LTF-UL limit of 65 km/h. The main role in the stall speed raise is played by the vortex generators, which in the old G70 covered all the leading edge of the wing, while in the new G70 are only in front of the ailerons. Take-off and landing distances have an acceptable value compared to the normal distance of UL airstrips; take-off run is well below the LTF-UL 300 m limit. Climb performance is satisfying both in CR and TO: the LTF-UL request is largely respected and the rate of climb is even slightly higher than the one of the first G70 generation.

Lateral-directional control tests show a linear response of the aircraft and

a time to bank well below the LTF-UL limit. Unfortunately, the test has been executed with the first aircraft configuration and it should be repeated. The result is not supposed to vary greatly and will be most likely still below the limit. Elevator forces during manoeuvre show a well defined positive gradient of stick force with respect to load factor and, consequently, LTF-UL requirements are fulfilled. Trimmability is optimal and no issues arise when the pilot steers the aircraft in steady level flight, for all the CG locations and along the whole speed envelope.

Longitudinal static stability is demonstrated, with acceptable gradients of stick force versus airspeed, comparable to the ones of the old G70. Some uncertainties in the prediction of the aircraft behaviour arises when the flaps are set in LND position: pushing the stick does not provide to the pilot the correct feedback in terms of force, which is way lower than the one registered in TO and CR. This issue, whose cause is probably the deviation of air stream due to deflected flaps, which eases the lowering of the elevator during the manoeuvre, has to be further investigated by the manufacturer. Lateral-directional static stability is demonstrated, although LND configuration has not been tested due to time constraints; certification will require the execution of this latter test.

Dynamic stability is generally verified for all possible aircraft modes. The LTF-UL requirements that all short period modes are adequately damped in both stick-fixed and stick-free conditions were assessed, with the exception of the Dutch Roll mode. In this case, the tests were not executed following the correct technique, which requests a proper rudder excitation of the mode, and should therefore be repeated. However, there have never been any signs of lateral-directional instability during the whole campaign and the test will most likely have a fully satisfying result.

In order to sum up the part related to type certification, the improvements to be done on the prototype before certification are as follows:

- air data system static error shall be corrected, to make more reliable the speed indication of the anemometer;
- stall speed shall be reduced. Two ways are possible, either installing vortex generators along the whole wing span, or closing the gap between flap and wing;
- stick authority with full flaps has to be increased and consequently verified.

Tests which have to be executed *ex-novo* are:

- Stall behaviour with MCP and in turning flight;
- Lateral-directional static stability in LND configuration;
- Longitudinal control throughout the whole flight envelope, which has not been executed for time constraints.

Tests whose results are expected to be good, but they have to be executed for a rigorous indication of compliance with LTF-UL:

- Dutch roll in CR and LND, to be done with the standard CS23 FTG execution;
- Lateral-directional manoeuvrability, to be performed in the final aircraft configuration.

The neutral point has been experimentally calculated with a good degree of accuracy, given the high quality of the test points and the resemblance of the in-flight results with the prediction of two different numerical methods. The aircraft drag polar has been successfully determined, based on the large amount of data from glides and trim tests. The analysis showed a certain degree of uncertainty of the propeller efficiency calculated by a software available online. While this tool may provide efficiency values acceptable in a first approximation, the overall result will be misleading whenever good accuracy is required, as drag polar estimation: C_D value can float in a very narrow range and small variations in the propeller efficiency can induce a significant error in the results. Fortunately, the uncertainty propagation analysis proved that results drawn from trim points at high speed are less prone to vary with propeller efficiency.

The Bootstrap approach to flight performance has been employed to draw the airspeed-altitude envelope of the aircraft and to provide four coefficients (C_{D0} and K for drag and m and b for the linear propeller polar) which can be used to predict the overall performance of the aircraft for all the conditions of weight and density altitude. The method can be applied using different data sets. All candidate data sets have been studied in order to define the best one in terms of data quality and error sensitivity of the outputs. Uncertainty propagation analysis has been performed for all the data sets, with a surprising result: small perturbations of inputs can dramatically vary the output coefficients, up to the 140-160 % variations in one of them. A large sensitivity to input variations has been proved also with an *ex-post* calculation of the input data which would have provided a result similar to the experimental one.

The present work may represent a reliable basis on which further analysis can be carried out in the future. On one hand, the characterization of the aircraft drag and longitudinal static stability characteristics may be used for the next campaign, when planning relevant flight test items. On the other hand, the methodology developed for deriving these results, as well as those related to certification requirements, may be useful for the final compliance demonstration and for similar activities on airplanes in the same class.

Appendix A

Air data calibration

Anemometer calibration - Flight 01.1405

The first air data calibration took place in the first flight, 01.1405, with unsatisfactory results for two reasons:

- The track indication has been read on the EFIS native screen since the AvMap GPS was not available that day; for all the duration of the test the EFIS reported a value of track equal to the value of heading, which looks suspicious, even if the flight takes place in smooth air conditions;
- The calibration showed a very high error on the static probe, of at least 10 km/h along the whole envelope of velocity.

Test results in terms of calibration line and anemometer compliance are shown in Figg. A.1 and A.2.

Anemometer calibration - Flight 01.2005

Since the EFIS of the aircraft showed a not acceptable level of unreliability in the first air data calibration, for 01.2005 flight the main AvMap GPS screen has been used. Unfortunately, the results were not dissimilar from the past ones, in particular the error, totally out of compliance, made the CAS be 10 km/h higher along the whole envelope. At this point, it was clear that the calibration problem was not in the instrumentation used, although the EFIS problems were demonstrated and out of discussion, but in the static probe.

Test results in terms of calibration line and anemometer compliance are shown in Figg. A.3 and A.4.

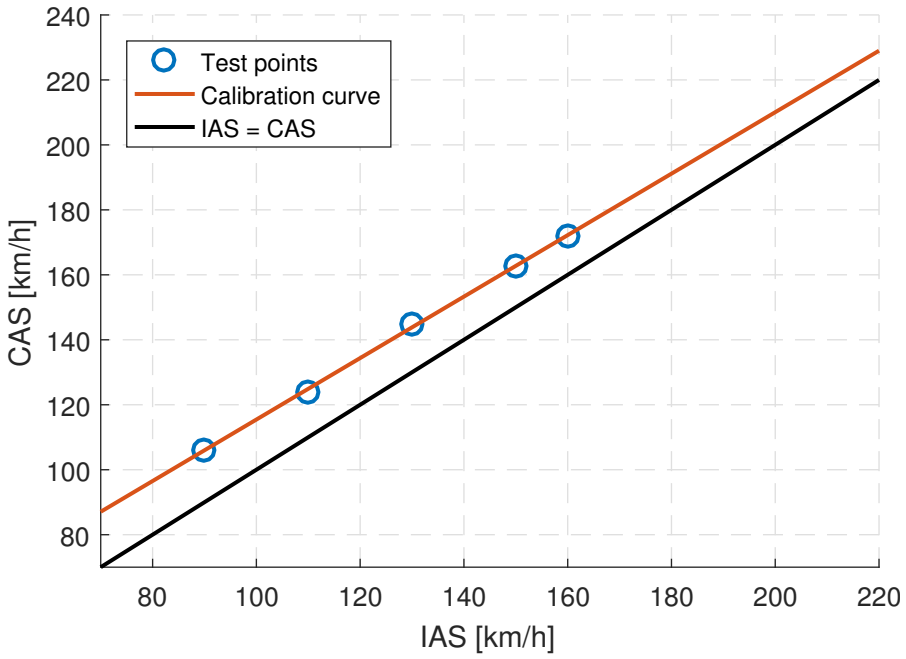

Figure A.1: Calibration line as resulted in flight 01.1405.

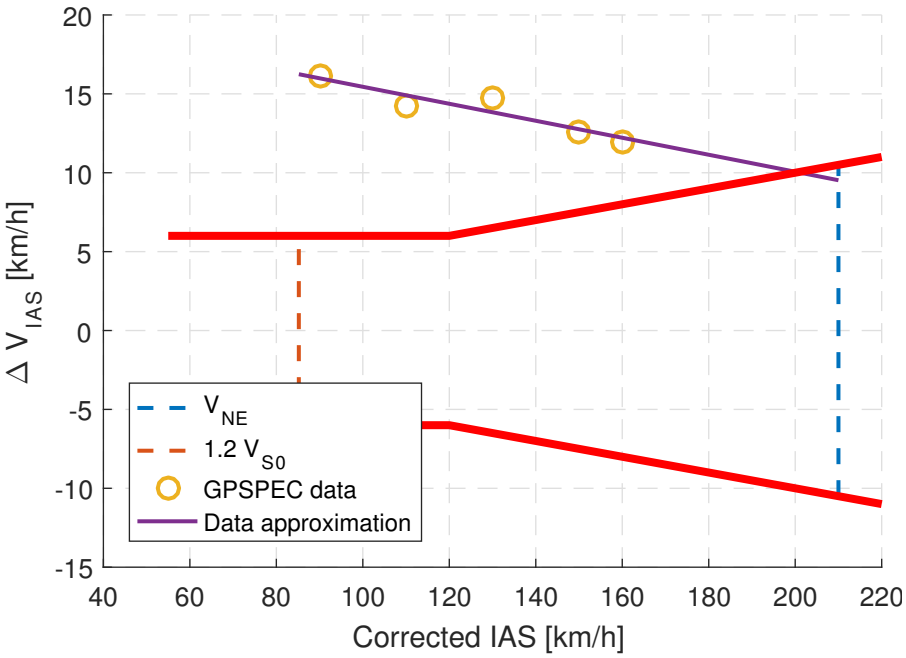

Figure A.2: IAS error and limits of LTF-UL, as resulted in flight 01.1405.

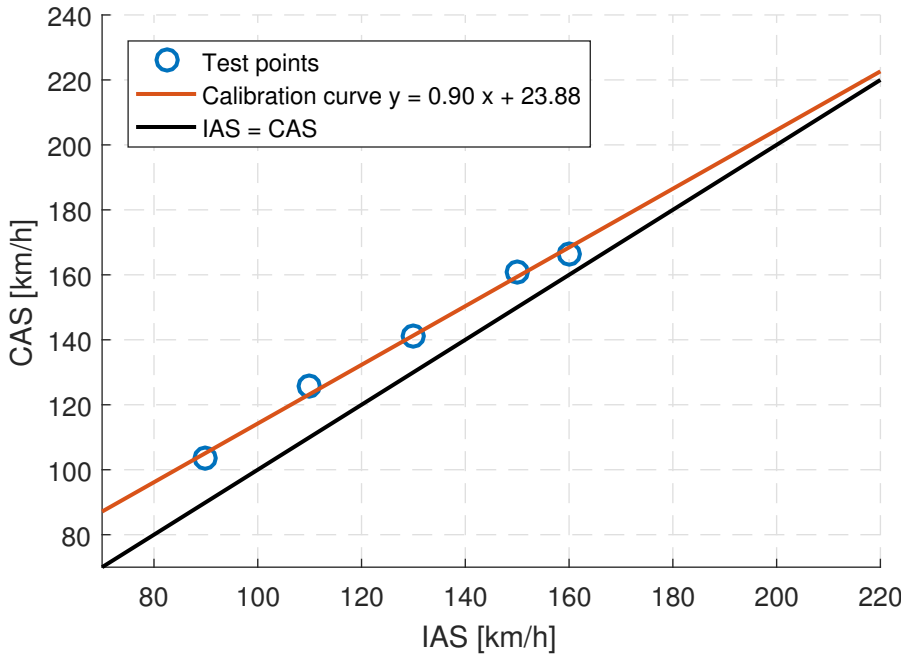

Figure A.3: Calibration line as resulted in flight 01.2005.

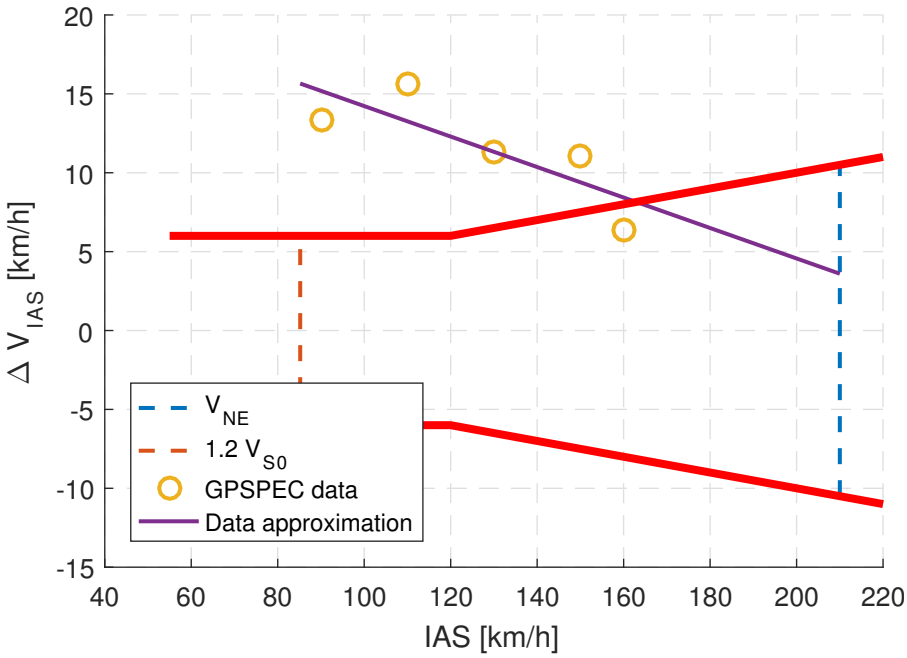

Figure A.4: IAS error and limits of LTF-UL, as resulted in flight 01.2005.

Appendix B

Performance

B.1 Climb performance

B.1.1 Basic theory of climbing test

During a steady climb, a vertical and horizontal equilibrium leads to:

$$L = W\cos\gamma \tag{B.1a}$$
$$T = D + W\sin\gamma \tag{B.1b}$$

Eq. B.1b, with Newton's Law $\sum F = Ma$, becomes:

$$T - D - W\sin\gamma = Ma = \frac{W}{g}\frac{dV}{dt} \tag{B.2}$$

By multiplying V_{TAS} and dividing the weight:

$$\frac{V(T-D)}{W} = V\sin\gamma + \frac{V}{g}\frac{dV}{dt} \tag{B.3}$$

where $V\sin\gamma$ is vertical speed, namely $\dfrac{dH}{dt}$. Excess power is defined as

$$P_{xs} = V(T-D) \tag{B.4}$$

therefore:

$$P_{xs} = W\frac{dH}{dt} + \frac{W}{g}\frac{dV}{dt}V \tag{B.5}$$

During a constant TAS climb, the second term of Eq. B.5 is null and all the excess energy is spent to climb; on the other hand, during a steady flight, the excess power contributes to accelerate the airplane. Since the climb

during the sawtooth test is performed at the same IAS, the acceleration contribution, which depends on TAS, is not null, although relatively small; this is the reason why one of the corrections of 5.5.3 includes the TAS gradient with altitude. With both the contributions of excess power, it is possible to reconstruct the test day $P_S = P_a - P_r$; the latter needs to be reduced to ISA conditions and to standard weight, influencing both P_a, which depends on temperature, and P_r, which depends on weight with the induced drag.

B.1.2 Additional ROC graphs

Aircraft configuration 1

The test has been executed in flight 02.1405, CR configuration, at 1300 ft. Tab. B.1 gathers the test data, while Tab. B.2 summarizes the corrections applied to each test point of the climb.

Table B.1: Climb data in aircraft configuration 1, flight 02.1405.

Climb	1	2	3	4	5	6
IAS [km/h]	90	100	110	120	130	167
CAS [km/h]	106	115	124	134	143	179
TAS [km/h]	108	118	127	137	147	183
ROC [m/s]	3.9	4.4	3.9	3.6	3.3	0

Table B.2: Corrections for every climb during flight 02.1405.

Climb	1	2	3	4	5	6
$\left(\frac{\Delta h}{\Delta t}\right)_t \frac{W_T}{W_S}$ $[m/s]$	4.98	5.58	4.95	4.61	4.21	0
$\Delta\left(\frac{\Delta h}{\Delta t}\right)_P \frac{W_T}{W_S}$ $[m/s]$	0.14	0.15	0.16	0.17	0.17	0.18
$\Delta\left(\frac{\Delta h}{\Delta t}\right)_{AF} \frac{W_T}{W_S}$ $[m/s]$	0.29	0.38	0.40	0.43	0.45	0
$\Delta\left(\frac{\Delta h}{\Delta t}\right)_{ind}$ $[m/s]$	0.18	0.17	0.16	0.15	0.14	0.11
$\left(\frac{\Delta h}{\Delta t}\right)_{std}$ $[m/s]$	5.59	6.27	5.66	5.35	4.96	0.29

The final result, meant as the Rate of Climb 2nd order least-squares

approximation curve, is reported in Fig. B.1 ad summarized in Tab. B.3. Compliance with LTF-UL is demonstrated with a broad margin.

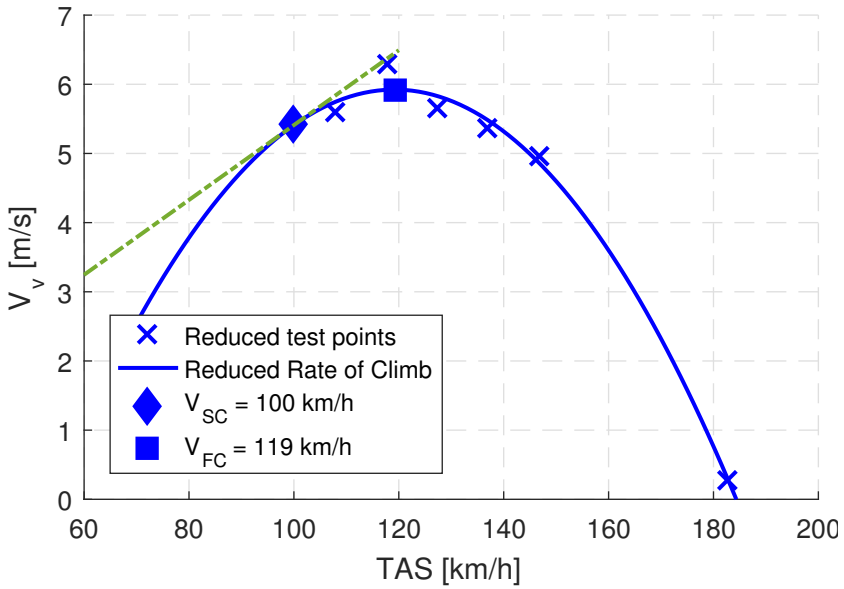

Figure B.1: Rate of Climb during flight 02.1405, CR configuration, 1300 ft.

Table B.3: V speeds after flight 02.1405 climbs analysis, CR configuration, 1300 ft.

Aircraft conf.	Flap conf.	V_{SC} [km/h]	V_{FC} [km/h]	$maxROC$ [m/s]
01	CR	99	119	5.92

Aircraft configuration 2

The test has been executed in flight 02.0206, CR configuration, at 1400 ft. Tab. B.4 gathers test data, while Tab. B.5 summarizes the corrections applied to each test point of the climb.

Table B.4: Climb data in aircraft configuration 2, flight 02.0206.

Climb	1	2	3	4	5
IAS [km/h]	100	110	120	130	189
CAS [km/h]	101	109	117	125	172
TAS [km/h]	103	112	120	128	176
ROC [m/s]	4.33	3.62	4.38	4.25	0

Table B.5: Corrections for every climb during flight 02.0206.

Climb	1	2	3	4	5
$\left(\frac{\Delta h}{\Delta t}\right)_t \frac{W_T}{W_S}$ $[m/s]$	5.53	4.63	5.60	5.43	0
$\Delta\left(\frac{\Delta h}{\Delta t}\right)_P \frac{W_T}{W_S}$ $[m/s]$	0.23	0.23	0.24	0.25	0.29
$\Delta\left(\frac{\Delta h}{\Delta t}\right)_{AF} \frac{W_T}{W_S}$ $[m/s]$	0.29	0.28	0.40	0.44	0
$\Delta\left(\frac{\Delta h}{\Delta t}\right)_{ind}$ $[m/s]$	0.18	0.17	0.15	0.14	0.10
$\left(\frac{\Delta h}{\Delta t}\right)_{std}$ $[m/s]$	6.23	5.31	6.39	6.27	0.39

The final result, meant as the Rate of Climb 2nd order least-squares approximation curve, is reported in Fig. B.2 ad summarized in Tab. B.6. The compliance with LTF-UL is demonstrated with a broad margin.

It is observable an increase of the maximum ROC of climb with respect to the flight 02.1405; the reason is definitely the removal of more than half vortex generators, which has reduced the drag on the wing surface.

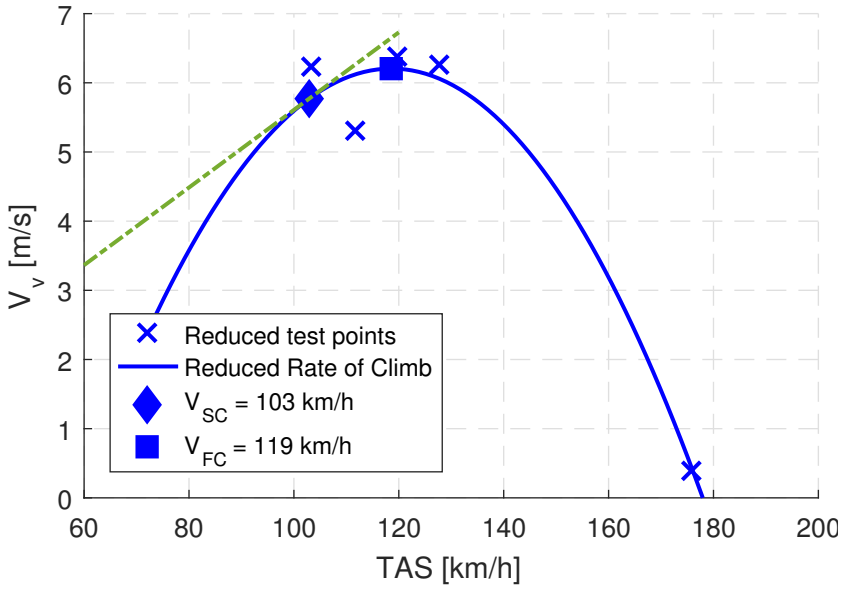

Figure B.2: Rate of Climb during flight 02.0206, CR configuration, 1400 ft.

Table B.6: V speeds after flight 02.0206 climbs analysis, CR configuration, 1400 ft.

Aircraft conf.	Flap	V_{SC} [km/h]	V_{FC} [km/h]	$maxROC$ [m/s]
02	CR	103	119	6.21

Aircraft configuration 3

This section groups some additional tests in the final configuration not reported in the main corpus for sake of brevity.

Table B.7: V speeds after flight 05.1006, 01.1507 and 05.1106 climbs analyses.

Airc. conf.	Flap	h [ft]	V_{SC} [km/h]	V_{FC} [km/h]	$maxROC$ [m/s]
03	CR	85	110	5.00	
03	CR	2100	106	122	4.85
03	TO	1300	96	118	4.84

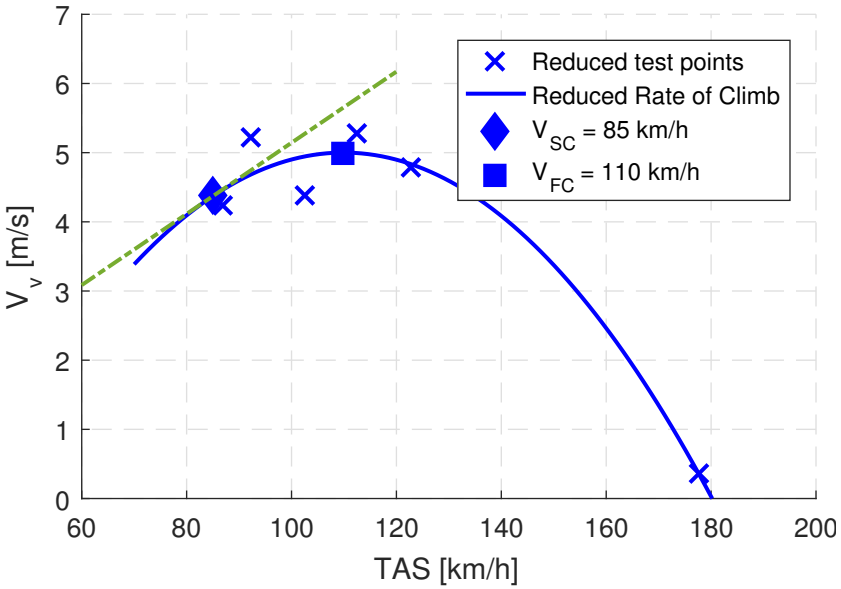

Figure B.3: Rate of Climb during flight 05.1006, CR configuration, 1600 ft.

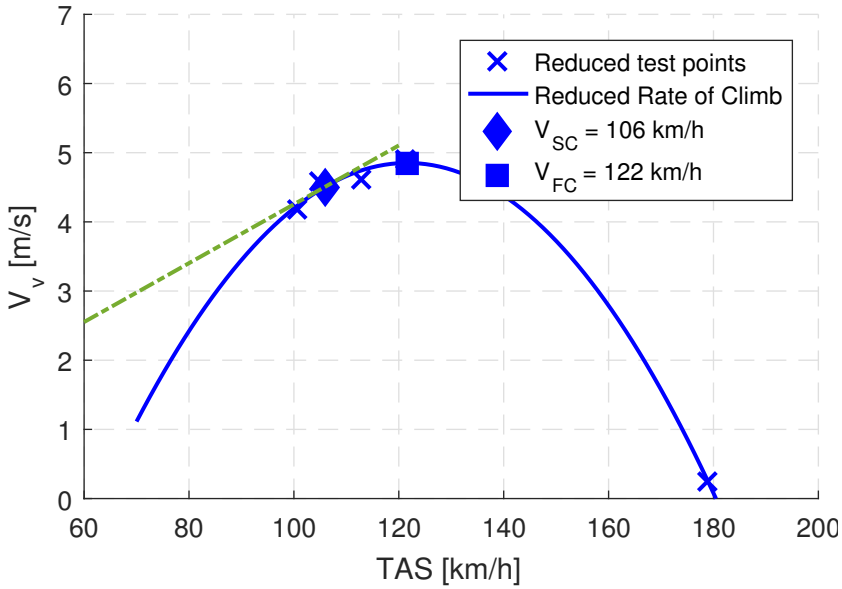

Figure B.4: Rate of Climb during flight 01.1507, CR configuration, 2100 ft.

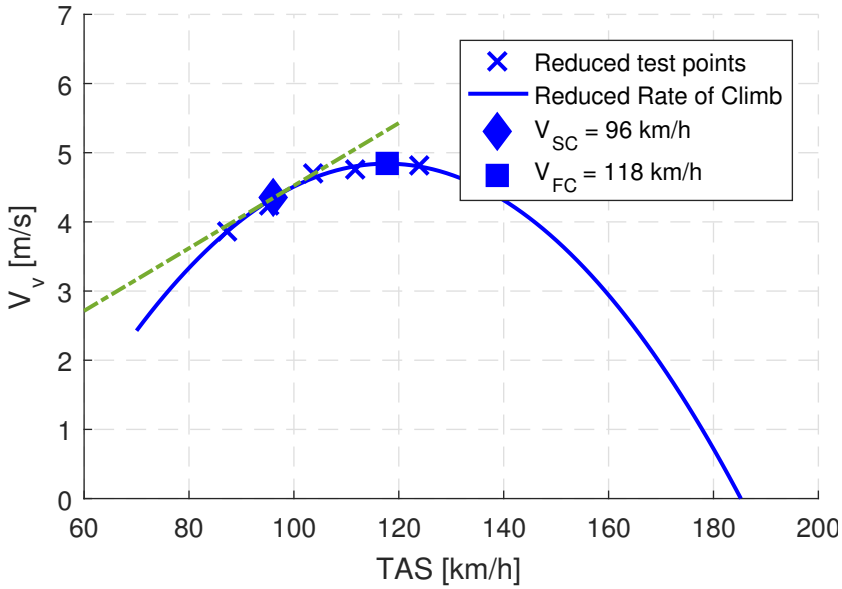

Figure B.5: Rate of Climb during flight 05.1106, TO configuration, 1300 ft.

Appendix C

Static and dynamic stability

C.1 Static longitudinal stability additional graphs

Firstly, an example of time history for each configuration of flaps is reported. Secondly, as stated in the main section, the static longitudinal stability in LND configuration shows some critical issues about the push phase, namely when the pilot tries to pitch the nose down the command loses authority with a very low force versus speed slope or even with an inversion of the command. Unfortunately, the data obtained during flight 01.1106 are not reliable due to the excessive variance of speed and stick force, which prevents from an accurate point extrapolation; therefore, the only test point in LND configuration available for a comparison is the one of flight 02.1106, TOP3. Its final result is reported in Fig. C.4.

The values of the gradients are:

- $\left.\frac{\partial F}{\partial V}\right|_{PULL} = -0.41 \quad \frac{N}{km/h}$
- $\left.\frac{\partial F}{\partial V}\right|_{PUSH} = 0.13 \quad \frac{N}{km/h}$

The pull gradient is almost the same already found in the test point showed in 7.1.4, which was 0.47, but the issue is clear for the push phase: the elevator moved without any effort of the pilot, whose force on the stick decreased with the speed increasing.

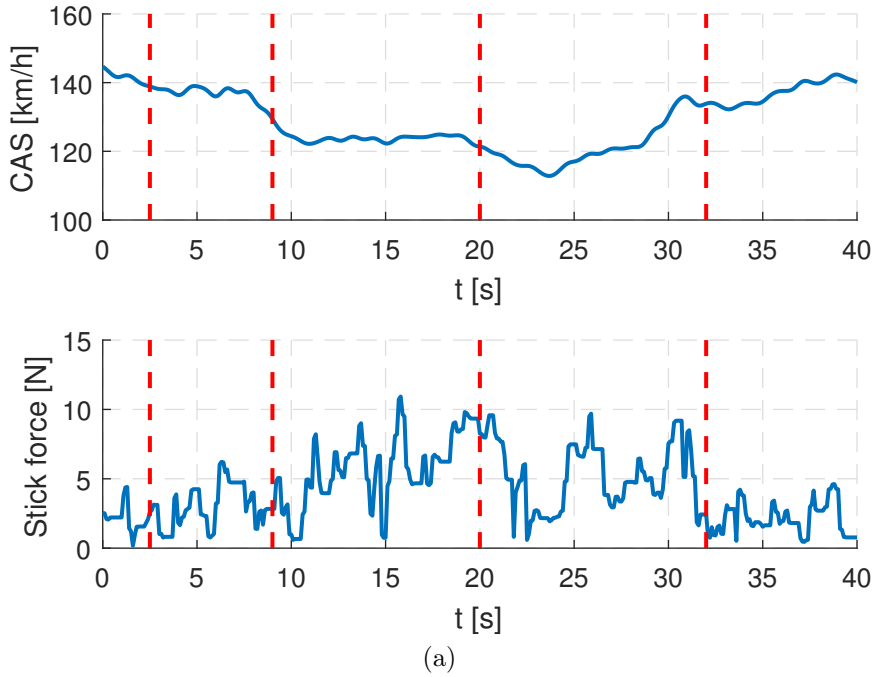

(a)

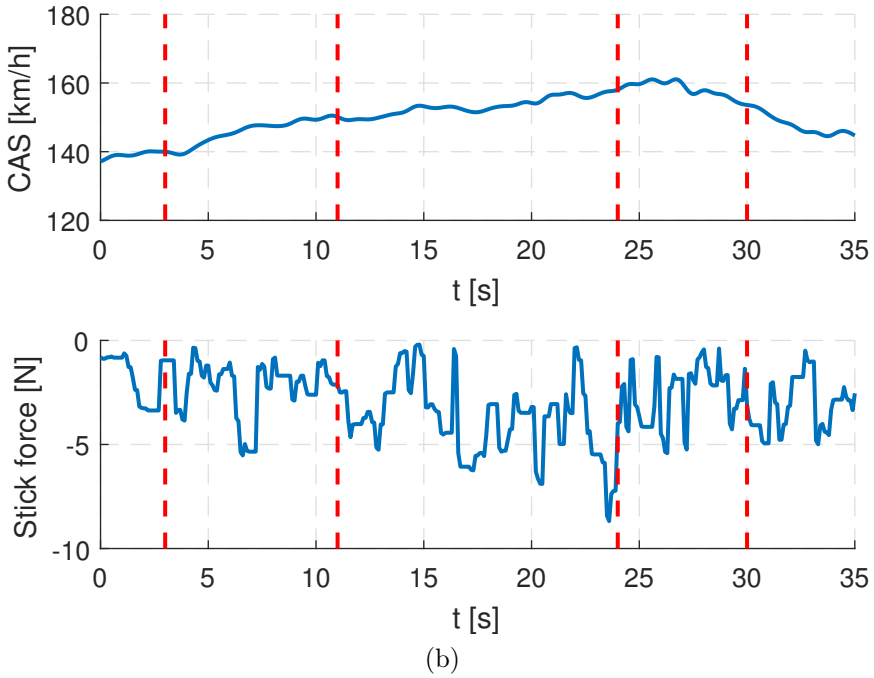

(b)

Figure C.1: Pull (C.1a) and push (C.1b) speed stability CAS and stick force time history in CR configuration (trim speed 140 km/h), flight 03.1706.

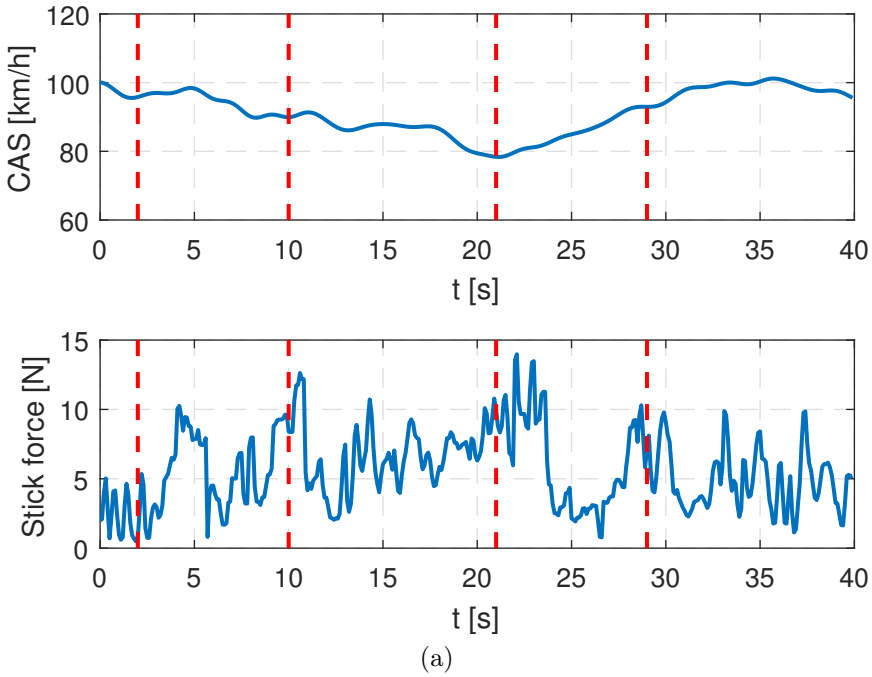

(a)

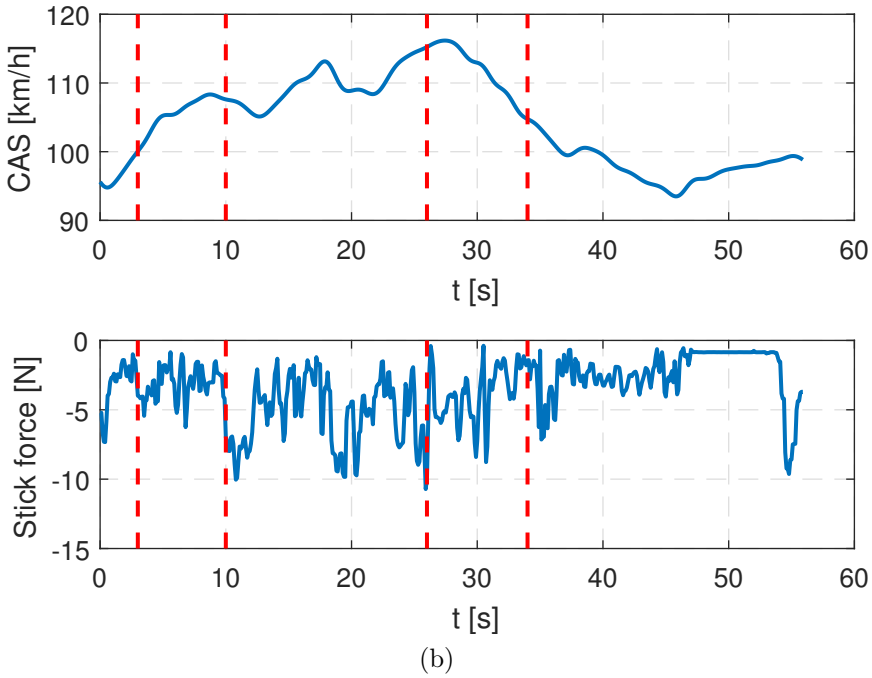

(b)

Figure C.2: Pull (C.2a) and push (C.2b) speed stability CAS and stick force time history in TO configuration (trim speed 100 km/h), flight 04.1106.

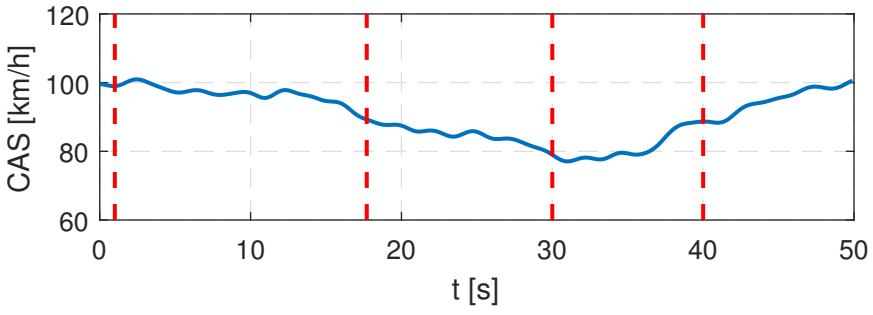

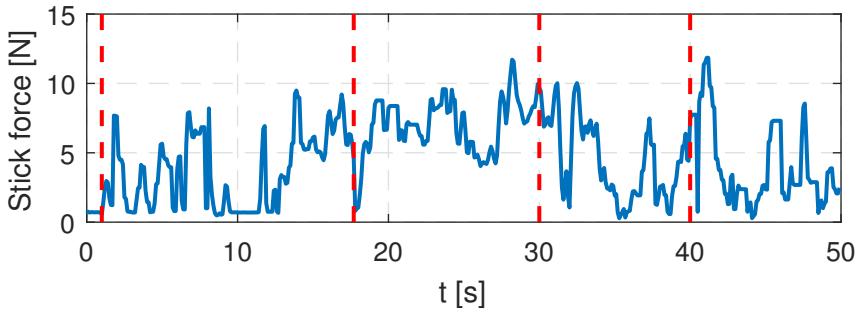

(a)

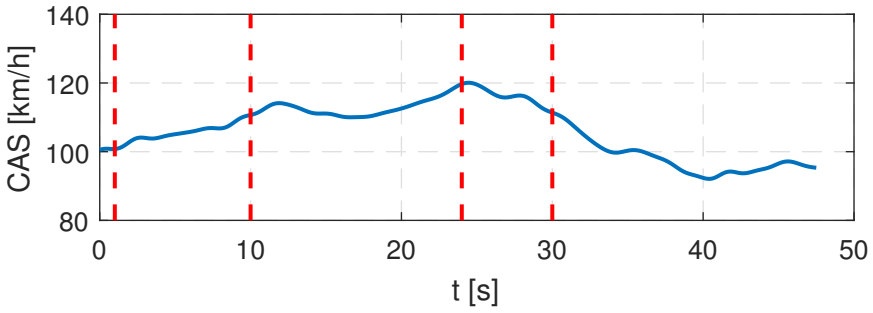

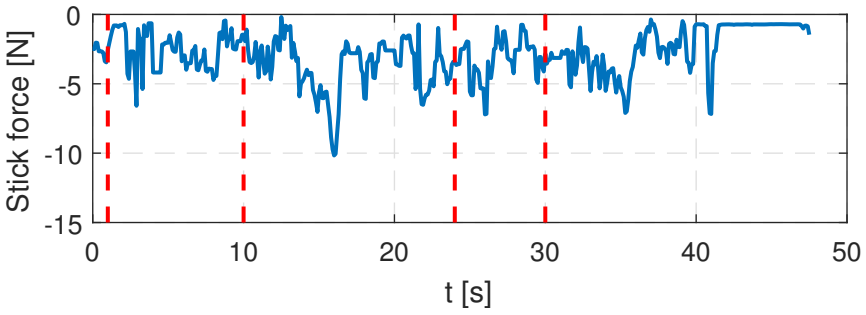

(b)

Figure C.3: Pull (C.3a) and push (C.3b) speed stability CAS and stick force time history in LND configuration (trim speed 100 km/h), flight 02.1106.

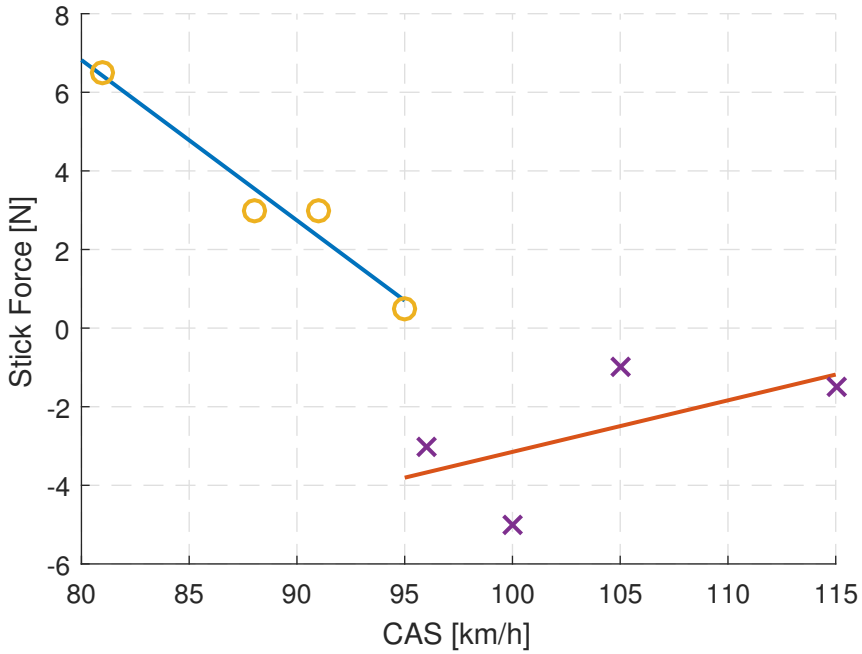

Figure C.4: Speed stability stick force vs speed, LND configuration, flight 02.1106 TOP 3.

C.2 Static lateral directional stability additional graphs

This section gathers some examples of time history in CR and TO configuration and additional test points to show the tendency of the rudder to lose effectiveness by increasing the speed.

Flight 01.1706 TOP 10 (CR configuration) gradients:

- $\frac{\partial \beta}{\partial \delta_R} = 1.10$
- $\frac{\partial \delta_A}{\partial \delta_R} = -0.51$

Flight 05.1106 TOP 10 (TO configuration) gradients:

- $\frac{\partial \beta}{\partial \delta_R} = 1.12$
- $\frac{\partial \delta_A}{\partial \delta_R} = -0.36$

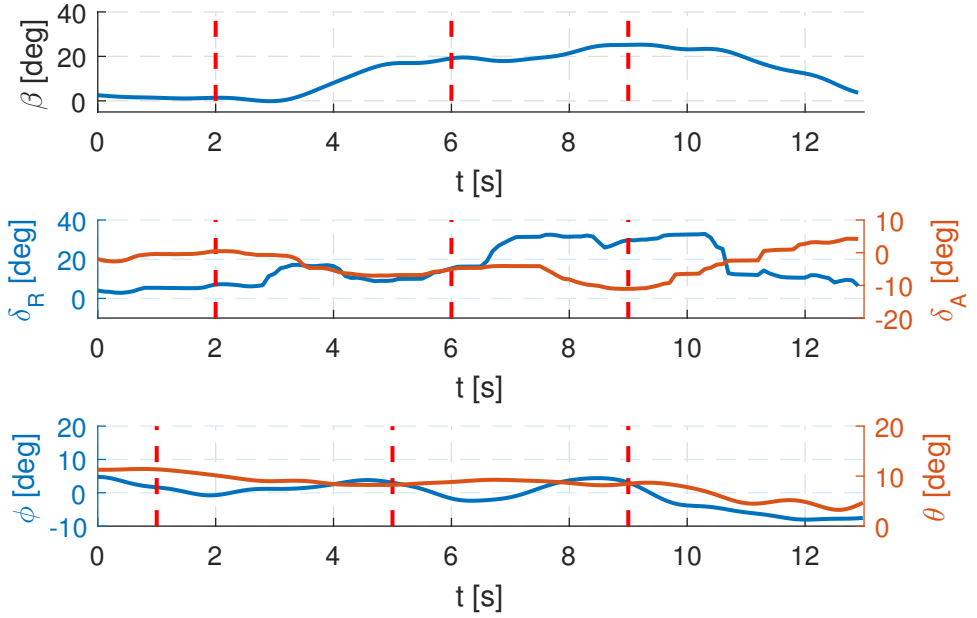

(a)

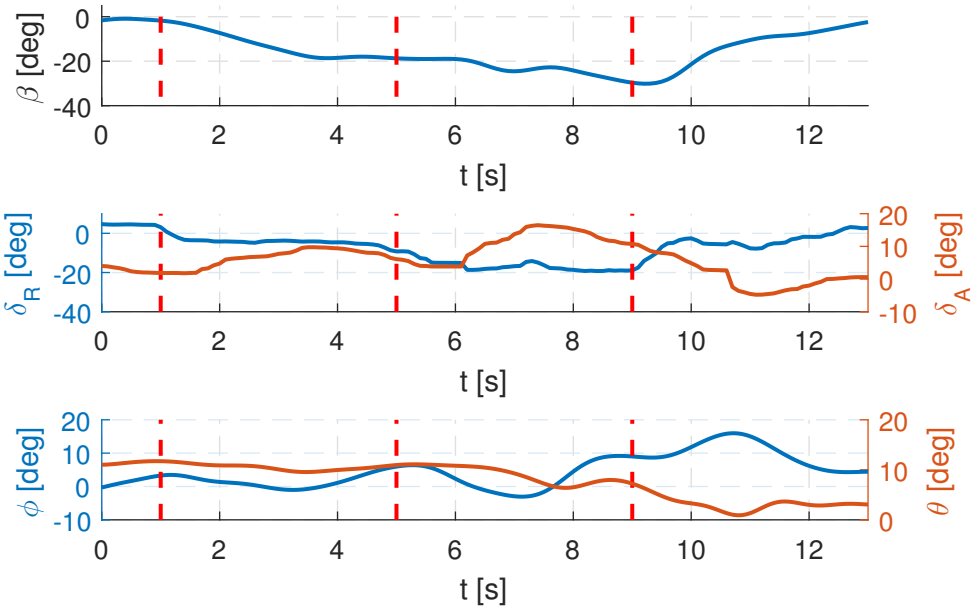

(b)

Figure C.5: Left (C.5a) and right (C.5b) SHSS time history with the most remarkable parameters in CR configuration (trim speed 90 km/h), flight 01.1706 TOP 9.

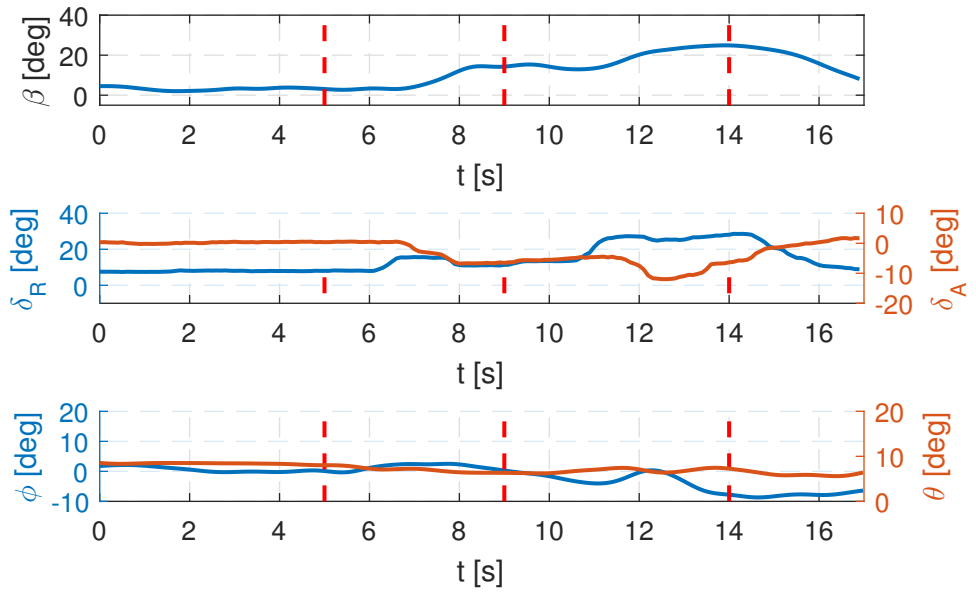

(a)

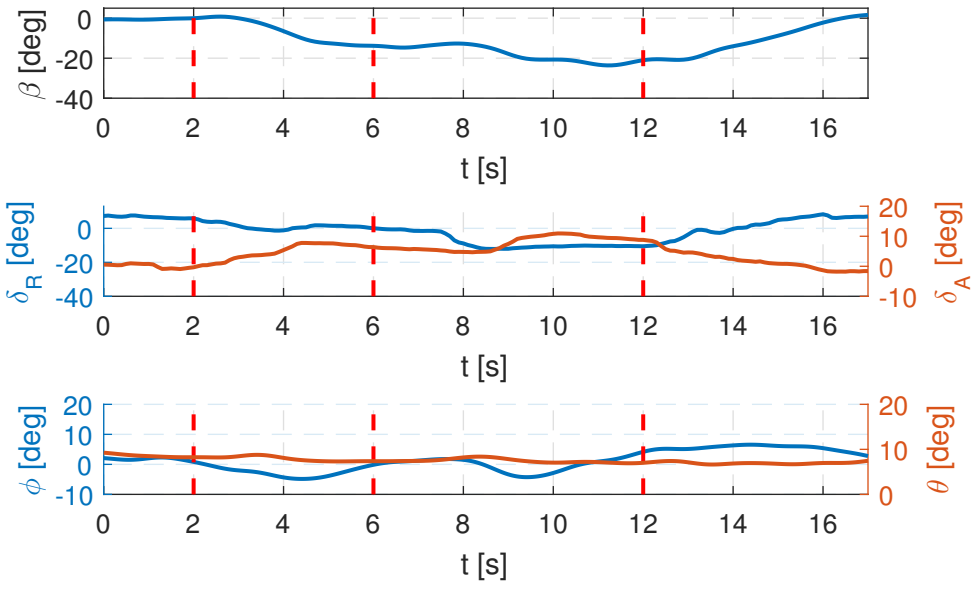

(b)

Figure C.6: Left (C.6a) and right (C.6b) SHSS time history with the most remarkable parameters in TO configuration (trim speed 90 km/h), flight 05.1106 TOP 9.

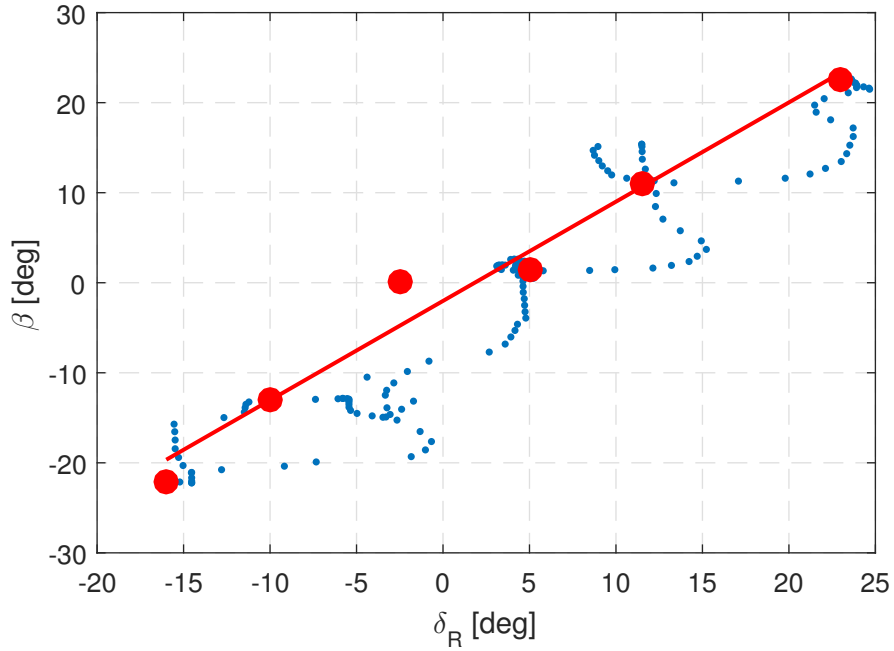

Figure C.7: SHSS β vs δ_R, CR configuration, flight 01.1706 TOP 10.

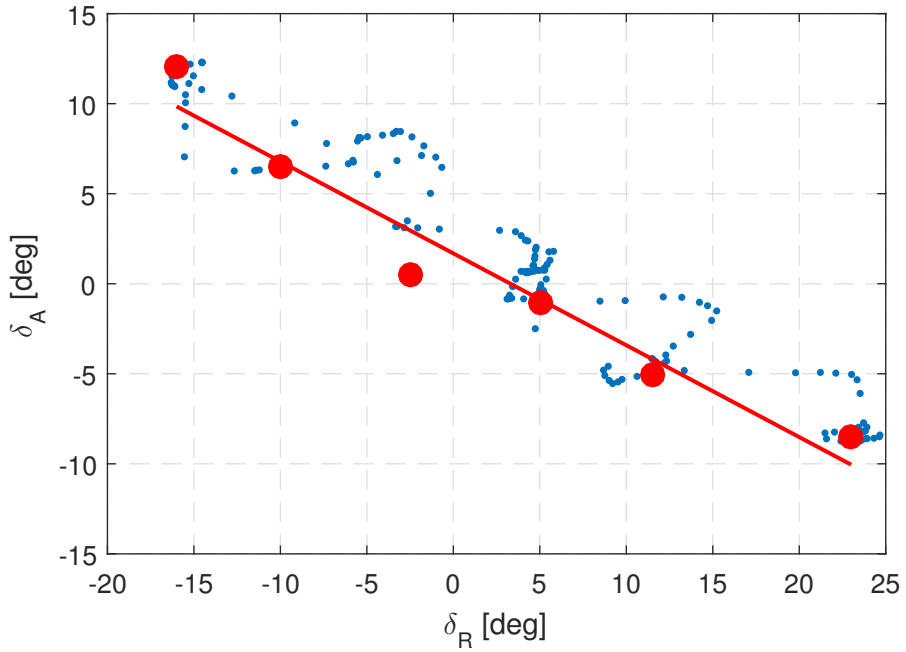

Figure C.8: SHSS δ_A vs δ_R, CR configuration, flight 01.1706 TOP 10.

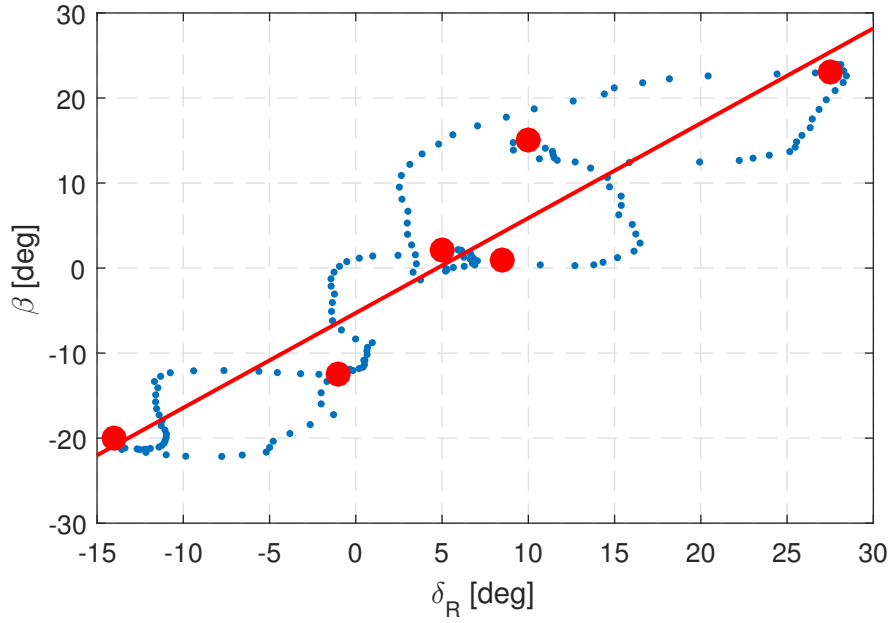

Figure C.9: SHSS β vs δ_R, CR configuration, flight 05.1106 TOP 10.

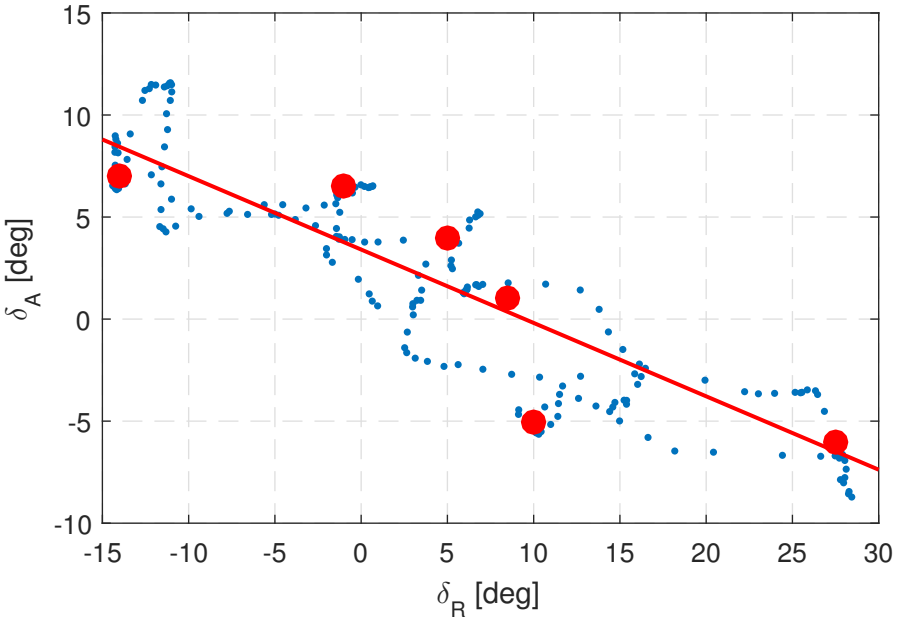

Figure C.10: SHSS δ_A vs δ_R, CR configuration, flight 05.1106 TOP 10.

C.3 Short period frequency prediction

Short period frequency can be predicted by approximating the airspeed as constant during the whole motion, which is a reasonable simplification and it has been verified in the post processing analysis of the short period flight. Longitudinal dynamics equations are not subject of this work and they can be found in [25]; the approximated formula of short period frequency is:

$$\hat{\omega}_{SP} = \sqrt{\frac{Z_\alpha M_q}{\bar{V}} - M_\alpha} \tag{C.1}$$

with:

$$Z_\alpha = -\frac{\bar{q}SC_{Z,\alpha}}{m} \tag{C.2}$$

$$M_q = \frac{\bar{q}Sc^2C_{m,q}}{2I_{YY}\bar{V}} \tag{C.3}$$

$$M_\alpha = \frac{\bar{q}ScC_{m,\alpha}}{I_{YY}} \tag{C.4}$$

where $\bar{V}$ and $\bar{q}$ are trim airspeed and trim dynamic pressure, respectively.

Aircraft derivatives have been estimated with Tornado, in the characteristics of airspeed and CG location of the test:

$$C_{Z,\alpha} = 4.9748 \tag{C.5}$$

$$C_{m,q} = -13.1109 \tag{C.6}$$

$$C_{m,\alpha} = -0.5083 \tag{C.7}$$

Inertia round the Y-axis has been calculated with Airplane Design V, by Roskam ([23]), which suggests a simple formula for a first approximation of aircraft inertia:

$$I_{YY} = \frac{l^2 W \bar{R}_Y^2}{4g} \tag{C.8}$$

$\bar{R}_Y$ is the non-dimensional radius of gyration, defined as:

$$\bar{R}_Y = \frac{2R_Y}{l} \tag{C.9}$$

where R_Y is the radius of gyration of the aircraft of mass M, namely the distance from the Y axis to a point mass M that gives an equivalent inertia to the original object. The non-dimensional radius of gyration is found in [23], which provides the values for various airplanes and requires to find out the most similar one in terms of weight and length. The chosen aircraft

is the Cessna 150M, whose weight is 510 kg with one pilot and its length is 6.5 m. The G70 is 30 cm shorter and has an additional occupant who increases the weight; since the moment of inertia is a mass times a quadratic distance, the two contributions compensate each other: therefore, for a first order approximation, the value of $\bar{R}_Y = 0.405$ can be considered acceptable.

The resultant frequency of short period is:

$$\hat{\omega}_{SP} = 2.65 \frac{rad}{s} \tag{C.10}$$

C.4 Phugoid test executed with different techniques

The aim of this section is to report other test points executed with a different technique with respect to the one prescribed in CS23 FTG ([1]) and to understand how different flight techniques might influence the phugoid test results. The test point are not enough to express conclusions about frequency value and pilot technique, but it is clear that the stick-fixed test points have a lower number of cycles, namely they damp earlier, both in CR and LND configuration.

Step input, sitck-free, CR configuration

During this test point the pilot pushed the stick forward without taking it back in the initial position, namely the input was a step and not a pulse; the aircraft response was observed without the hand on the stick, as shown in Fig. C.11. During the test a gust has been most likely encountered at 100 s from the beginning of the test point, when the speed was already damped; it is clear from the pitch angle, which has a sudden variation after some seconds of flatness. The results are reported in Tab. C.1.

Table C.1: Phugoid test results of flight 05.1006 TOP 6.

Conf.	$\overline{T}$ [s]	ξ [-]	ω_{PH} [rad/s]	Δt_{IMP} [s]
CR	22	2 cycles	0.29	3

Pulse input, sitck-fixed, CR configuration

The elevator is pushed forward and than moved back to the original position, but the stick is holded for all the duration of the test point, as shown in Fig. C.12. Test results are summarized in Tab. C.2.

Table C.2: Phugoid test results of flight 05.1006 TOP 6.

Conf.	$\overline{T}$ [s]	ξ [-]	ω_{PH} [rad/s]	Δt_{IMP} [s]
CR	17	1 cycles	0.37	7

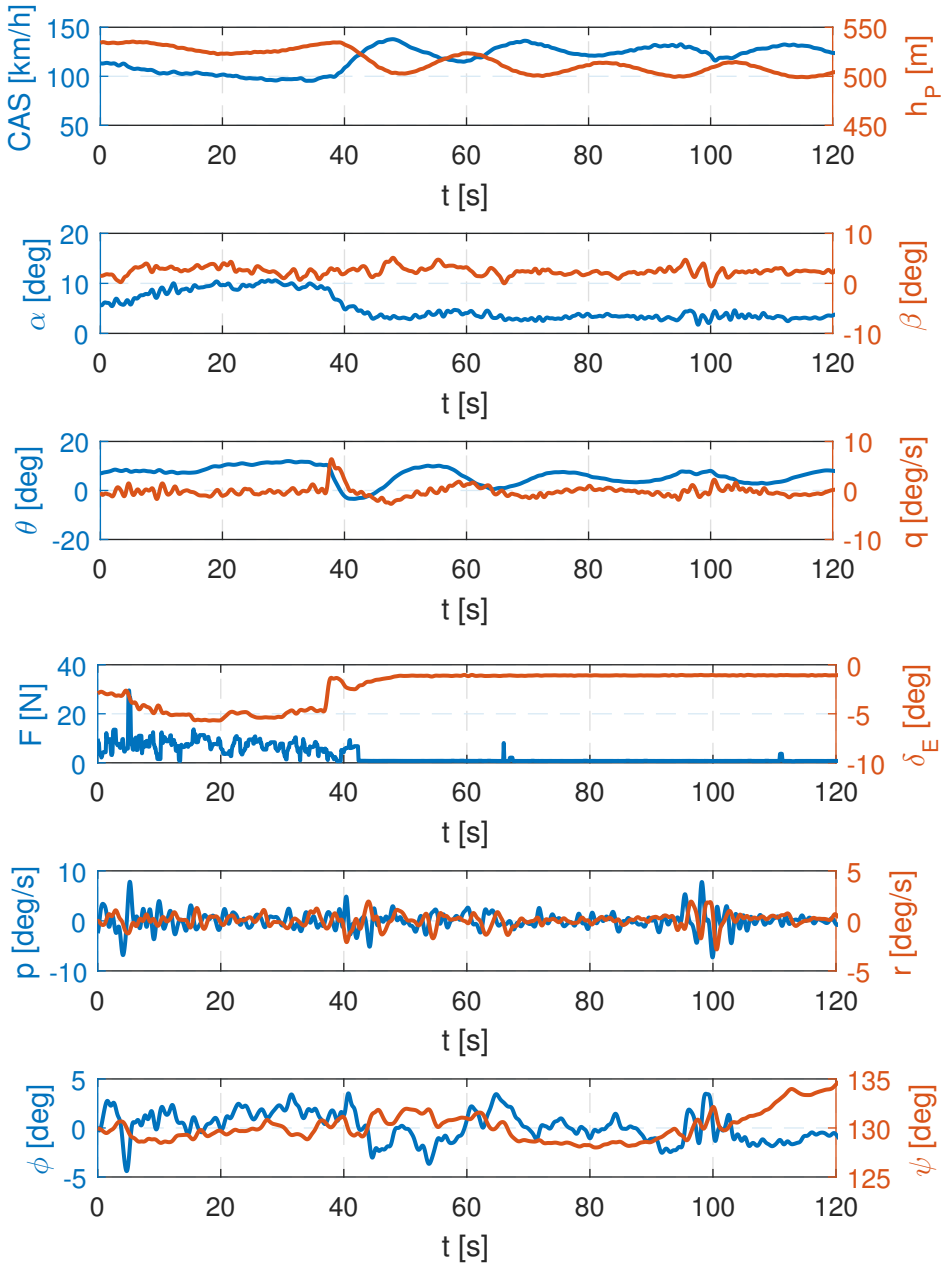

Figure C.11: Phugoid test time history, CR configuration, flight 05.1006, TOP 6.

Pulse input, sitck-fixed, LND configuration

The elevator is pushed forward and than moved back to the original position, but the stick is holded for all the duration of the test point, as shown in Fig.

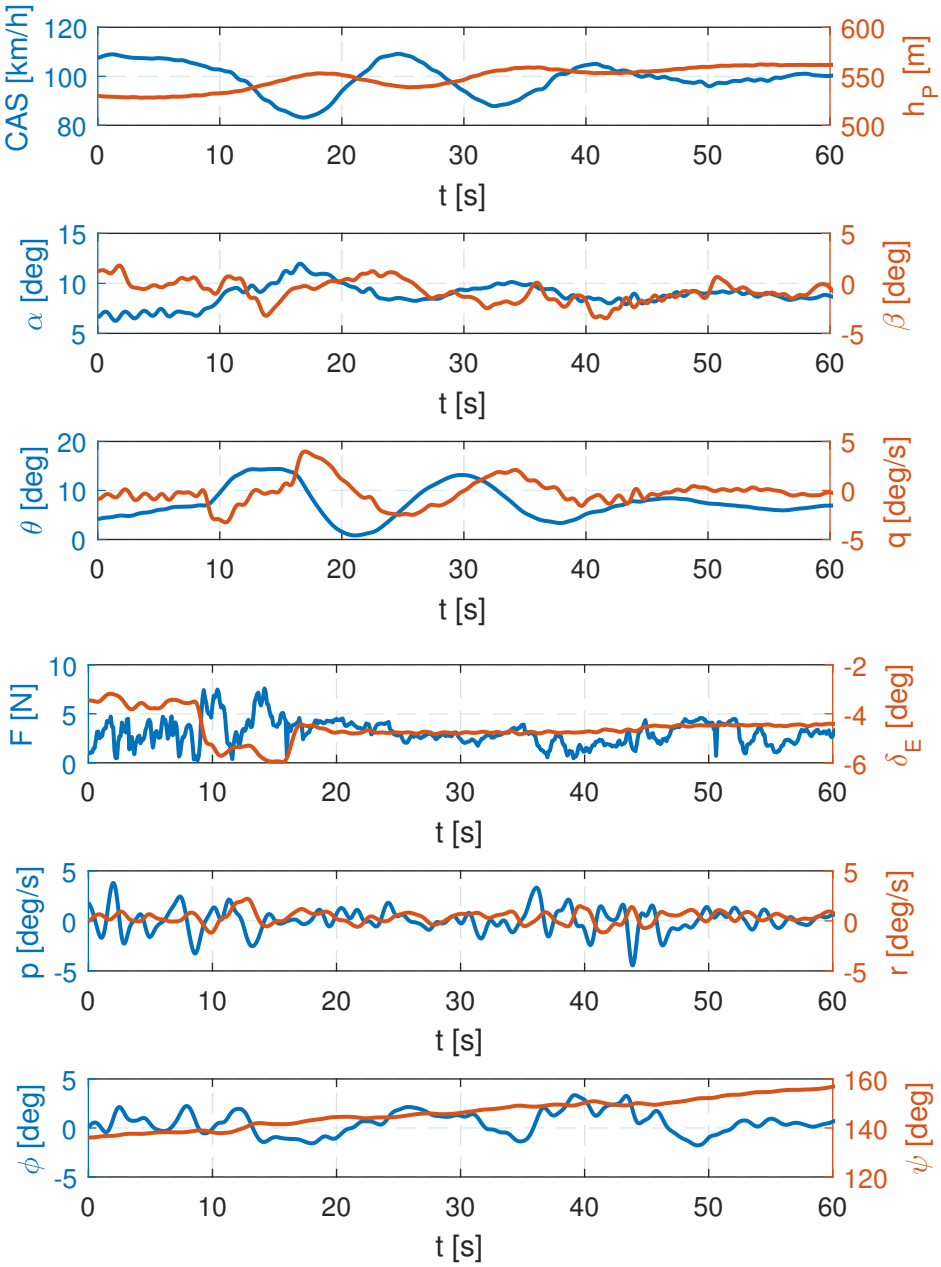

Figure C.12: Phugoid test time history, CR configuration, flight 06.1006, TOP 10.

C.13. Test results are summarized in Tab. C.3. Since the phugoid has been damped in half a cycle, all the measures reported are referred to the half period and then doubled.

Table C.3: Phugoid test results of flight 04.1006 TOP 8.

Conf.	$\overline{T}$ [s]	ξ [-]	ω_{PH} [rad/s]	Δt_{IMP} [s]
LND	22	0.5 cycles	0.29	5

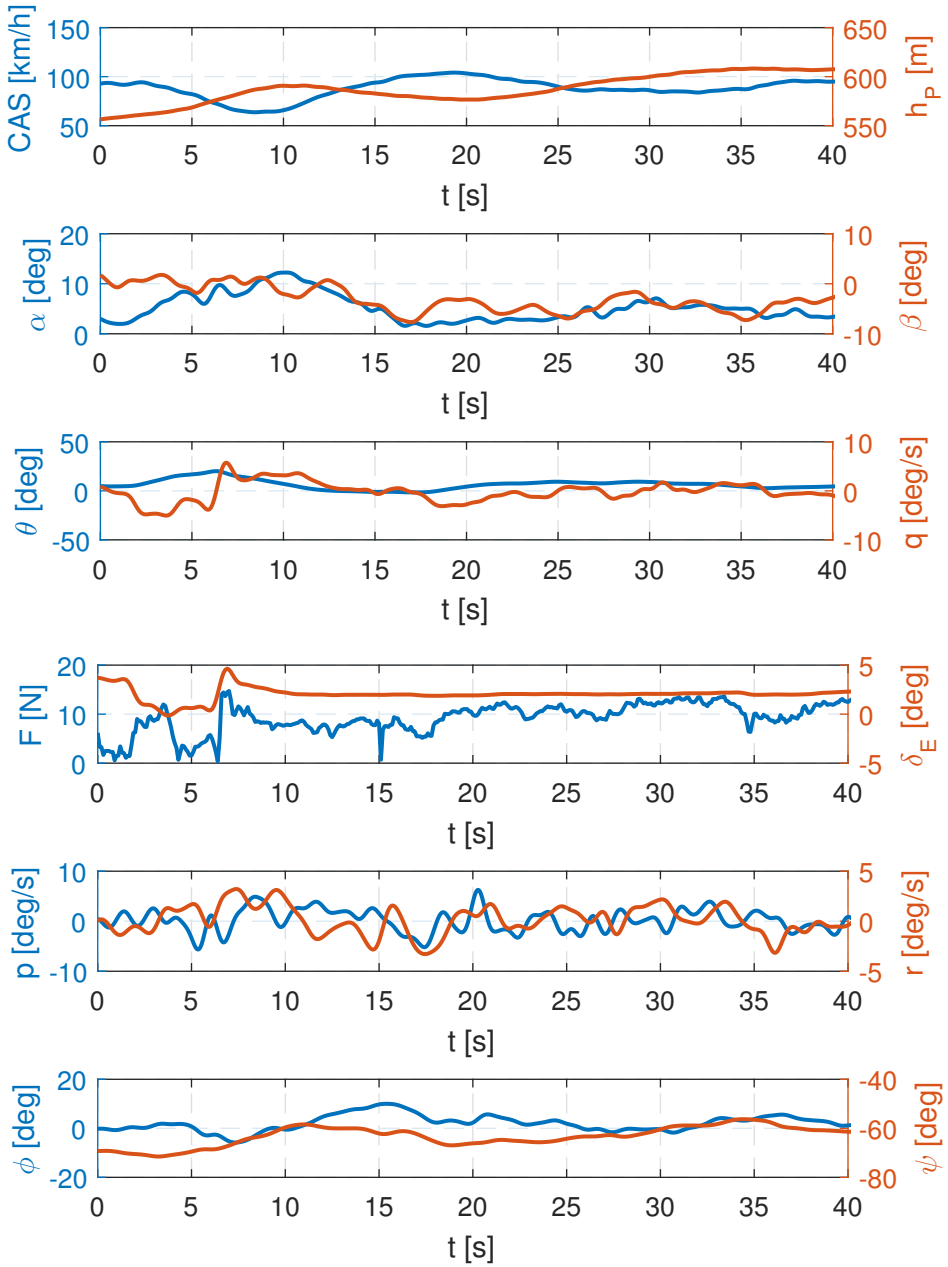

Figure C.13: Phugoid test time history, LND configuration, flight 04.1006, TOP 8.

Appendix D

Bootstrap approach

The main section dedicated to Bootstrap approach to flight performance enumerated the result with the so called *3rd data set*, which employs, to evaluate propeller polar coefficients m and b, V_{FC} and V_M. This appendix shows what happens with the choice of the other data sets. The results in terms of drag coefficients C_{D0} and K are the same and have been already reported in the main section and they will not be repeated in this appendix.

The first set uses, beyond V_{BG} and $V_{d,BG}$ which are common to all the data sets, V_{SC} and V_{FC}, while the second data set employs V_M and V_{SC}. Tab. D.1 enumerates the propeller polar coefficients for all the approaches (also of the 3rd one, for a quick comparison), while D.1 and D.1 show the results in terms of Penaud's graphs and rate of climb performance for data sets 1 and 2.

Table D.1: Bootstrap propeller polar coefficients with all the data sets.

Data set	m	b
1	2.3615	-0.0121
2	2.4295	-0.0121
3	2.6555	-0.0226

Data sets 1 and 2 provide the same value of b and slightly different values of m. Both the approaches have results which heavily underestimate the available power of the aircraft and its climbing ability, most of all the first one, which shows a maximum ROC 300 ft/min less of the real one. The second data set reduces the gap to 250 ft/min, thanks to the higher value of m.

The analysis shows how all the input take part in the great overall error of the method, but it is also clear how the main role in the great error

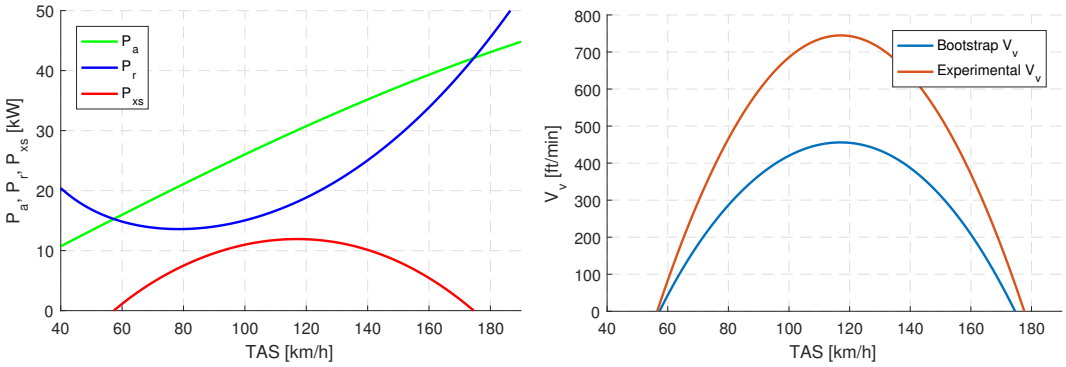

(a) (b)

Figure D.1: Climb performance graphs with V_{SC} and V_{FC} as input.

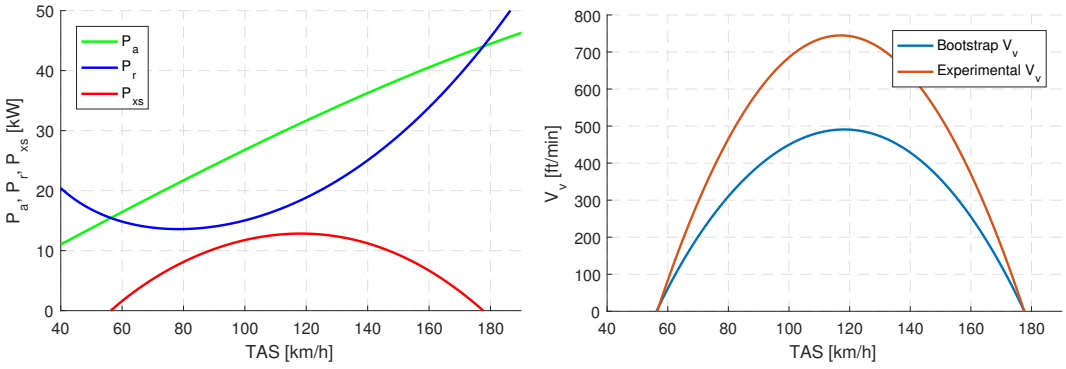

(a) (b)

Figure D.2: Climb performance graphs with V_M and V_{FC} as input.

propagation is played by V_{SC}. The proof is the more satisfying result coming from the third data set, which does not consider the speed of steepest climb as input.

Bibliography

[1] *Certification Specifications for Normal, Utility, Aerobatic and Commuter Category Aeroplanes, CS-23 Amendment 4*, EASA, 2015.

[2] *Certification Specifications for Very Light Aircraft, CS-VLA, Amendment 1*, EASA, 2009.

[3] *Decreto del Presidente della Repubblica n.133*, 2010.

[4] *Legge 25 marzo 1985, n.106 - Disciplina del volo da diporto o sportivo*, 1985.

[5] *LTF-UL, Airworthiness Requirements for Three axes standard control Ultra Light Aircraft (UL-Aircraft)*, 2003.

[6] Nando Groppo SRL, *Manuale di impiego e manutenzione, G70 TRAIL*, ver. 1, 2017.

[7] Rotax, *Operators Manual for Rotax Engine type 912 Series*, 2015.

[8] Abbott, H. Ira and Von Doenhoff, Albert E., *Theory of wing sections*, Dover, New York, 1959.

[9] Castelletti, T., *Design and development of the new generation of a flight test instrumentation system for ultra light machines*, MSc thesis, Politecnico di Milano, 2015.

[10] Etkin, B., *Dynamics of flight: stability and control*, New York, Wiley, 1996.

[11] Gadarco, T. and Terzaghi, V., *Flight testing for the final development and type certification of a new ultralight aircraft*, MSc thesis, Politecnico di Milano, 2015.

[12] Gardner L. (ed.), *Society of Flight Test Engineers Reference Handbook*, SFTE, Lancaster, CA, 2001.

[13] Guglieri, G. and Riboldi, C. E. D., *Introduction to flight dynamics*, Torino, Celid, 2014.

[14] Jategaonkar, R. V., *Flight vehicle system identification : a time domain methodology*, Reston, VA, American Institute of Aeronautics and Astronautics, 2006.

[15] Kimberlin, R., *Flight testing of gixed-wing aircraft*, Knoxville, Tennessee, American Institute of Aeronautics and Astronautics, 2003.

[16] Lowry, J. T., Analytical V speeds from linearized propeller polar, *Journal of Aircraft*, 33, 1, 1996, 233-235.

[17] Lowry, J. T., The Bootstrap approach to predicting airplane flight performance, *Journal of Aviation/Aerospace*, volume 6, 1, 1995.

[18] Minichini, L., *Developement of a WiFi-based telemetry system for ULM flight testing*, MSc thesis, Politecnico di Milano, 2015.

[19] National Aeronautics and Space Administration, *Information summaries - Steady sideslip.*

[20] Phillips, F. Warren, *Mechanics of flight*, Hoboken, New Jersey, John Wiley and Sons Inc., 2004.

[21] Quaglietta, S., *Prove di volo su velivolo ultraleggero: scelta dell'elica e caratterizzazione delle prestazioni e della stabilità statica longitudinale*, Msc thesis, Politecnico di Milano, 2014.

[22] Rolando, A., Rossi, F., Castelletti, T. and Reghenzani, F., *Mnemosine Mark-V: The Fifth Generation of an Ultra Light Machine-Dedicated FTI System*, 27th Annual Society of Flight Test Engineers European Chapter Symposium, Nuremberg, Germany, May 10-12, 2016.

[23] Roskam, J., *Airplane Design - Part V: component weight estimation*, Ottawa, Kansas, Roskam Aviation and Engineering Corporation, 1989.

[24] Roskam, J., *Airplane Design - Part VI: preliminary calculation of aerodynamic, thrust and power characteristics*, Ottawa, Kansas, Roskam Aviation and Engineering Corporation, 2004.

[25] Roskam, J., *Airplane flight dynamics and automatic flight controls*, Lawrence, Kansas, DARcorporation, 2001.

[26] Taylor, J., *Introduzione all'analisi degli errori: lo studio delle incertezze nelle misure fisiche*, Bologna, Zanichelli, 2000.

[27] Trainelli, L., *Appunti di Sperimentazione in Volo - Approccio 'Bootstrap' alle misure di prestazioni di motoelica*, 2017.

[28] Trainelli, L., *Lezioni di Meccanica del Volo, 7 - Equilibrio, controllo e stabilità longitudinali in volo rettilineo*, 2010.

[29] Von Mises, R., *Theory of flight*, New York, Dover Publications, 1959.

[30] Wheeler, A. and Ganji, A. R., *Introduction to engineering experimentation*, Boston, Pearson, 2010.

[31] $http://www.e-props.fr/16/calcA.php$

[32] iMAR Navigation, $i\mu VRU$, 2014. $http://www.imar-navigation.de/downloads/IMU\_myIMU-01.pdf$.